ABSTRACT

Title of Dissertation: PARTICLE CHARGING EFFECTS ON PIV MEASUREMENTS OF PLASMA ACTUATORS

Arber Masati, Doctor of Philosophy, 2017

Dissertation directed by: Associate Professor Raymond J. Sedwick
Department of Aerospace Engineering

Plasma actuators gained popularity during the change of the millennium for their ability to induce airflow and reattach stalled flow. Since then, investigations have been conducted to characterize their performance and extend their applications. Plasma actuators can be used to increase lift, decrease drag, and increase the efficiency of wind turbines. Phase locked ensemble averaging particle image velocimetry (PIV) is used to determine the induced velocity field and characterize actuator behavior and performance. However, very few studies account for particle charging from dusty plasma theory. Particle charging theories for high pressure plasmas predict a mostly linear trend between charge and particle size, with smaller particles charging less. In this work, PIV

experiments were conducted with monodisperse nanoparticles for sizes ranging between 300 nm and 1250 nm. Results showed that smaller particles follow the flow more closely. PIV uncertainty quantification was performed for ensemble averaging processing. A weighted linear fit was applied to each vector and extrapolated to the 0 nm particle speed, which is taken as the true air speed. Stokes drag force fields were calculated using the known velocity difference, and using a force balance calculation the electrostatic force acting on the particles was calculated. The electrostatic force near the actuator electrode was always acting upstream, implying that particles can attain either negative or positive charge, depending on the phase.

PARTICLE CHARGING EFFECTS ON PIV MEASUREMENTS OF PLASMA ACTUATOR

by

Arber Masati

Dissertation submitted to the Faculty of the Graduate School of the
University of Maryland, College Park in partial fulfillment
of the requirements for the degrees of
Doctor of Philosophy
2017

Advisory Committee:
Professor Raymond J. Sedwick, Chair/Advisor
Professor David Akin
Professor James F. Drake
Professor Kenneth Kiger
Professor Kenneth Yu

Acknowledgement

First I would like to thank my advisor, who, has listened and welcomed my questions, comments, concerns, and smart remarks throughout all these years. In the beginning I planned to get a Master's degree and find employment. His leadership and guidance as an advisor helped persuade me to pursue a Ph.D. I would also like to thank my committee, who have spent hours guiding me about my research, aerospace engineering, PIV, and physics. Their help and communication is valued and appreciated.

My lab mates have always been there to help with experiments and analysis. They have always been there for happy hours and relaxation too. They are good friends of mine and I wish them the best. My roommates, who are numerous, have always been supportive and understanding no matter the circumstance. Thank you.

A special thank you to Dr. Leishman and his graduate students, Anish Sydney and Joe Ramsey, both of whom are doctors now. They provided me with the tools and knowledge to conduct preliminary PIV experiments. Thank you also, to Dr. Jones and her students, Andrew Lind and Field Manar specifically. They allowed me to use their equipment and get the data that makes up this dissertation.

Last but certainly not least, my family, who supported me all my life and never stopped asking, "When will you finish?" They love me the most and I love them the most. Thank you!

Table of Contents

List of Figures

List of Tables

Chapter 1: Introduction

More than 100 years have passed since the Wright brothers' first flight. The 1903 flyer lifted off a sandy beach and flew under its own power for several seconds. To control the plane in flight, the pilot had to pull on strings that changed the shape of wings causing the airplane to roll. Fast forward a century and technology advancements have made airplanes common. Airplanes have grown in size and capability. Some can go faster than the speed of sound; others cannot be detected by radar. Whatever the technological advancement however, some design concepts have remained. All airplanes need control structures that help with maneuvering and control. Placed on the far edges of the wings, ailerons change the shape of wings, increasing or decreasing lift causing the airplane to roll. The Wright brothers pulled strings to alter the shape of their wings which allowed them roll control. Today, strings have been replaced by mechanical actuators that provide the torque necessary to move ailerons. Still, wing shaping for control has remained since the days of the first airplane.

Plasma actuators are light weight, electrically driven, thin devices that can be placed on a surface and alter the airflow. They don't have moving parts, relying instead, on high voltage and electric fields to induce airflow in the boundary layer. A schematic of a simple plasma actuator is shown in Figure 1-1. More detail on optimal configuration will follow in the succeeding sections but plasma actuators are not complicated in their design. Two metal electrodes are placed on opposite sides of a dielectric sheet such that one starts where the other one ends. The electrodes are usually thin metal strips, less than a millimeter thick but about a centimeter in width. Copper or aluminum tape is usually

the material of choice since it comes prepackaged in the correct dimensions and can be easily cut to alter designs. The dielectric can be made of any material that can withstand breakdown in the presence of high electric fields. Glass, printed circuit boards, acrylic, polyimide, and many more are suitable choices. The electrodes connect to a high voltage AC power supply with usual operating frequencies in the range of a few thousand Hz (1 kHz-10 kHz) and voltages in thousands of volts peak to peak (>10kV$_{pp}$). Although the frequency can vary to any degree capable by the power supply, the voltage must periodically exceed the breakdown value of air to ignite the plasma.

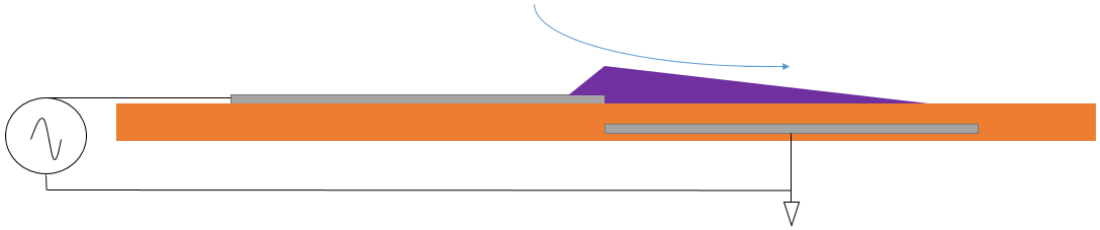

Figure 1-1. Plasma actuator in the standard configuration. Flow is induced to the right. Bottom electrode is encapsulated inside the orange dielectric and grounded.

1.1 Plasma

Plasma is a quasineutral collection of charged particles whose density is large enough to interact with both external and internal electromagnetic fields. The fourth state of matter, plasma is seldom studied except as part of advanced degrees. However, the world is filled with it. The Sun is a giant ball of plasma, neon lights are plasma, and lightning is plasma; albeit all of them are different form each other. Plasma can be classified by temperature and density. The sun is a hot and highly dense plasma with ion densities exceeding $10^{15}/m^3$ and temperatures exceeding 1000 eV. The aurora plasma, on the other hand, is a cold and low density plasma with ion densities at around $10^{10}/m^3$ and

temperatures around 0.1 eV. Plasma actuators are dense and cold, with a density of $10^{18}/m^3$, while the electrons can reach temperatures of 1 eV, the ions can be assumed to be near room temperature.

Plasmas have interesting effects. One of the effects is to charge anything within contact. Charged species, such as electrons and ions, will frequently collide with the material and affix charge even if the material is nonconductive. Another effect is the shielding of external fields. The charged particles will naturally reorient themselves to counteract most external fields. The length scale associated with the reorientation is known as the Debye length and is calculated using Equation (1-1)

$$\sqrt{\frac{\varepsilon_0 K_B T_e}{n_e q^2}} \tag{1-1}$$

Where ε_0 is the permittivity of free space, K_B is the Boltzmann constant, T_e is the electron temperature, n_e is the electron density, and q is the elementary charge. It is over this length that external fields are shielded from the rest of the plasma. This scale is also the standard measurement for distances within the plasma.

The frequency scale, also known as the plasma frequency, is associated with the reaction time of particles (electrons most of the time). The general speed of the electrons divided by the Debye length gives the plasma frequency shown in Equation (1-2)

$$\sqrt{\frac{n_e q^2}{m_e \varepsilon_0}} \tag{1-2}$$

Electron mass is m_e and the frequency for standard plasma actuators is more than 50 GHz. The small Debye length and large plasma frequency allow the plasma to reach local equilibrium during operation.

Dusty plasma, sometimes called complex plasma, is a special field of study that focuses on the dynamics and interactions of plasma that has small dust particles usually in the nanometer or micrometer range, immersed within it. Interactions between the dust and the plasma constitute a new set of dynamics. The most important new parameter in dusty plasma is the particle charge. Whenever plasma is in contact with an object, ions and electrons impart a charge on the object. The long-distance nature of the Coulomb force complicates interactions in dusty plasma. Khrapak and Morfill give an overview of basic processes in dusty plasma, including particle charging, potential distribution, interparticle interactions and the ion drag force[1]. A more detailed discussion will be provided in later chapters.

1.2 Plasma Actuators

Plasma actuators use the principles of dielectric barrier discharge to ionize air between the two electrodes. The method requires the use of high voltage to surpass the 3 MV/m breakdown value of air. At the same time, the dielectric stops the transmission of DC power and lowers the power requirement to sustain the plasma. Plasma actuators induce flow through the acceleration of ions and the collisional momentum transfer onto the neutral fluid. Propellers drive flow in one direction using pressure differences. In contrast plasma actuators have no moving components. Because of their light weight, ease of construction, thin form, and electric operation, plasma actuators appeal to aerodynamic applications where their ability to alter flow is best situated.

In the late 1990's Roth et al.[2] used the term "One Atmosphere Uniform Glow Discharge Plasma" to describe what would later be known as plasma actuators. In their

experiments, multiple plasma actuators were mounted on a flat plate and tested in a wind tunnel. One set of plasma actuators had an asymmetric configuration similar to Figure 1-1; while the other set had a symmetric configuration with the bottom electrode directly underneath the top. They found that both configurations had an influence on the airflow but the asymmetric configuration decreased drag up to speeds of 10 m/s and induced boundary layer airflow of about 3m/s in static air. In 2003 Roth placed plasma actuators on top of an airfoil and conducted flow visualizations experiments[3]. The results showed that plasma actuators reattached flow at high angles of attack until about 16° at which point flow detached. Figure 1-2 a) shows stalled flow over an airfoil and b) shows the reattached flow when plasma actuators are operational. The acceleration and reattachment of flow popularized plasma actuators as airflow manipulation devices.

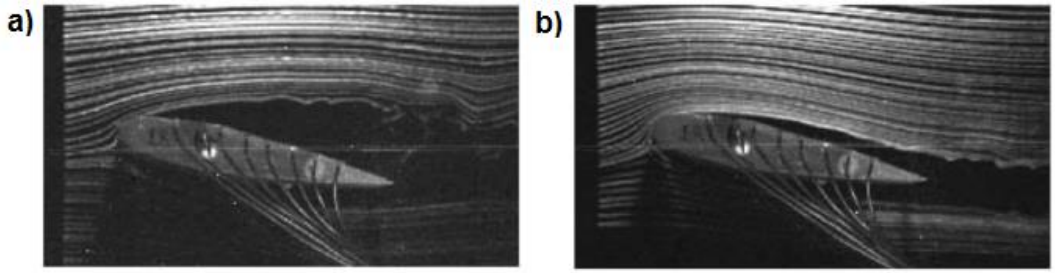

Figure 1-2. Plasma actuators acting on stalled flow a) plasma off, b) plasma on. Images from Ref. 3.

Their thin design and easy construction allows researchers to place plasma actuators on different objects and conduct experiments to test their applications and effectiveness. He et al. attached plasma actuators on the leading edge and trailing edge of an airfoil[4]. They conducted wind tunnel experiments to measure the effect of the plasma actuators for Reynolds numbers up to $3x10^5$. Their results show that the leading edge plasma actuator reattached flow for an angle of attack of 24° and increased the maximum coefficient of lift. The trailing edge plasma actuator increased lift throughout the entire

range much like a trailing edge flap. Figure 1-3 shows the critical angle of attack increase that plasma actuators are capable of producing.

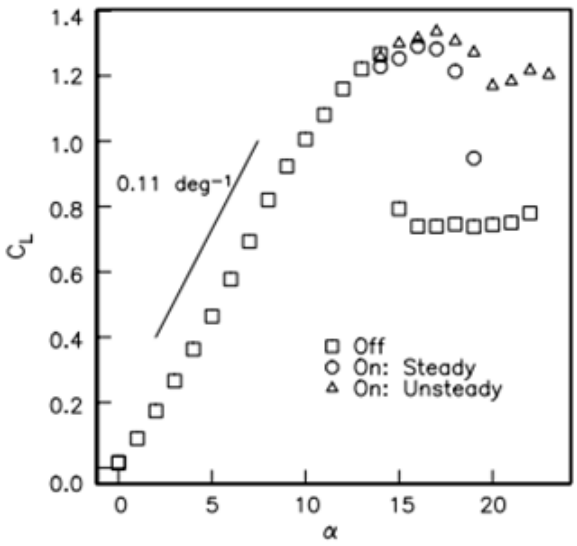

Figure 1-3. Coefficient of lift as a function of angle of attack with different plasma actuator operations. Data from Ref. 4.

Greenblatt et al. attached plasma actuators on the leading edges of a vertical axis turbine[5]. They conducted wind tunnel experiments to determine the power coefficient of the turbine. Vertical axis turbines experience a wide range of angle of attack because of their circular motion. Plasma actuators provided flow control during operation and increased performance more than 30%.

Plasma actuators can also be used at supersonic speeds. Nishihara et al. used Schlieren imaging to capture the effects of a plasma actuator at Mach 5 flow conditions[6]. The actuator was mounted on the front of a cylindrical body and operated using 5 ns, 30 kV pulses at repetition rates of up to 100 kHz. They found that the actuator induced compression waves that interacted with the bow shock, increasing the shock distance by up to 25%. Gnemmi and Rey placed low voltage plasma discharge devices on supersonic projectiles[7]. Their goal was to induce a change in direction by having the plasma interact with the shock structure. The projectiles experienced a 2 degree change in angle of attack after a 2.5 ms discharge. Kriegseis et al., seeing the potential use of plasma actuators as aerodynamic control devices, constructed a controller that helped the actuator maintain proper operation in gusty conditions[8]. The authors used Lissajous figures of the voltage

and current as well as light emission data, to characterize the power consumption of plasma actuators when a gust of wind passes over. The actuator power fluctuates during gusty conditions. A proportional integrating controller was designed from the gathered data. The power fluctuations were reduced from 4 Watts to 1 Watt.

The simplicity of plasma actuators makes them attractive devices for aerodynamic applications. There is much to be gained by enhancing the capabilities of plasma actuators. Researchers set out to characterize plasma actuators and improve their performance.

1.3 Particle Image Velocimetry

The performance of a plasma actuator can be characterized by the induced air speed. Pitot tubes and hot wire anemometers have historically been used to determine air speed but they are only capable of point measurements. Furthermore, velocities near the plasma are difficult to measure. Placing conducting metal near the plasma risks damaging the equipment through an electric shock. Even non-conductive material will attract charge and change the structure of the plasma. Particle Image Velocimetry (PIV) is a flow measurement technique that determines the two-dimensional velocity-field of a fluid. PIV requires three components. First, tracer particles that are injected into the flow; second, a laser that illuminates the part of the flow that is of interest; third, a camera to capture images of the tracer particles that are illuminated by the laser.

The concept is simple and is illustrated in Figure 1-4. Particles are injected into the flow, ①, to visualize the movement of the fluid. A laser, ②, is used in conjunction with optics to create a sheet of laser light. This sheet illuminates part of the flow with high

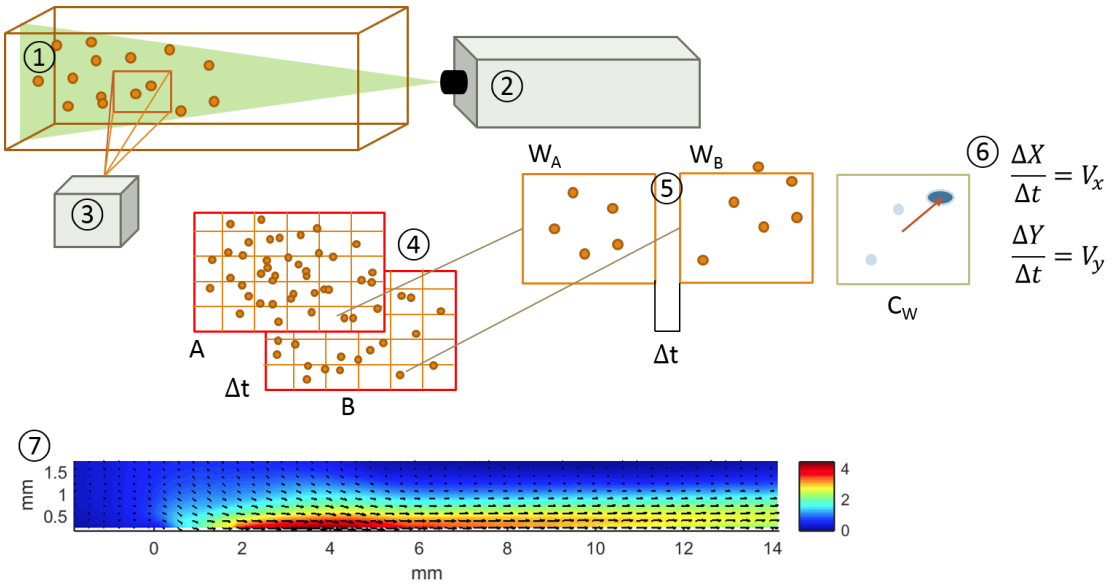

Figure 1-4. Particle image velocimetry 1) seeding of flow, 2) laser, 3) camera, 4) double images Δt apart, 5) particle locations between image A and image B, 6) cross-correlation results and velocity determination, 7) velocity results.

intensity light such that only particles in the sheet can be seen. A camera, ③, takes two successive images of the flow, ④, that are a set time difference, Δt, apart. The software will discretize the images into windows and will then compare windows from image A and image B, ⑤, using a cross-correlation algorithm. The results of the cross-correlation analysis yield a displacement vector that is used to calculate the velocity of the particles, ⑥. This process is repeated for every window pair for images A and B until velocity vectors, ⑦, have been calculated for the entire image.

In practice, PIV requires more attention to detail. The tracer particles must be selected with the proper size and density. Stokes drag, shown in Equation (1-3), is usually the most important force in PIV

$$F_{SD} = 3\pi\mu d(\vec{u} - \vec{v}) \tag{1-3}$$

Where μ is the viscosity of air, d is the tracer particle diameter, u is the air velocity and, v is the particle velocity. Stokes drag dictates the ability of a particle to follow the flow. A

good particle would have the same density as the fluid and be small enough so that it does not impede the fluid flow. Foam and other materials can be made with similar densities as water, and are popular choices. Matching the density of air is more difficult. The solution is to decrease the diameter of the particle so that the inertia can be minimized. The ability of a particle to follow a flow is determined by the particle's response frequency given in Equation (1-4) where ρ_p is the particle density

$$f_p = 18\mu/\rho_p d^2 \tag{1-4}$$

Due to the square dependence, the size of the particle is more important than the density of the particle. As long as the particle is small enough, denser material can be used for seeding air. Popular particle selections include polystyrene, glass micro-balloons, and different oils such as olive oil and di-ethyl-hexyl-sebacate (DEHS). Polystyrene particles can be manufactured with precise size tolerances and have a similar density with water. Glass micro-balloons are also popular for water PIV and have good size tolerances. Oils are popular choices for air PIV that does not require precisely sized particles. The oil is sent through an atomizer that creates a fine mist. Although individual droplets vary in size (DEHS droplets are centered around 300 – 400 nm, olive oil droplets are centered around 1 μm), the seeding capability of atomizers is exceptional and frequently used in air PIV, especially for larger scale experiments. Whatever the choice of particle, plasma will impart a charge on it. The strong electric fields will act on the particle and distort its ability to follow the flow.

1.4 Motivation

PIV is a powerful tool for capturing velocity data with the underlying assumption that particles closely follow the flow. The use of PIV to characterize plasma actuators creates a dusty plasma environment. Plasma imparts a charge on the particles and the strong electric fields complicate the dynamics. The electrostatic force may significantly affect the motion of a particle. To better determine the effect of particle charging, a set of PIV experiments for different size monodisperse particles was conducted. Smaller particles charge less than larger particles. It was expected that smaller particles would more accurately follow the flow. It is the goal of this work to illuminate the dusty plasma effects present in PIV studies of plasma induced flow. It is hoped that future PIV investigations of airflow with plasma can account for the effects of particle charging and, if significant, correct the PIV results. PIV is a tool used to find answers, not the answer itself.

Chapter 2: Literature Review

This section recounts important advancements in the fields of plasma actuators, PIV, and dusty plasma. The section is segmented into three different parts with each part covering one field. The intent was to cover important investigations that have shaped today's field and not to list all investigations that have been conducted till today; therefore, this section does not provide a complete representation of the research that has been conducted but offers a good overview of important points in time.

2.1 Plasma Actuators

Since the work by Roth et al., plasma actuator research has expanded to the characterization and optimization of the device. This section lists and summarizes research conducted on plasma actuators. Although not an exhaustive list by any means, important results and the evolution of understanding plasma actuator performance are reviewed. In truth, although plasma actuators were used for aerodynamic applications in the late 90's, by then, dielectric barrier discharges (DBD) existed and had numerous industrial applications[9]. Ozone production is a popular use of DBD because of the ease of operation and large-scale capability. Pollution control technologies employ DBD to provide reactive species that breakdown hazardous gases. CO_2 lasers and excimer lamps also base their design around DBD. However, the use of DBD for flow acceleration is a more recent invention. The technology is new and evolving, and as such the current state of the art may be vastly different from a future state in which plasma actuators have

industrial applications. Corke et al. and Moreau et al. offer good reviews of plasma actuator research in their papers[10-13].

2.1.1 Physical Design Parameters

This section reviews research for the construction and optimization of physical parameters such as electrode width and shape, gap distance, and dielectric strength and thickness. While they may be simple to build, an optimum design for plasma actuators does not currently exist.

Enloe et al. conducted a study on the effects that geometry has on plasma actuator performance[14]. They found that the maximum induced velocity increases with the length of the bottom electrode, even up to 25 mm for 16 kV_{pp}, but the effect is less pronounced for 12 kV_{pp}. This implies that there is an optimum length for a given voltage. They also found that thinner top electrodes generate more force than thicker top electrodes for the same power input. This can be attributed to the increased electric field resulting from the sharper gradient of the thinner electrodes. Hoskinson et al. came to the same conclusion in their research[15]. They studied the induced velocity and force generation of plasma actuators with wire electrodes made of copper, steel, and tungsten. Smaller diameter wires exhibit stronger forces, but unlike previous research they found that the force scaled exponentially. The material of the wire electrodes did not have a significant effect. Forte et al. conducted a parametric study to determine optimum construction of plasma actuators and increase the induced air velocity[16]. The results show that velocity increases with the width of the bottom electrode up to a certain point and then no noticeable changes occur. This agrees with Ref. 14 and places a lower limit on the width of the

bottom electrode to around 20 mm depending on the operating voltage. The width of the top electrode was parametrically studied by Kriegseis et al[17].Their results show that the optimum electrode configuration has the top electrode width equal to 25% of the bottom electrode width. Thomas et al. studied the effect of bottom electrode width and gap distance in their attempt to optimize plasma actuators[18]. The wider bottom electrode allowed for stronger flow. They also used a serrated top electrode, which increased the electric field and thrust in agreement with previous research. However, there was a negative gap between the electrodes.

The gap between electrodes is the distance between the end of the top electrode and the beginning of the bottom electrode. Figure 1-1, shows a plasma actuator with zero gap distance. The gap distance between the electrodes affects the velocity of the actuator. In Ref 16, a negative gap – one where the bottom electrode starts under the top electrode – decreases velocity. A gap of zero, or a few millimeters, produces the fastest velocity; while a gap of a centimeter, or more, decreases the velocity. Another study found similar results[19]. Negative gaps decrease both power input and velocity. However, power input was maximized at 2 mm while velocity was at its max at 4 mm.

Designs with multiple electrodes have also been researched. Durscher and Roy conducted experiments with multiple encapsulated electrodes and dielectric layers[20]. Three configurations where tested. First was a standard plasma actuator, the second had a middle electrode in the dielectric, and the third had two enclosed electrodes. With multiple electrodes the question becomes: what is ground? The authors researched multiple configurations with grounded and powered middle electrodes. They found that the middle electrode helped when it was not grounded and there was a large voltage

difference between all electrodes. The actuator with four electrodes had each electrode powered with a phase shift either leading of lagging the top electrode. The leading configuration was better. The group compared all the designs based on force measurements and found that standard plasma actuators delivered more force at lower voltages but the three-electrode configuration was more effective (Force/Power). Another study on multiple enclosed electrodes found similar results[21]. The authors built several actuators with multiple enclosed electrodes. Unlike the study mentioned above, the extra electrodes were small compared to the main enclosed electrode and all of them were grounded. Results show that standard plasma actuators are better than one of the other designs but worse than the new design which had two small electrodes close to the top electrode but lower than the large grounded electrode. The location of the electrodes inside of the dielectric plays a small positive role in actuator performance but the field has yet to adapt multiple electrode designs.

Plasma actuators can be placed one downstream of the other to increase induced velocities. Insulation should be used too if unwanted discharge initiate between the electrodes of different actuators[16]. In this configuration speeds can reach up to 8m/s. The final speed is not additive with number of actuators because of losses. The distance between the actuators influences the final speed. If they are too close, unwanted back discharges decrease performance. If they are too far, the velocity of the air decreases before reaching the next actuator. The optimum is around 2 cm. The ratio of thrust force for single, double, and triple actuators shows the non-additive combination of actuators[18]. The ratio for two actuators is about 1.6; the ratio for three is 2.3.

The dielectric stops DC current and stores charge on its surface. Research has shown that dielectric physical parameters are an important part of plasma actuator design. For example, glass and acrylic have different dielectric characteristics which affect plasma actuator performance[16]. The glass dielectric allowed for faster velocities with lower voltages but reached saturation, at which point the PMMA surpassed glass in induced velocity. The curves show that there is an asymptotic behavior for speed and power input for a given dielectric. Orlov et al. used a phenomenological model to calculate the effect of the dielectric constant[22]. Results show that there is an optimum frequency for dielectrics that depends on the dielectric constant; the smaller the constant, the higher the optimum frequency. Reference 11 argues that the capacitance of the plasma actuator is proportional to ε/h, where ε is the dielectric constant and h is the thickness of the dielectric. To increase the power to the plasma, the capacitance must be lowered by using thicker material with small dielectric constants. Reference 14 conducted experiments to determine the effect of dielectric constants and thicknesses. Force measurements for similar plasma actuators with different dielectrics show that plasma actuators built with low dielectric constants have higher thrust. They also found that for a given frequency, thicker dielectrics had stronger forces. The thickest dielectric used by Ref 18 was 6.35 mm, which is still thin when compared to the thickness of airplane wings, and wind turbine blades. Results showed that the gain in thrust by moving from a 3.15 mm dielectric to a 6.35 mm is not as large as the thrust gained by moving from a 1.59 mm dielectric to 3.15 mm. These experiments demonstrate that minimizing ε/h within the covered ranges, improves actuator performance. The minimum ε is 1, while the maximum h is in principle unbounded. In the limit of low dielectric constant and large h,

actuators should theoretically perform well. However, having a thick dielectric requires more voltage input to create a breakdown. The experiments did not include larger dielectrics, though at some point the electrodes would be too far from one another to create a strong discharge. Furthermore, the advantage of thin designs should also be considered when building plasma actuators.

Plasma actuators therefore, work better with thin top electrodes and wide bottom electrodes with a minimal horizontal gap between them. The dielectric should be thick enough to handle the voltage difference and have a low dielectric constant.

2.1.2 Driving Signal

The previous section reported on the physical aspects of plasma actuators. This section focuses on the power input parameters such as voltage, frequency, and signal waveform. While 30 kV/cm is required for breakdown in air at 1 atm, voltages and frequencies of plasma actuators can vary to anything allowed by the power supply. It has already been stated that dielectrics have an operating frequency zone best suited for them. To truly optimize and increase performance, researchers have conducted parametric studies to find the best voltage and frequency.

Operating voltage is one of the most important parameters. A higher voltage creates a stronger electric field. The stronger field pushes ions and transfers more momentum onto the neutrals thereby increasing induced flow velocity. Experiments show that velocity increases with applied voltage with a power law exponent of 3.5[11,23]. This relation holds for sinusoidal, sawtooth and square signals. Operating plasma actuators in a higher voltage leads to more than a cubic increase in the force. More recent experiments

determined the relation to be correct up to a certain voltage, after which the exponent changes to 2.3[18]. That voltage point was named the saturation voltage and depends on the dielectric material and frequency.

Experiments conducted to relate the saturation voltage and frequency for a dielectric were conducted by Thomas et al[18]. For a sine input the relation between saturation voltage and frequency is linear. Higher frequencies induce faster flow but reach saturation more quickly. Lower frequencies produce lower forces for the same voltage input but can reach higher voltages and higher forces than higher frequencies. The power input linearly varies with frequency for constant voltage[16]. The power supply would have to linearly increase power with frequency, which places a limitation on the voltage and frequency operation on the system. In general, higher frequencies perform better if the dielectric has a low dielectric constant and the voltage is below the saturation level. Because of the 3.5 power law exponent, voltage should be kept as high as possible unless saturation has been reached. At saturation, frequency should be reduced in order to attain better performance.

A different operation has been proposed and successfully used by Corke et al[11-13]. Plasma actuators don't need to be powered all of the time to alter air flow. They proposed using a sine wave with a duty cycle to only power the actuator part of the time. The actuator receives power and AC voltage for a designated time but then receives no input for the time determined by the duty cycle, which effectively lowers the operational frequency of the actuator and linearly reduces power requirements. This mode of operation is called unsteady operation and should not be confused with unstable operation. The actuator operates very well in unsteady mode. He et al. were mentioned

above for increasing lift and stall angle of attack[4]. The best results were obtained using unsteady operation. The duty cycle was chosen such that the effective frequency (duty cycle times regular frequency), matched the Strouhal number, which is the ratio between the effective actuator period and the time it takes air to traverse the chord length, $F^+=T/(c/U)$. Where, F^+ is the Strouhal number, T is the effective actuator period, c is the chord length, and U is the air speed. The Strouhal number can be formulated in terms of frequency, $F^+=fc/U$, with f being the effective actuator frequency. A Strouhal number of unity was found to require the least amount of voltage to reattach flow at high angle of attack. Unsteady operation of the actuator with $F^+=1$ outperformed steady operation and used significantly less power. The augmentation of wind turbine power generation was also mentioned previously[5]. Unsteady operation suits vertical turbines very well because the actuator does not need to operate for the entire blade cycle. Furthermore, when it is operating, unsteady operation can be used to reduce power input. The Strouhal number is hard to define for wind turbines because they experience a large variation in free steam velocity. The authors augmented the equation to account for the variation and found the best operational duty cycle for the plasma actuator. Unsteady operation lowered the required actuator power to less than 10% of the extra power delivered by the actuator. The use of plasma actuators on vertical wind turbines helps generate more than 10 times the amount of power used to run the actuator itself. Benard et al. placed a plasma actuator at the leading edge of an NACA 0015 airfoil[24]. The plasma actuator operated in a steady mode increased lift, decreased drag, and extended angle of attack operational range as observed in previous research. Steady mode operation at frequencies corresponding to $F^+=1$ or $F^+=1/2$ showed improvement over other frequencies. Effective actuator

frequencies with $F^{+}>10$ also showed improvement. The authors believe that excitations of boundary layer frequencies, which are 10 times higher than bulk flow frequencies, and improved actuator performance at higher frequencies are the cause. Use of unsteady actuation can improve aerodynamic performance and reduce power requirements.

Different applied voltage waveforms follow the 3.5 power law relation with respect to voltage, but generate different amounts of thrust. Usually, a sinusoidal signal drives plasma actuators but sawtooth and square signals have also been used successfully. Enloe et al. found that positive sawtooth signals deliver more thrust than negative sawtooth signals[23]. Balcon et al. conducted particle image velocimetry (PIV) experiments to determine the effect of the two sawtooth signals on airflow[25]. They found that negative sawtooth signal induced faster flow, which seems to disagree with previous thrust measurements. However, the velocity profile for the negative case was thinner and had a small negative flow 8 mm above the actuator. In contrast the positive sawtooth flow was slower but had little or no negative flow far above the actuator.

Kotsonis and Ghaemi used high speed PIV to characterize sinusoidal, square, and sawtooth waveforms[26]. They found that a square wave induces the fastest velocities but uses more power. A sinusoidal waveform comes second but is more efficient. The positive sawtooth is faster than the negative sawtooth, but the velocity profile was slimmer, which agrees with Balcon et al. In general, square waves induce more flow but use more power, sine waves are in the middle, and sawtooth waves induce less flow and use less power.

2.1.3 Chemistry and Phase Analysis

The current through a plasma actuator can be easily measured by attaching a small resistor between ground and the enclosed electrode. The current waveform changes for different voltage waveforms, but it also changes between positive and negative cycles. For a sinusoidal voltage, the current waveform exhibits numerous large peaks during the positive part of the cycle. During the negative part of the cycle the current waveform exhibits smaller but more numerous peaks. Enloe et al. took fast capture pictures of the streamer and found that the positive cycle has a different streamer structure than the negative cycle[14,23]. As shown in Figure 2-1, the negative cycle had more diffuse streamers that occupied a larger dielectric area, while the positive cycle had thin strong streamers that extended from the exposed electrode toward the dielectric like lightning bolts. They also used a photomultiplier tube to analyze the light coming off the actuator. The negative cycle is brighter and shines longer than the positive cycle. The difference in the cycles and the pictures suggest the positive cycle is more filamentary while the negative cycle is more diffuse. This implies that the performance of the actuator is different during the two cycles.

Font et al. set out to measure the difference in thrust between the two cycles [27] . They mounted the plasma actuator to a torsional plate and shined a laser through a series of beam splitters

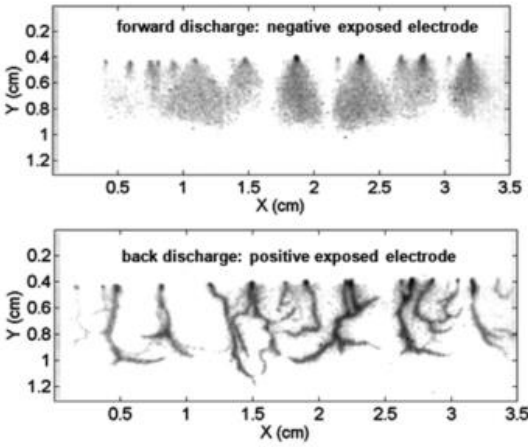

Figure 2-1. Images of plasma discharges at negative voltages (top), and positive voltages (bottom) from Ref. 48.

and mirrors. The beam bounced off a mirror on the torsional plate and into a laser detector that measured the incoming angle. When the plasma actuator turned on, the plate rotated and the detector measured the angle divergence. The force of the plasma actuator was measured over the entire cycle. The results showed that the negative cycle was stronger than the positive cycle. Plasma actuators use strong electric fields to accelerate ions forward and impart momentum through collisions. A strong force during the negative cycle implies that negative ions are present in the plasma. Oxygen is the second most electronegative element after Fluorine. As such, oxygen likes to absorb electrons and charge negatively. To test the effects on oxygen the authors placed their laser and plasma actuator setup inside a vacuum chamber. Experiments were conducted at atmospheric pressure with oxygen levels varying from 0 to 20%. Oxygen has a significant effect on force. The force dependence on O_2 content is exponential, rising to 4.5 times the force of pure N_2. During the simulated atmosphere experiment (20% oxygen), the plasma actuator accelerated the flow twice. Once during the positive cycle and again during the negative cycle. The density of positive ions is larger during the positive cycle, while the density of negative ions dominates during the negative cycle. In fact, the negative cycle produced more force. The measured force for the pure nitrogen showed both a deceleration and an acceleration during both cycles. Since Nitrogen is not very electronegative, there are no negative ions to push the flow. Interestingly, both cycles act to push and pull the flow.

A new convention for characterizing plasma actuators arose from this work[11]. Plasma actuators are characterized using the push-pull terminology. The first word corresponds to the negative cycle or rather the forward push of electrons from the top

electrode. The second word corresponds to the positive cycle or the backward pulling of electrons to the top electrode. The plasma actuator used in the oxygen level experiment operates in PUSH-push mode, where PUSH corresponds to a large acceleration and push corresponds to a small acceleration. When oxygen is present there is a strong push during the negative cycle and a weaker push during the positive cycle.

Phase and time resolved experiments have been conducted that show this behavior. Forte et al. used Laser Doppler velocimetry (LDV) to calculate time resolved velocities induced by plasma actuators[16]. They found that the negative cycle induces higher velocities. The actuator induced flow during the positive cycle as well, so it is classified as PUSH-push. Leonov et al. used high-speed pressure probe measurements to calculate the velocity in both air and nitrogen[28]. In air the actuator operated in PUSH-push mode. In nitrogen, push-none was observed, which contradicts results from Ref. 27. High-speed PIV experiments by Kotsonis and Ghaemi illuminate different operating modes for waveforms[26]. They used a 6 kHz laser system to obtain 48 velocity fields for each waveform tested. The sinusoidal waveform behaved as expected, PUSH-push. The square waveform, which was found to be less power efficient, operated in a PUSH-pull mode. The voltage slope of the square wave is large; it is not surprising to see the strong PUSH for the negative cycle. For the positive half cycle, it is possible that the positive ions do not have enough time to overtake the negative ions and so the electric field slows the flow by pulling the negative ions back. This leads to wasted power and the inefficiency in square waves. The positive sawtooth acts in PUSH-pull but is weaker than the square waveform. The negative sawtooth acts in a push-none characterization.

Plasma actuators can push flow during both cycles when using sinusoidal waveforms. For all waveforms, actuators are stronger during the negative cycle, when negative oxygen ions outnumber positive ions.

2.1.4 Atmospheric Conditions and Surface Charge

Airplanes experience a wide range of atmospheric conditions. Plasma actuators should be tested with similar conditions, to check performance. Erfani et al. tested the effect of temperature[21]. They placed the actuator on dry ice to cool it and on hot plate to heat it. Hotter plasma actuator perform slightly better, while colder plasma actuators perform worse. They found a larger performance gap between the cold and ambient case. Benard et al. conducted experiments to test plasma actuator performance at different pressures and relative humidity[29,30]. They placed the actuator inside a vacuum chamber and used a glass Pitot tube to find the velocity profile at different pressures. Power and the length of plasma discharge increase linearly as pressure is reduced. Induced velocity increases until about 0.6 atm; below that pressure, the velocity starts to decrease. The electrode configuration was constant throughout the experiments. Below 0.6 atm, the plasma length exceeded the bottom electrode length. The authors acknowledge that the electrode configuration was not optimized for the different pressures and longer electrodes may help. In another experiment, they kept the pressure constant but varied the relative humidity from 40% to 98%. Power input was largest for 55% and decreased to a minimum at 85%. There was a sharp rise in the consumed power for 98% humidity. The number of current spikes associated with the plasma discharge showed an increase of positive spikes and a decrease of negative spikes. LDV experiments were conducted to

better understand the velocity evolution. Results show a stronger negative cycle throughout the humidity range. The higher humidity values decreased the performance of the actuator. Relative humidity of 70% seems to be the maximum level that plasma actuators have effective operation. A higher applied voltage helps recover lost performance at the price of higher power input.

To measure the charge on the dielectric surface, Enloe et al. separated the grounded electrode into segments[31]. The segments were attached to op-amp integrating circuits and connected to the top electrode through a small high voltage capacitor. This configuration is known as a V-dot probe, which is used to calculate the voltage and charge on one part of a capacitor. The op-amp output includes both the capacitive load between the two electrodes and the contribution by the surface charge. Results were calibrated for the capacitive part by running the actuator below the breakdown voltage. Segments farther from the top electrode required less adjustment. The potential distribution on the dielectric shows a difference between the two cycles. The potential of the dielectric throughout the entire dielectric increases during the positive voltage half-cycle. When the plasma quenches and the voltage begins to drop, the potential on the dielectric segments nearest the exposed electrodes drop as well. However, the potential of the segments farther downstream remains constant. When the negative cycle ignites the plasma, the potential near the electrodes reverses signs and charges to high negative voltages. The potential farther away remains almost constant. When the plasma quenches and the voltage starts to rise, the segments near the exposed electrode follow. The segments farther away remain constant. The authors conclude that a permanent positive charge develops downstream. They calculate the longitudinal electric field and find an

almost constant value of 0.3 MV/m downstream. The location of maximum charge transfer happens 2 mm downstream and remains constant for different dielectrics. The total charge transfer within one cycle does not depend on frequency but rather on voltage. Similar configurations were used by He et al. and Font et al., who found similar results[4,27]. Font found little variation for the case of pure nitrogen.

Nichols and Rovey conducted pressure experiment with V-dot probes to determine the dielectric charge at different operating pressures[32]. The plasma actuator behaved similarly to the one by Benard et al[29]. Plasma length and power increased with decreasing pressure. The surface charging results for 1 atm relate well with the results by Enloe et al[31]. In this experiment the enclosed electrode was widened and results are available up to 45 mm downstream. The surface potential behaved similarly to the 1 atm case for pressures down to 321 Torr (0.42 atm). The characteristic constant positive potential is visible in each pressure data set. The potential near the exposed electrode follows the applied voltage. Below that pressure, the charging of the dielectric exceeds the width of the enclosed electrode and only a partial picture is available. At low pressure, the entire dielectric gains charge and follows the applied voltage. It is interesting to note that the charging of the dielectric continues farther than the visible plasma length.

2.1.5 Spectroscopy Measurements

The light emitted from the plasma actuator is caused by the de-excitation of excited species in air. Spectroscopy measurements determine the wavelength of the emitted light. The wavelengths correspond to certain de-excitation processes. A review of

research conducted on plasma actuators using spectroscopy measurements in given in this section.

Kozlov et al. gathered spectroscopy data for dielectric barrier discharges of two rounded metal electrodes with glass on both[33]. The group found that the data include lines from the excited molecule $N_2(C^3\Pi_u)$ de-exciting to $N_2(B^3\Pi_u)$ and the ion $N_2^+(B^2\Sigma_u^+)$ de-exciting into $N_2^+(X2\Sigma_g^+)$. The wavelengths for both are in the UV spectrum close to violet. The group used cross correlation spectroscopy to determine the reduced electric field using known Townsend functions. They found that the electric field in the discharge reached up to 280 Townsend (Td). The authors offer an explanation as to why the other excited states of nitrogen don't show up. The high pressure in DBD's makes reactions between the excited states of nitrogen and oxygen common. The other states don't have enough time to emit light because their collision cross sections with oxygen are larger. Starikovskaia, et al. conducted experiments on symmetric DBD actuators with 95%-5%, nitrogen-oxygen mixture[34]. They used an intensified charge coupled device (ICCD) to measure emitted wavelengths. Only the C state of excited nitrogen and the B+ state of ionized nitrogen was measured and analyzed. The group used an electron energy distribution function solved with a Boltzmann equation solver as well as electron cross section data to determine the reduced electric field for both the positive and negative cycle. The field of the positive cycle is in excess of 1000 Td, while the field of the negative cycle is around 600 Td.

Stanfield et al. conducted spectroscopy measurements on DBD actuators operating in air using a fast switching ICCD[35]. The camera was able to capture the differences between the two cycles. Again, only nitrogen states emitted light so the

standard wavelengths were used to calculate data. A Boltzmann equation fit was applied over the data to obtain the rotational and vibrational temperature of the excited and ionized states of nitrogen. Concentrations of both species increased as voltage increased. Excited nitrogen had a higher concentration during the negative cycle while ionized nitrogen had a higher concentration during the positive cycle. This supports velocity experiments that found a PUSH-push type of actuation. Rotational temperature for the N_2(C) state at the tip of the top electrode is 355 K during the negative cycle and 345 K during the positive cycle. The rotational temperature of the N_2^+(B) state is 620 K during the negative cycle and 420 K during the positive cycle. This difference in temperature may be caused by the acceleration of positive ions toward the exposed electrode during the negative cycle. In following experiments, Stanfield et al. found similar results[36]. The rotational temperature of the excited and ionized nitrogen were determined over an average area. Temperatures increase with applied voltage. Ionized nitrogen is always more energetic, the authors believe that an electric field present in sheaths can give ionized nitrogen more energy. Vibrational temperatures for excited nitrogen are around 2500 K for12 kV. Stanfield and Menart conducted more spectroscopic experiments to determine the electric field inside of micro discharges[37]. Usually the discharges occur at random locations but when there is a small gap between the electrodes the discharges tend to stay (not always) at one location. The authors used the opportunity to collect data on a single discharge for the negative cycle of a DBD actuator. A least squares fit with rotational, vibrational, and density parameters was used to approximate the distribution. Measurements show that near the exposed electrode the number density of excited and ionized nitrogen is larger than distributions farther away. The rotational temperatures in

that region reached 450 K for excited nitrogen. The rotational temperature near the electrode reached 1250 K but quickly lowered to about 850 K half a millimeter downstream. Vibrational temperature for excited nitrogen was around 3500 K. The reduced electric field was calculated at 300 Td near the electrode and 185 Td farther away.

Wu et al. conducted a spectroscopic analysis for different pressures[38]. They observed that at 45 Torr the plasma actuator began operating in glow discharge mode. The rotational temperature of nitrogen decreases slowly from 880 K at 1 atm until the pressure reduces to 45 Torr, at which point a large decrease in rotational temperature is observed, down to 345 K at 2 Torr. The vibrational temperature decreases a little from 3100 K to 2800 K and then sharply increases below 45 Torr to over 3500 K. The electron density and ratio were obtained from line ratios. Electron temperature is almost constant at around 1.75 eV until the transition to glow discharge, at which point the temperature increases to 3 eV. The density near atmospheric pressure is close to $6x10^{12}/cm^3$. At lower pressures the density decreases and then increases slightly during glow discharge. Ying et al. also conducted spectroscopy experiments and found that the rotational temperature of nitrogen depends on the gap distance between the electrodes[39]. The plasma becomes more filamentary after the separation. Rotational temperature for nitrogen increases from 440 K to 840 K when the electrodes are separated. The temperature does not depend on the actuator frequency.

2.1.6 Phenomenological Modeling

Up until now, the cited works were all experimental. These experiments were conducted to better understand the operation of plasma actuators and optimize their performance. This section summarizes research for modeling plasma actuators so that computer programs can be used to predict performance and help optimize the configuration.

Enloe et al. measured light intensity using a photo multiplier and found that the negative cycle was brighter[14,23]. In collaboration with the group led by Corke[12,13], they attempted to represent plasma actuators using circuit elements[23]. The initial model assumed the plasma was a combination of variable resistors and capacitors. Unfortunately, this model predicted the power law as quadratic. However, research shows the exponent is 3.5. The model was changed and is described in Ref. 22. The enclosed electrode of the plasma actuator was segmented into a number of sub-circuits that used Zener diodes to differentiate the positive cycle resistors from the negative cycle resistors. More than 100 sub-circuits are required to properly model the plasma actuator. However, the model is based on circuit elements so computers can solve it with ease. The model predicts 3.5 as the exponent and can check performance for different configurations. The current supplied to the plasma actuator matches the light intensity from experiments, which was found to intensify with stronger current. The data from the photo multiplier was used to calculate the speed of expansion of the plasma, which the model matches. Poisson's equation was used to solve for the forces above the plasma actuator. A FLUENT CFD simulation with the forces as input parameters calculated the induced flow

on an airfoil. The results agree with experimental data. Lift and separation angle increased and unsteady actuation performed better than the steady case.

Suzen et al. attempted to model the induced velocity of the plasma actuator by separating the electric force into two components: the external field, and the charge density[40]. The charge distribution was assumed to be a half Gaussian starting from the left edge of the grounded electrode. To solve the system, the Debye length, maximum charge density at the wall, and the scaling parameter for the Gaussian are required input parameters. The authors used PIV results to calibrate the model inputs. They were able to accurately predict the force distribution as measured from PIV results. The method requires a re-calibration for each plasma actuator. In a later publication, the authors removed the necessity to input the maximum charge by using the grounded electrode as the source of the charge[41]. The model became less dependent on experimental data but retained the ability to model induced flow.

Meijerink and Hoeijmakers conducted PIV experiments and used Suzen's model to calculate the force imparted onto the flow[42]. The PIV experiments showed that the plasma actuator induced flows up to 8 m/s. Suzen's model was solved using COMSOL Multiphysics. The results multiplied by 20 gave a good representation of the speed but the shape of the velocity profile was off. They used the results from the model as an input into a computational fluid dynamics (CFD) simulation. Eight actuators were placed around an airfoil and the induced velocities were calculated. The actuators performed well for flow reattachment and lift augmentation up to a Reynolds number of $7x10^5$. Maden et al. used PIV data and an empirical force model to describe plasma actuator

velocity fields[43]. They use a Steady Reynolds-Averaged Navier-Stokes (RANS) CFD method to simulate results. Their model matches well with experimental investigations.

Phenomenological models quickly calculate the forces or flow velocities produced by plasma actuators. The methods described above solve quickly and offer good agreement with experimental results. However, they do not properly capture the discharge effects. New insights into plasma actuator operation require plasma simulations.

2.1.7 Plasma Simulation

While fast photography, spectroscopic measurements, and flow velocities can help characterize actuators, simulations offer the unique ability to qualitatively and quantitatively study the plasma structure and strength. DBD simulations were used even before plasma actuators to help mostly with ionizer operation. Braun et al. performed simulations of microdischarges in air DBD's[44]. They used Poisson's equation in conjunction with the continuity equation to simulate the discharge. Monte Carlo techniques were used to calculate the equilibration time of electron energy and oxygen dissociation. Both equilibrations occur within a few picoseconds, which allows for the use of equilibrium relations. The pressure is raised to 2 bar to more accurately simulate a pressurized ionizer. The electric field inside the discharge can reach up to 600 Td. The electron density reaches up to $1x10^{15}/cm^3$. In another simulation, Braun models the two-dimensional structure of a discharge inside of a parallel plate DBD[45]. They determine the discharge has 4 phases. A Townsend ionization phase starts the discharge and evolves into a streamer. The steamer progresses towards the cathode and a cathode layer forms.

The electron and ion density are almost constant within the discharge except inside the cathode layer. The electric field weakens and the discharge begins to decay. Both simulations accounted for oxygen and nitrogen chemical reactions. The simulations lasted as long as the discharges themselves, that is tens of nanoseconds.

Plasma actuators operate on the principles of DBD. The simulations by Braun are not directly applicable because of the difference in geometry and pressure, but the results and simulation dynamics provide a stepping-stone. Simulations for plasma actuators have the added difficulty of induced airflow. Equilibration occurs in picoseconds, discharges need a few nanoseconds, but airflow manipulation occurs over millisecond time scales. In effect, a proper plasma actuator simulation must take into account the small structures in the nanosecond scale and run up to a 100s of microseconds or even a millisecond. The simulation would take too long to complete. Furthermore, the distances considered in the aforementioned simulations were on the order 1 mm. Plasma actuator simulation length scales should be on the order of a few centimeters. The larger simulation area further increases simulation time. Completing a full plasma actuator simulation would take too long to be practical; therefore plasma actuator simulation dimensions are reduced and voltage frequencies are increased.

Jayaraman et al. provide a good review of research into plasma actuator simulations[46]. The authors' model is 1 cm x 1 cm with 2 mm electrode lengths. The frequency is set to 10 kHz, and the model uses helium because of its simplicity. The discharge mechanism qualitatively matches those of real DBD's but the actuator is operated in a pull-push mode, which does not match experiments. Font simulated the discharge of plasma actuators assuming pure nitrogen[47]. The simulation area was 2 mm

by 1.5 mm with the bottom electrode spanning 1.25 mm. The top electrode has a thickness of 1 mm and protrudes 0.25 mm into the simulation domain. The simulation starts with a negative voltage and shows electrons streaming away from the electrode and into the dielectric. The plasma density reaches more than $1x10^{17}$ particles/m^3. The voltage switches polarity after 60 ns. At this point, electrons leave the dielectric and rush towards the exposed electrode. The plasma intensifies for positive applied voltages. The density exceeds $2x10^{18}$ particles/m^3. Ionization events continue well after 100 ns. The simulation does not include oxygen so the force production is wrong.

Orlov et al. expanded the dimensions of the previous simulation to 10 mm by 7.5 mm with a 4 mm encapsulated electrode[48]. Pure nitrogen was used during the simulation. The positive and negative cycles were investigated individually. The positive cycle showed a streamer propagating across the dielectric, while the negative cycle showed a more diffuse plasma. These results match well with fast photography, which show streamer discharges for positive voltages and diffuse structures for negative voltages. Boeuf et al. conducted a simulation in pure nitrogen using an implicit Scharfetter-Gummel scheme[49]. They simulated a positive voltage ramp separately from a negative ramp. During the positive voltage ramp, the plasma expanded throughout the dielectric in multiple streamers. The force applied to the neutrals was assumed to come primarily from the electrostatic force. The results show that the streamers applied a strong force over a short time period. The plasma showed a type of corona state between streamers. The force at this state was weaker than the streamer force, but it acted over a longer time such that it became the major contributor. During the negative ramp, multiple weaker discharges with weaker force distributions were observed.

The performance of plasma actuators depends on the oxygen content. Simulation presented above did not include that element. Likhanskii et al. included oxygen and the effect of negative ions in their simulation[50]. The frequency was set to 1 MHz and the simulation was run for multiple cycles. Both cycles produced a net positive force. The negative cycle was stronger but near the top electrode, the force pushed upstream. Positive ions attracted to the negative electrode pull the flow back. The authors believe this to be an inefficiency of plasma actuators. Boeuf et al. altered their simulation to include negative ions[51]. The plasma actuator operated at 5 kHz and either 10 or 25 kV. The force formulation included electric field effects as well as pressure gradients. The results show differences between the positive and negative cycles as well as the applied voltages. For 10 kV, the positive cycle was stronger but the current did not show the characteristic spikes associated with streamer formation. The 25 kV operation included current spikes during the positive cycle, which reduced the force applied. The negative cycle was stronger in that case. For both voltages, negative forces were observed close to the exposed electrode during the negative cycle. This matches the results from Likhanksii[50]. The surface potential was also calculated. They found that the dielectric followed the applied voltage near the electrode and weakened downstream. They did not find a constant positive region as was reported by experiments[31,32].

Simulations model the plasma discharge very well. They can simulate the streamer formation during the positive cycle and the more diffuse plasma during the negative cycle. Unfortunately, the large physical and time scale of DBD actuators makes it difficult to simulate experimentally realized actuators. However, they provide insights into the plasma dynamics and offer information that is difficult to measure otherwise.

2.2 Particle Image Velocimetry

PIV technique has been studied and used for more than 30 years and has improved with time. Adrian gives a good review of important concepts and achievements and characterizes PIV as the "accurate, quantitative measurement of fluid velocity vectors at a very large number of points simultaneously."[52] The words accurate and quantitative are very important to measurements techniques. It is these words that have guided PIV research. PIV has been used in multitudes of experiments and has evolved to be used in a large portion of fluid flow. This section summarizes investigations that have shaped PIV practice to its current state but focuses on the fundamental elements of the practice. Two other subsections will be included as research in those fields is pertinent to the current investigation. First, ensemble averaging is an investigation technique that allows PIV measurements for low seeding environments. Second, uncertainty analysis is important in any investigation and recently there have been many investigations into that aspect of PIV.

2.2.1 PIV: A Brief History

A brief history of PIV was provided by Adrian[52]. The author describes how PIV started and evolved through much of the early years. This section will focus mostly on work since the 1990's and digital particle velocimetry, which is the standard today. Perhaps one of the most famous works using digital technology for PIV was conducted by Willert and Gharib in 1991[53]. The authors used a digital video camera operating at 30 Hz to capture single exposure images and analyze them using cross correlation. The uncertainty of the system was characterized and it was determined that the system's best

performance was 0.01 pixels. However, this number is idealized, as particle pairs existed in both frames, stayed the same size, and moved uniformly. For an experiment, the mean velocity uncertainty was determined to be around 0.08 pixels with a standard deviation of around 0.26 pixels. These numbers have been used since then as the uncertainty of PIV measurements. The authors also showed that PIV reduces spatial wavelength determination for wavelengths less than the window size. This may be seen as a necessity to reduce window sizes but image density is more important than wavelength response in determining valid velocities; as such window size must be kept large enough to include enough particles.

Lourenco et al. introduced a new PIV setup using a digital camera connected to a PC with dedicated digital image hardware and a double pulsed Nd:YAG laser[54]. The laser pulse timing and the exposure time were capable of being varied, allowing the capturing of images at specific times and therefore, specific particle displacement. The setup was shown to accurately determine a wide order of velocities through a wall jet experiment. With the exception that they used auto-correlation instead of cross-correlation, this setup became the standard PIV setup for single camera systems. Adrian credits Lourenco et al. for convincing the Kodak company to manufacture a camera with an on-board frame buffer, which allows for successive images to be taken quickly

The use of cross-correlation in analyzing PIV images was studied extensively by Keane and Adrian[55]. It was shown that cross correlation leads to smaller erroneous correlation peaks due to having fewer peaks and limiting correlation of noise. It should be noted that cross-correlation does not significantly improve valid vector determination if the density is low. However, with proper seeding, cross-correlation performs better in

velocity fields with velocity gradients. The authors recommend that window sizes and seeding densities are chosen such that there are at least 10 particles in a window, the in-plane motion is less than a quarter of the window size, the out-of-plane motion is less than a quarter of the light sheet thickness, and the spatial displacement gradients are less than one particle image diameter per interrogation window length. These suggestions have been followed by the community to this day and represent the criteria for the initial analysis.

The purpose of PIV is to accurately determine the particle displacement. With the above recommendations for particle seeding and experimental setup it is possible to achieve a large yield of displacement vectors. Random noise, lack of particles in the region, reflections from surfaces, and the fact that cross-correlation is a probabilistic procedure, will result in spurious displacements. Many of these displacement vectors are easy to find with the naked eye since they contradict their neighbors in magnitude and direction. It would be too tedious, however, to manually go through each vector. As such, Westerweel compared three techniques that automatically check the vector field for any spurious vectors[56]. The global-mean method compares vectors against the mean of the entire set of vector data. The local-mean method compares vectors against the mean of the local vectors, for example a 3x3 set of vectors or a 5x5 set. The local-median compares possible spurious vectors against the median vector from their set of neighbors. The global mean test requires the most computation time and is the least effective. The local mean performs better and is more efficient. It was shown that the local median method is the best because of its low computation cost and its resilience to more than one

erroneous vector. Two wrong vectors do not significantly affect the median, but have a large impact on the mean.

Spurious vectors can be easy to find but accurate PIV results need to properly represent the flow within some uncertainty. Another paper by Westerweel looked at the precision of the PIV measurements to theoretically determine the best performance of PIV[57]. The probability density function is determined for combinations of Gaussian or uniform particles and Gaussian and uniform light sheets. In reality, the probability density function of particle intensities is more complicated than those used in simulations; however, the simulations are approaching experiments. The author calculated the error due to displacement as well as the particle image diameter and the image density. It was determined that the maximum error due to displacement is about 0.15 pixels. Image density data show that error is minimized for higher density images. The error for particle image diameter was found to have a minimum at a diameter of about 2 pixels. This agrees with other investigations[58]. The error increases for small particles due to the inability of the Gaussian interpolation to accurately determine the particle position and the peak locking effect from having particles smaller than one pixel. Peak locking occurs when the particle image diameter is less than one pixel, which disallows interpolation methods to determine the particle location with sub-pixel resolution. Peak locking leads to discrete displacement values between images and increases the measurement error. Centroid interpolation is less likely to remediate peak locking. Gaussian interpolation is the best interpolation for particle images down to below 2 pixels.

After the initial pass, the displacement information can be used to make better predictions and increase accuracy. To further increase accuracy, Scarano[59], and Scarano and Riethmuller propose multigrid approaches with image deformation techniques[60,61]. Using the displacement vectors as a reference, the interrogation windows can be shifted to follow the particles and better estimate the velocity field. Grid refinement is also possible. Since the displacement of the particles is known, it is possible to refine the grid to include fewer than 10 particle pairs and still get a valid peak by matching the particle displacement with that of the window. Originally the shift was limited to integer pixel values but has been extended to sub-pixel shifts. Higher order effects take into account the gradient in the velocity fields and deform the interrogation window appropriately to decrease loss of pairs. These higher order methods can be computationally expensive but are capable even in turbulent flow.

A review of the fundamentals is given by Westerweel, who includes details about seeding, imaging, correlation, and validity[62]. A more detailed analysis of PIV can be found in books by Raffel et al.[63] and Adrian and Westerwell[64] among others. Still, PIV experience is best earned in the laboratory with practice.

2.2.2 Particle Size and Seeding, and Sum of Correlation

Particle selection is an important first step in any PIV experiment. For experiments conducted in air, the diameter of the particle must be small enough to accurately follow the flow yet large enough to scatter enough light for a good signal to noise ratio. Melling offers a good review of analysis for the suitability of particles based on their density and diameter for PIV experimentation[65]. The response of the particle to

changing flow velocities is characterized using the Stokes number given in Equation (2-1)

$$Stk = \frac{\omega \rho_p d^2}{18\mu} \tag{2-1}$$

A good particle has a frequency response that is much greater than ω, the characteristic oscillation frequency present in the fluid flow. For plasma actuators, ω is the operating voltage frequency. A Stokes number much less than 1 is desirable for accurate PIV results.

The diameter is more important than the density for frequency response. However, it plays an even more important role for intensity of light scattered. There are two relations for light scattering off a particle. First, if the particle diameter is larger than laser wavelength, the scattering cross section is proportional to the square of the ratio of particle diameter to laser wavelength, $(d/\lambda)^2$. Second, if the particle diameter is smaller than the laser wavelength, the scattering cross section is proportional to the ratio, of diameter to wavelength, raised to the fourth power $(d/\lambda)^4$. For larger particles, increasing the diameter by a factor of 3 increases the scattering cross section by an order of magnitude. Neodymium doped lasers operate near the green 530 nm wavelength. A 1.6 micrometer particle has a cross section 10 times higher than a 530 nm particle. The increase in intensity leads to a better particle recognition by the software and hence a better signal to noise ratio. For smaller particles, decreasing the diameter to half that of the wavelength reduces the scattering cross section to just 6% as compared with a diameter matched to the wavelength. Adrian and Yao performed their own experiments with different camera settings and they too found two power law dependencies with

particle size[66]. Care must be taken to ensure that particles can be sensed by the camera should there be a need to reduce the particle diameter below the wavelength value.

Particle image diameter can be a source of significant error in PIV, if its value approaches unity. Westerweel reviewed the error due to particle image diameter[62] and concluded that estimation error is minimized for particle image diameters between one and three pixels. For diameters smaller than one pixel, error increases more quickly than for diameters larger than three pixels. The small diameter error is caused by pixel locking, a discrete movement in the image plane that doesn't allow for accurate sub-pixel interpolation. As such, displacement errors can quickly increase to as much as one pixel. Pixel locking can be avoided by using diffraction limited optics or larger particles.

In general, for the first interrogation of an image, 10 or more particles should be present in an interrogation window to give an accurate first result. This can be problematic if an adequate seeding density cannot be achieved. This scenario is often the case for experiments with a high magnification that look at small size flows like microchannel PIV experiments. In microchannel flow, the size of the interrogation region is small and so it is difficult to achieve a suitable seeding density. Lindken et al. give a good review of micro PIV guidelines and experiments[67]. Particle selection is important and to achieve accurate results, ensemble averaging, also called sum of correlation, is imperative.

Santiago et al. were the first to use ensemble averaging to account for Brownian motion in microfluidic flows[68]. However, Meinhart et al. first described the technique as a way to calculate the average velocity in time-averaged velocity fields[69]. The authors describe three methods for averaging velocity information for steady flow or phase-

averaged flow. PIV has three stages where summation and averaging can occur: the image capture, the correlation, and the peak detection or velocity determination. The most popular method of calculating the average of multiple time series is to individually find the velocity vector for each set and then calculate the mean and standard deviation. This allows the user to find the average flow speed and estimate the flow variance. It is also possible to sum the intensity values of the images to form one image. This method can be useful when seeding is low. Essentially, the separate images are combined to create a new image that includes more particles. This artificially increases the particle image density and the probability of finding the correct peak. However, this method increases noise at a faster rate and is detrimental if too many images are summed together. The third method sums the correlation planes for the image sets. The vector is then determined from one correlation plane that is the sum of all correlation planes. As such, this method is named sum-of-correlation, or ensemble averaging. The authors compare the three methods using experimental data of a steady microchannel flow with low particle seeding. Sum-of-correlation performed better than the other methods and even approached the theoretical flow results after only 5 image correlation summations.

Ensemble averaging can be used to calculate the average velocity for flows that are steady or for phase locked images. Individual correlation maps are calculated normally. In low seeding conditions, individual maps may not have enough particles or even any particles. Therefore, erroneous peaks will populate the correlation map in random locations. When many maps are summed together, the random erroneous peaks do not sum with each other, while the proper displacement peaks will always sum. After summing enough images the true displacement peak prevails over the random peaks and

the map has only one peak. With the use of window shifting and grid reduction techniques described above, ensemble averaging can provide flow details for smaller window sizes

There is no upper limit to the number of images that can be used in ensemble averaging as long as the flow is steady or phase locked. Window size can be reduced by increasing the number of images, which leads to a higher vector density and a more accurate representation of the flow. Single pixel ensemble averaging is the extension of ensemble averaging to a resolution of one vector per pixel. This technique was first introduced by Westerweel et al. and requires the use of thousands or tens of thousands of images[70]. The technique relies on a two-point ensemble correlation and is essentially the reduction in window size to one pixel. The authors compared ensemble averaging and single pixel ensemble averaging using synthetic and experimental data. They found that the single pixel technique gives superior vector resolution but is noisy for the low speed section of flows. More images can compensate for noise. The drawbacks of the technique are the large number of images necessary and that the flow must be quasi-steady or periodic and phase locked. Furthermore, the results apply only to the average flow field and cannot provide information about the instantaneous flow field.

Microfluidic flow faced a problem with high speed flows. It was difficult for small interrogation regions to capture large particle displacements. Kähler and Scholz extended single pixel ensemble processing to speeds up to 350 m/s by using cameras with interframe times of 75 ns[71].The Ensemble correlation was later extended to macroscopic application with fluctuating components by Willert[72]. The author applied ensemble processing algorithms to subsonic and transonic jets to calculate the average flow field by

starting with a coarse grid and then refining to an effective window size of 24 x 24 pixels. Processing time was decreased by summing the Fourier transforms instead of the correlation planes. Two peaks were noticed in the shear regions of the flow showing that ensemble averages could distinguish between the different velocities, but it is wrong to attribute only one of those velocities as the flow velocity.

2.2.3 Uncertainty Analysis in PIV

PIV research outlined above focused on determining the capabilities of the technique. As such, the uncertainties were calculated for the method not the flow. Velocity fluctuations are a part of every experiment and the fluctuation of velocity is important in calculating Reynolds stresses, or quantifying turbulence. To determine the velocity fluctuation, the uncertainty associated with PIV must be quantified and removed from the total uncertainty.

PIV uncertainty quantification has become a major research topic in recent years. In 2012, Timmins et al. proposed a more general method of estimating uncertainty[73]. The method uses the particle image diameter, the particle density, the displacement and the local shear to determine a 4 dimensional "uncertainty surface." The surface is initially determined by calculating the error in tens of thousands of simulated images. Tests with simulated flow showed good agreement with laminar flows, but the method is not universal as it only takes into account 4 sources of error while PIV measurements can have even more sources of error that lead to the method incorrectly determining the uncertainty. Good agreement was found when the uncertainty surface was applied to a rectangular jet experiment with wire anemometer measurements for comparison.

Sciacchitano et al. proposed another method to determine the uncertainty by matching images[74]. The method uses the calculated displacement vector to shift the images back and overlay them. Individual particles should lie close to each other. The difference between the particle centers is calculated and used to form a Gaussian estimate of the disparity between the particle locations. The mean and standard deviation are measures of systematic and random error. The method requires at least 6 particle pairs to match and does not work well with pixel locked particles. Simulated images were used to test the algorithm and it was determined that the uncertainty matched well with the computed error. A water jet experiment was also used to test the method and the relative accuracy of the method was determined to be about 90%.

Charonko and Vlachos proposed to estimate the uncertainty using the cross-correlation peak ratio between the main peak and the secondary peak for both standard cross-correlation and robust phase correlation[75]. The authors used synthetic images to find the correlation between the peak ratio and the uncertainty. This technique does not require analyzing images and is computationally fast. When robust phase correlation was used, the error estimation was accurate but the method is not as accurate for standard cross-correlation.

Weineke proposed the correlation statistics method[76]. The method starts by matching images, much like the method by Sciacchitano et al.[74]. A residual is used to best determine the location of matching and a function can be defined with a maximum at the location of best match. For a perfect match, the function is symmetric, but in reality, the function will be misshaped due to error in the algorithm. The method takes into account the contribution of each pixel to this asymmetry to determine the standard deviation for

the uncertainty of the measurement. Since the writing of this paper, this method has been incorporated into the LaVision DaVis software package.

To test and compare the different methods described above, Neal et al. conducted a jet flow experiment that used a standard PIV set up, a high dynamic range PIV set up (HDR-PIV), and a hot wire anemometer to determine the air speed[77]. Taking the hot wire anemometer measurement as the truth for one point of the flow, the standard PIV and HDR-PIV systems compared favorably, with the latter performing better, as expected. The HDR-PIV velocity field was used as a comparison with the standard PIV results. The database was built using error measurements stemming from variable seeding densities, variable particle image size, out-of-plane motion, and velocity gradients.

Sciacchitano et al. used the experimental results from the database to compare the recent methods for uncertainty determination[78]. Each method was tested using the uncertainty coverage method, which calculates the percentage of measurements that lie within the uncertainty bands. One standard deviation was chosen as the uncertainty bound. The correlation statistics and particle disparity methods performed well in flows with gradients and small particles. The uncertainty surface method was superior in low seeding settings. Overall, the image matching methods were more sensitive to fluctuation in the uncertainty.

While these methods advanced PIV uncertainty research, none of them were designed for use with ensemble averaging in mind. Kahler and Scholz (Ref. 71) offer a qualitative theoretical treatment for uncertainties using ensemble processing. The authors argue that the correlation peak for single pixel ensemble averaging contains information about the Reynolds stress. Since ensemble averaging sums the correlation planes, the

final product contains information related to the variance of the flow. However, the correlation peak contains effects from the particle image diameter for both frames, noise from the camera, and any velocity gradients present in the interrogation windows. They assume particle diameters and noise signals have Gaussian shapes and are able to, with assumptions, calculate the correlation diameter.

Scharnowski et al. also present a theory for estimating Reynolds stresses from the correlation plane of ensemble PIV[79]. The method relies on deconvolving the probability density function from the correlation peak by removing the effect of the particle image diameter and taking into account the velocity gradient. The authors do not take into account the effect of noise, out-of-focus particles, loss of pairs, or other sources of error. The number of image pairs plays an important factor in the error estimation. For 100 pairs the uncertainty was found to be around 0.6 pixels, while for 100,000 pairs the uncertainty was found to be around 0.1 pixels. The effect of velocity gradient is found to be important for values larger than 0.1 pixel/pixel. A correction is offered for gradient flows and the theory is validated with computational and experimental results. Single pixel ensemble averaging is found to give much sharper results for Reynolds stresses compared to window interrogation techniques that act as a low-pass filter. A method similar to this one is used in the current work to calculate uncertainty.

2.3 Dusty Plasma

Chapter 1 gives a brief introduction to plasma as a state of matter and its relevant scales. The introduction is for a simple and almost perfect state of plasma. Special fields exist in the study of plasmas that deal with more complicated and specialized cases.

Dusty plasmas is one of those fields. A brief review of dusty plasmas is given in the current work. The focus is on particle charging theories and their dependence on pressure, or collisionality between charged and neutral species. A particle in contact with plasma attains a charge due to collisions with ions and electrons. Because the particle is not attached to a circuit, its potential value is floating and the average current to the particle at steady-state is zero. The current from positively and negatively charged species must equal each other. Since current depends on velocity, collisionality plays an important role in charging dynamics. This section gives a brief overview of particle charging dynamics at low and intermediate pressures. The focus is placed on the dynamics in high pressure plasmas. A more thorough review of dusty plasma processes is given by Khrapak and Morfill as well as references within[1].

2.3.1 Low and Intermediate Pressures

Orbital Motion Limited (OML) theory is the most popular charging theory for dust particles in low pressure plasmas. Allen gives a detailed review of the theory and talks about its limitations[80]. OML theory derives the particle potential by calculating the current to the particle from incoming charged species using conservation of energy and angular momentum. The theory does not take into account collisions, which can greatly affect the velocity of ions and lead to a velocity value outside the allowable range. A review of the full Orbital Motion theory is given by Kennedy and Allen[81]. The full theory is derived from first principles and compared to OML theory. They determine that the OML solution approaches the full Orbital Motion solutions for small particle radii. Still, the simplicity of OML is attractive despite its limited validity.

If a collision occurs, the ion would lose energy and momentum and hit or orbit the particle. A simple theory was introduced by Allen, Boyd, and Reynolds (ABR theory)[82]. The theory is also known as radial motion theory, and it assumes that the ions only travel radially toward the particle. This motion increases the ion current to the particle and decreases the charge. The resulting charge can be viewed as a minimum value in a standard ion-electron plasma. ABR theory better predicts particle charging for pressure ranges where collisions can occur near the particle. An experiment was conducted on the ISS wherein a plasma tube was injected with nanoparticles to study dusty plasma dynamics[83,84]. The pressure for the experiment was varied between 20 and 150 Pascals. The dust charge was determined from a force balance for lower dust densities or linear wave dynamics for higher dust densities. The results showed that the dust charge was lower than expected from OML calculations. This is due to the increased pressure and ion-neutral interaction. A theoretical expression from Lampe et al. was used to calculate the dust charge[85]. This method uses a correction for higher pressures by taking into account the trapped ions inside a sphere of influence. The analytic approximation matches nicely with the experimental data, especially with smaller particles.

The previous dusty plasma experiment was expanded to a pressure of 500 Pa[86]. The results show the dust charge has a minimum at about 200 Pa for the setup. Higher pressures lead to higher charge due to ion-neutral collisions. The weakly collisional analytic expression is used to fit the lower pressure data. The hydrodynamic analytic expression is used at higher pressure. An interpolation using the two expressions matches the data nicely in the middle. At lower pressures OML properly predicts the current to the particle. As the pressure increases, collision between ions and neutrals redirect more ions

toward the particle, increasing the ion current and decreasing the particle charge. At even higher pressures, the numerous collisions between ions and neutrals limit the mobility of the ions and decrease their current towards the particle.

2.3.2 Hydrodynamic Regime

As pressure increases, the ions' mean free path reduces and their motion becomes mobility limited. Plasma actuators operate at these pressures. Ion current to the particle decreases and electrons charge the particle more negatively. Chang and Laframboise derive an expression for the current to a probe in a highly collisional plasma made up of electrons, and positive and negative ions[87]. Their work is based on the diffusion and mobility equations coupled with Poisson's equation. They determine expressions for each plasma species for arbitrary probe shapes. The different charging mechanics over wide pressures were investigated by Gatti and Kortshagen, who derived an analytic expression for particle charging for a wide range of pressures[88]. They use OML theory for low pressures, ion flux into a capture radius for medium pressures, and hydrodynamic limits for high pressures. Current equations for different pressures were weighted by the probability of collision and summed to give an expression for wide pressure ranges. Khrapak et al. have derived expressions for particle charging in highly collisional plasmas[89]. Two regimes are studied. First, both ions and electrons are limited due to collisions. Second, only the ions are limited, while the electrons follow OML theory. Results agree with those by Chang and Laframboise for the collisional case. An analytic expression is derived for the charge fluctuation due to the discrete and random nature of particle charging. It is shown that the electrostatic potential of a particle decays like 1/r in

collisional plasmas as opposed to the exponential decay of the Debye-Huckel theory. These results were complemented by a linear kinetic model analysis that takes into account ion-neutral collisions[90]. Flowing ions due to external electric fields have been analyzed and it was found that ions can be absorbed from both upstream and downstream directions[91]. More interestingly, the particle charge does not depend on the electric field until the ions reach large supersonic speeds. Therefore, particle charging is independent of electric field strengths present in plasma actuators; therefore the charging mechanisms mentioned above can be applied without corrections.

2.3.3 Ion Drag Force

Ion motion, caused by external electric fields, can impart momentum onto the particle through collisions and long range Coulomb forces. Ivlev et al. give a review of works regarding ion drag force until the early 2000's[92]. Two approaches are discussed in detail. The pair collision approach is based on the interaction of ions and dust particles and works best for low pressure plasmas. The kinetic formalism approach is algebraically more complicated but is more accurate for higher pressures with low speed and high speed flows. Since plasma actuators operate in a high-pressure regime, the kinetic formalism method is of more interest. Khrapak et al. apply linear response formalism to an absorbing particle in highly collisional plasma and determine that at low speed flows the ion drag force decreases and can even reverse direction[93]. However, high speed flows and direct collisions are not considered. The reversal of direction is in agreement with Monte Carlo simulations of particle charging in plasma at 150 Pa[94]. Chaudhuri et al. extend the linear response analysis by including the electron drag force in the

hydrodynamic regime[95]. The authors find an equivalent charge that describes the total force in an external electric field. The equivalent charge is very similar to the actual charge, further implying that drag forces are weak in highly collisional plasmas. Furthermore, the force due to collisions is found to be small compared to the induced Coulomb force from streaming ions and electrons.

In another paper, Chaudhuri et al. determine the electrostatic potential of an absorbing particle in a collisional plasma[96]. Linear formalism is used and the potential function is found to have two parts. The first part is the standard Debye-Huckel potential and the second part relates to absorption and collisions. The electric field is calculated from the potential function and depends on electron to ion temperature ratio, ion thermal Mach number, and collisionality. The ion drag force is found to decrease from the effect of ion absorption and the electric field always points toward the grain farther downstream. Near the grain, a positive potential can exist if the thermal Mach number, collisionality, and electron to ion temperature ratio are high. Plasma actuators operate in high collisionality plasma with high electron to ion temperatures, but the thermal Mach number is low. Plasma production near the particle was accounted for in a later paper[97]. Ionization strongly impacts the ion drag force. Strong ionization near the particle can lead to a reversal of the ion drag force and in general weakens the force acting on the particle. A review of these processes is given by Khrapak et al[98].

For plasma actuator PIV experiments, the ion drag force appears to be too weak to make a substantial difference in the dynamics of the particles. Highly collisional plasmas with strong ionization and loss mechanisms, along with high electron to ion temperature ratios and low ion speed, couple to reduce the effect on the ion drag force. It may be that

in some cases the force switches directions, but the amplitude of the force would be small compared to the strong electric field and aerodynamic forces present in operating conditions.

2.3.4 Electronegative Plasma

Usually plasma is composed of electrons and positive ions, with electrons having a higher mobility due to their low mass; however, certain elements, like oxygen and fluorine, are electronegative, which increases the likelihood of electron attachment. Electronegative plasmas have two species of ions, positive and negative, and the behavior changes from the standard electron-positive ion plasma.

Franklin gives a review of research into electronegative plasma till the turn of the century[99]. Electronegative plasmas have different dynamics due to the third species and can have electron-ion sheaths with ion-ion cores due to limited mobility of negative ions. Oxygen is special because of its numerous reactions with itself and other elements. Klumov et al. investigated the effect of adding small quantities of oxygen in a dusty argon plasma[100]. Negative ions, formed by electron dissociative attachment, significantly change dusty plasma dynamics. Both particle charge and electric field strength are reduced due to the transformation from an ion-electron plasma to an ion-ion plasma. Ion-ion plasmas have slower time scales and longer length scales due to the restricted mobility of ions compared to electrons. Mamun and Shukla investigate the effect of negative ions on particle charge in low pressure discharges[101]. They consider a quasineutral plasma and two regimes for negative ions, streaming and Boltzmann. When streaming, negative ions are assumed to have supersonic velocities and they find that the

particle charge decreases and can be nullified for large densities of negative ions. Boltzmann ions lead to similar results. The particle charge is the most important element in a dusty plasma; negative ions play an important role in the dynamics.

Usually particles charge negatively due to the higher mobility of the electrons; however, recent experiments in the night sky have detected positively charged particles[102]. A sounding rocket test was conducted in the northern sky between 80 and 90 km altitude. Positively charged particles were observed and believed to be larger than 2 nm and have a density of 3 g/cm^3. The region had a low number of electrons compared to positive ions. Quasineutrality arguments led to a negative ion density that was 40 times higher than that of the electrons. Kim and Merlino conducted an experiment in low pressure plasma with K+ ions and SF6- ions[103]. Theoretical arguments from OML theory predict that positive dust charge can exist if there is a large population of negative ions that are less mobile than positive ions, hence the choice of K and SF6. Langmuir probe measurements provided plasma potential information and glass microspheres were used as particles. It was shown that for high partial pressures of SF6 the plasma potential drops due to the lack of electrons and the low mobility of SF6-. In those conditions, particles can charge positively.

Electronegative species change the charging dynamics in dusty plasmas. Plasma actuators operate in air with large amounts of oxygen, an electronegative element. Particles immersed in atmospheric plasma interact with a multitude of ion species including negative oxygen ions. PIV experiments of plasma actuators need to account for the charging effects on the particle to accurately determine the velocity field.

Chapter 3: Experimental Set Up

The experiment consisted of setting a plasma actuator in a quiescent flow environment and conducting PIV measurements with precisely measured nanoparticles. The quiescent flow experiment was modeled after Durscher and Roy, who placed a serpentine plasma actuator in a quiescent chamber and conducted Stereo PIV experiments[104].

In the present experiment, a high-speed single camera system is used to measure the velocity field of a standard DBD plasma actuator seeded with monodisperse polystyrene nanoparticles. A timing circuit was assembled to synchronize the high-speed PIV system with the plasma actuator and quickly collect data for 25 phases. This chapter expands on the equipment and is divided into three parts dealing with the instrumentation, the seeding apparatus, and the timing circuit.

3.1 Instrumentation

3.1.1 Plasma Actuator

The plasma actuator was constructed using three Kapton CR® sheets of 3 mil thickness adhered together. Kapton CR was chosen for its high breakdown voltage and low dielectric constant. Copper tape was used to construct the electrodes, which were 6 inches long and 3 mils thick. The bottom electrode was 1 inch wide; the top electrode was half an inch wide. There was no gap between the electrodes (parallel to the flow), but they were offset from each other (perpendicular to the flow) by an inch so that their end corners were not near each other. Practice has shown that plasma actuators burn through

their dielectric at locations of strong electric fields, like corners and points. To extend the life of the plasma actuator the corners near the opposite electrodes were rounded to decrease the electric field and plasma generation as shown in Figure 3-1. Figure 3-2 shows the equipment and the signal path from the signal generator to the plasma actuator. High voltage, Kapton insulated wires were soldered onto the electrodes at opposite corners and connected to a CMI 5525 step-up high voltage transformer, with the bottom electrode grounded and the top electrode connected to the high voltage terminal of the transformer. A Keithley 3390 signal generator created the sinusoidal signal input for the EPX4000 Behringer amplifier. The

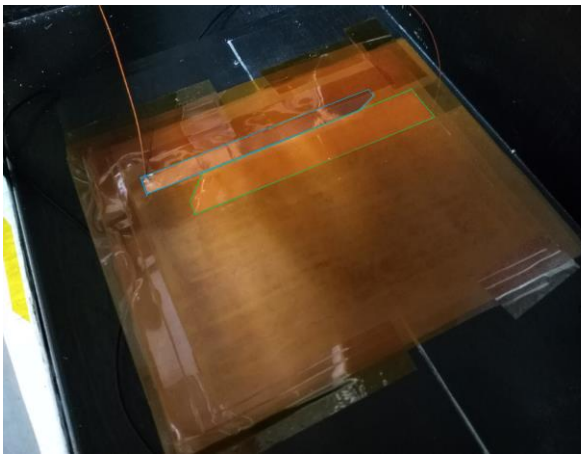

Figure 3-1. The plasma actuator used for experiments.

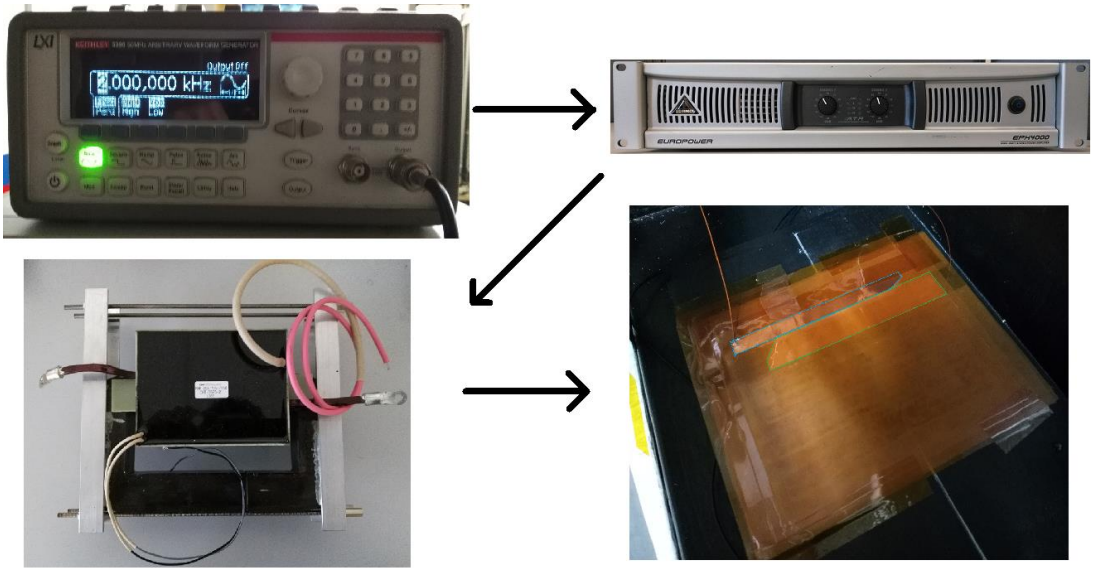

Figure 3-2. High voltage generation equipment. The signal generator is pictured on the top left, the amplifier is pictured on the top right, the high voltage transformer is pictured on the bottom left, and the plasma actuator is on the bottom right.

amplifier was set to stereo mode with side-A powering the high voltage transformer. Throughout all experiments the frequency and voltage powering the plasma actuator were set to 2 kHz and 4.5 kV_{rms} (12.7 kV_{pp}). Figure 3-2. High voltage generation equipment. The signal generator is pictured on the top left, the amplifier is pictured on the top right, the high voltage transformer is pictured on the bottom left, and the plasma actuator is on the bottom right

3.1.2 Quiescent Enclosure

The plasma actuator was placed inside an enclosure to perform quiescent flow experiments and control the environment as shown in Figure 3-3. The floor, ceiling, far side wall, and back wall of the enclosure were constructed with 3/4 inch wood panels for rigidity and support for the seeding apparatus. The wood was painted matte black to minimize the effect of reflections. The front panel was made of glass to allow the laser sheet to shine through. The near side panel was made of Polyethylene terephthalate

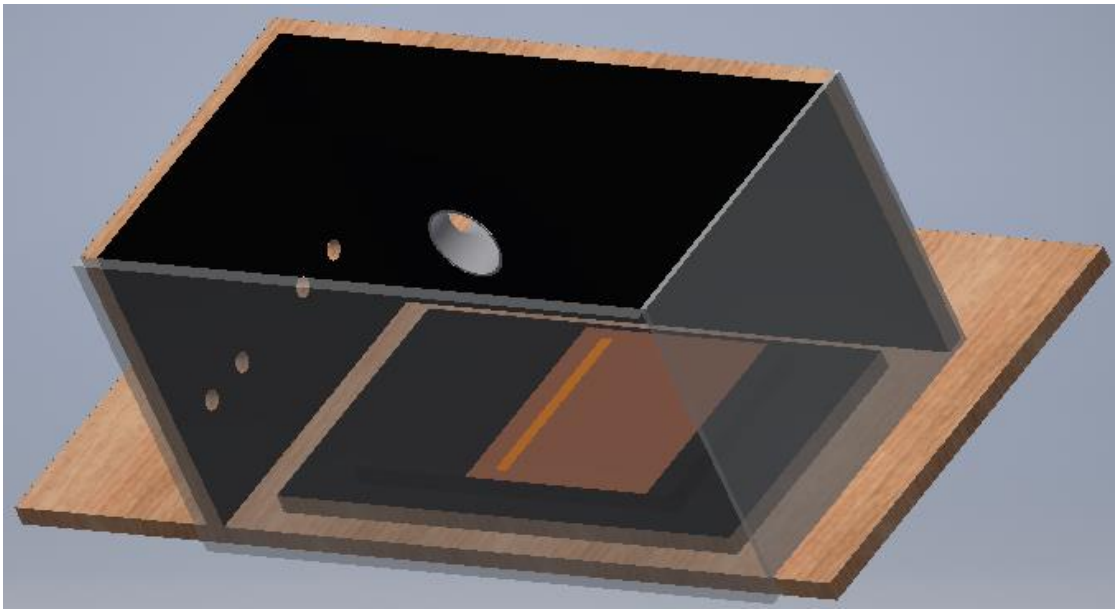

Figure 3-3. 3D CAD model of the enclosure used for experiments.

(PETG) for chamber rigidity, and transparency for the camera. The PETG panel was screwed to the back wood panel and adhered to the floor and glass panel with silicon. The glass panel was adhered to the floor, far side, and PETG panel with silicon. The top of each panel was lined with foam insulation to form a seal with the top of the enclosure, which was removable to allow access to the chamber. The chamber was 2 feet long and 1 foot wide and tall. The plasma actuator was placed at the center, facing the glass front. The plasma actuator was raised 1.5 inches above the floor through the use of a pedestal to allow for easier aligning of the laser and mitigate the effects of the silicon at the bottom of the glass panel on the laser sheet. To properly seed the chamber, four ¾" holes were drilled into the back panels to allow for inlet and one 3" hole was drilled in the back wall as the outlet for particles. Three leveling feet were attached to the base of the chamber to allow for leveling the plasma actuator with the PIV system.

3.1.3 PIV System

Figure 3-4 shows the PIV hardware. Experiments were conducted using a Litron LDY 304 Nd:YLF dual cavity pulsed laser operating at 527 nm. The laser firing frequency was set to match the plasma actuator at 2 kHz, well below its 10 kHz limit, and the energy output was maintained at 30mJ/pulse (100%) for both beams for all experiments. Images were captured using a Vision Research Phantom v641 12-bit high speed camera with 64 GB of onboard memory. The camera was capable of capturing 725 double images per second at the full resolution of 2560 x 1600 pixels. The sensor resolution was binned down to 2048 x 676 pixels to increase the capture rate to above 2000 double images per second.

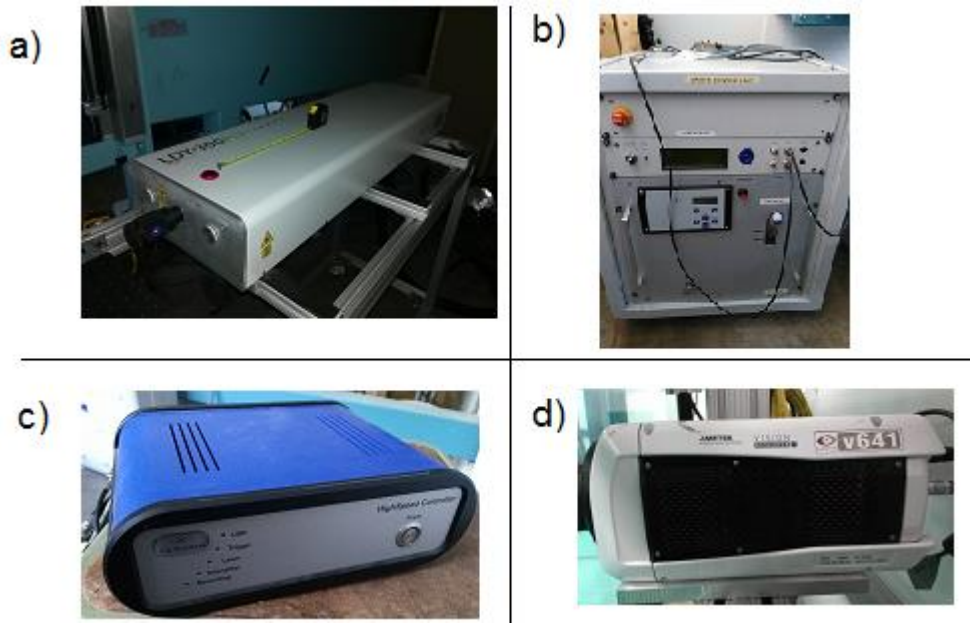

Figure 3-4. PIV hardware, a) laser head, b) laser power unit, c) high speed controller, and d) camera.

The laser was mounted on an 80/20 table; the tape measure is extended one foot for scale (Figure 3-4 a). The laser power unit provided cooling and power for the laser head. A LaVision high-speed controller handled the timing and connection between the laser and the computer. A 200 mm objective Nikon lens was mated to the camera to provide the magnification required to image the small area in front of the top electrode. Figure 3-5 shows a 3D CAD rendering of the chamber and the PIV system. The small red area, at the intersection of the plasma actuator top electrode and the laser sheet, is the camera field of view.

The viewing area spanned 13.5 mm horizontal and 7.5 mm vertical for a magnification ratio of 0.955. The LaVision high-speed controller was updated to software version 2.0 and the laser and camera timing were connected to the plasma actuator signal. The laser beam went through a spherical and cylindrical lens system to create a 2 mm thick laser sheet at the plasma actuator, with the laser sheet aligned perpendicular to the

middle of the top electrode. The camera was aligned perpendicular to the laser sheet and calibrated using a LaVision calibration plate. The chamber was situated on adjustable pivoting feet, the camera was placed on a tripod, and the laser was situated on an 80/20 table with adjustable feet; all three were leveled to within 0.1 degrees using a digital level.

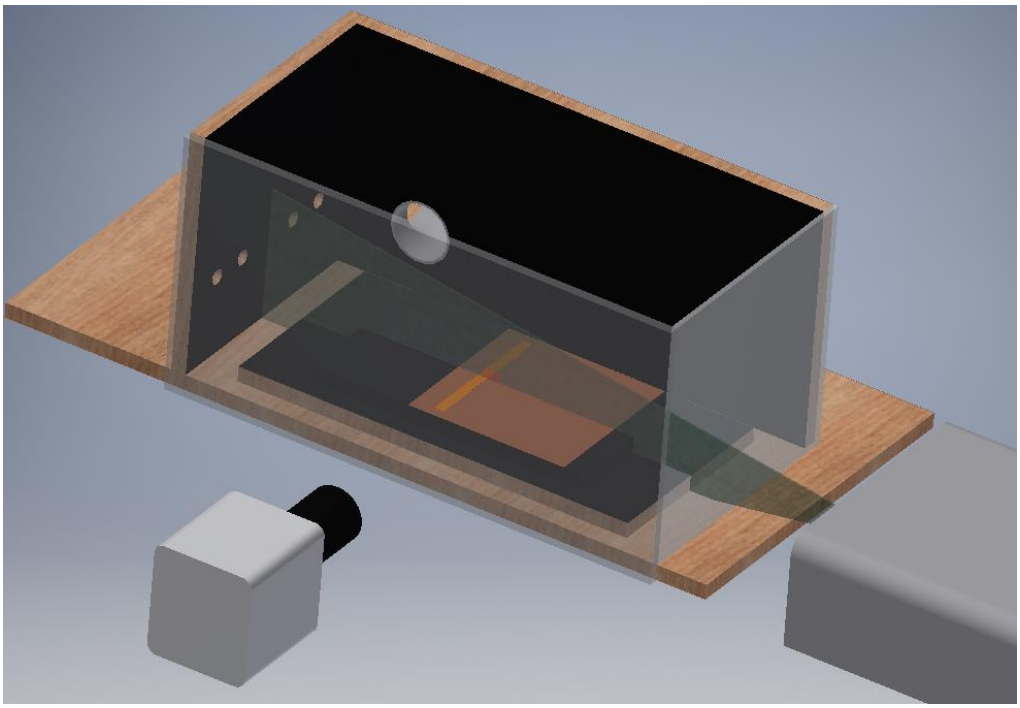

Figure 3-5. Laser, camera, and chamber setup. The small red area on the laser sheet near the electrode is the camera field of view.

3.2 Seeding and Humidity

Monodisperse nanoparticles are necessary to determine the charging effects in plasma actuators. Polystyrene spheres were chosen as the seeding particles because of their precise size. They can be manufactured from 50 nm to more than 10 um with a 3% tolerance on the particle volume. A total of five particle diameters were chosen for the experiment: 300 nm, 500 nm, 700 nm, 900 nm, and 1250 nm. The range of particle sizes

represents the limit of what can be used for PIV experiments with a 2 kHz flow oscillation. Table 3-1 shows the response times, Equation (1-4), and the Stokes number, Equation (2-1), for a 2 kHz oscillation for each particle diameter. Air viscosity was

Table 3-1. Response frequency and Stokes number for chose particle diameters.

	Particle Diameter [nm]				
	300	500	700	900	1250
f_p [MHz]	3.52	1.27	0.65	0.39	0.20
Stk	$5.6\text{x}10^{-4}$	$1.6\text{x}10^{-3}$	$3.1\text{x}10^{-3}$	$5.1\text{x}10^{-3}$	$9.9\text{x}10^{-3}$

assumed to be $1.846\text{x}10^{-5}$ kg/(m-s). Every particle has a Stokes number of much less than unity. Even the 1250 nm diameter particle has a Stokes number of 0.01 and should therefore follow non-charged flow with great accuracy.

3.2.1 Nebulizer and Heater

A combination of nebulizers, heaters, and coolers were used to seed the chamber. The DeVilbiss Pulmoneb LT nebulizer created a mist of droplets with suspended particles. It has a 10 ml container and a nebulization rate of 0.15 ml/min. It is necessary to ensure that each droplet only has, at most, one suspended particle. This reduces the chance that two particles adhere together and form a larger particle with a different effective diameter. The particles were purchased in 10 mL containers of deionized water with a concentration of 25 mg/mL, which was too large. The concentration was converted to a number density using the material density for polystyrene, 1.05 g/cm^3, and the known particle diameters, and is given in Equation (3-1),

$$n_{sol} = \frac{25}{1000 * V_{part} * \rho_p} \tag{3-1}$$

where V_{part} is the particle volume (mL), the solution number density is n_{sol} (1/cm^3), and ρ_p is the particle density (g/cm^3). The mean molecular aerodynamic diameter (MMAD) for the droplets created by the nebulizers was 5 µm, which was set to the desired mean distance between the particles while in deionized water. To that effect, distilled water was added to the nebulizer containers to reduce the concentration of particles and increase the interparticle distance to the desired value. Given the droplet MMAD and the particle diameter, the particle density inside the nebulizer container was calculated using Equation (3-2). The necessary solution volume was calculated using Equation (3-3)

$$n_{neb} = (MMAD + d)^{-3} \tag{3-2}$$

$$V_{sol} = \frac{n_{neb} * 6}{n_{sol}} \tag{3-3}$$

The number 6 refers to 6 mL and is used as a safety factor. Enough distilled water was added to fill the 10 ml container, but the solution volume was calculated using 6 ml so that the minimum interparticle distance remained above the calculated value. Table 3-2 shows the calculated density and volume values. Each particle had its own syringe and needle to avoid cross contamination. A precision 100 µL syringe was used for the 300 nm particles and the more popular 10 mL syringes were used for the other particles.

Table 3-2. Particle number density and volume values.

	Particle Diameter [nm]				
	300	500	700	900	1250
Solution Concentration [mg/mL]			25		
Solution Number Density [x10^{11}/cm^3]	16.8	3.64	1.33	0.62	0.23
Nebulizer Number Density [x10^9/cm^3]	6.72	6.01	5.40	4.87	4.10
Necessary Solution Volume [mL]	0.024	0.099	0.244	0.468	1.056

The nebulizer output was connected to the Omega AHP-7561 heater, which was connected to a Variac to control its input voltage. The heater acted to evaporate the water droplets and separate them from the particles. Figure 3-6 shows the nebulizer and heater. A string was tied to the heater and the nebulizer container to keep the container vertical. A quick disconnect pipe fitting was added after the 90° bend for ease of construction and cleaning. Galvanized steel was chosen for the 90° elbow to isolate the hot heater from the quick disconnect connector, given the 52 W/(mK) conductivity compared to copper's 400 W/(mK) conductivity.

The operating voltage for the heater was determined using the PIV system in live mode and running the nebulizers with distilled water. Voltage was increased until no

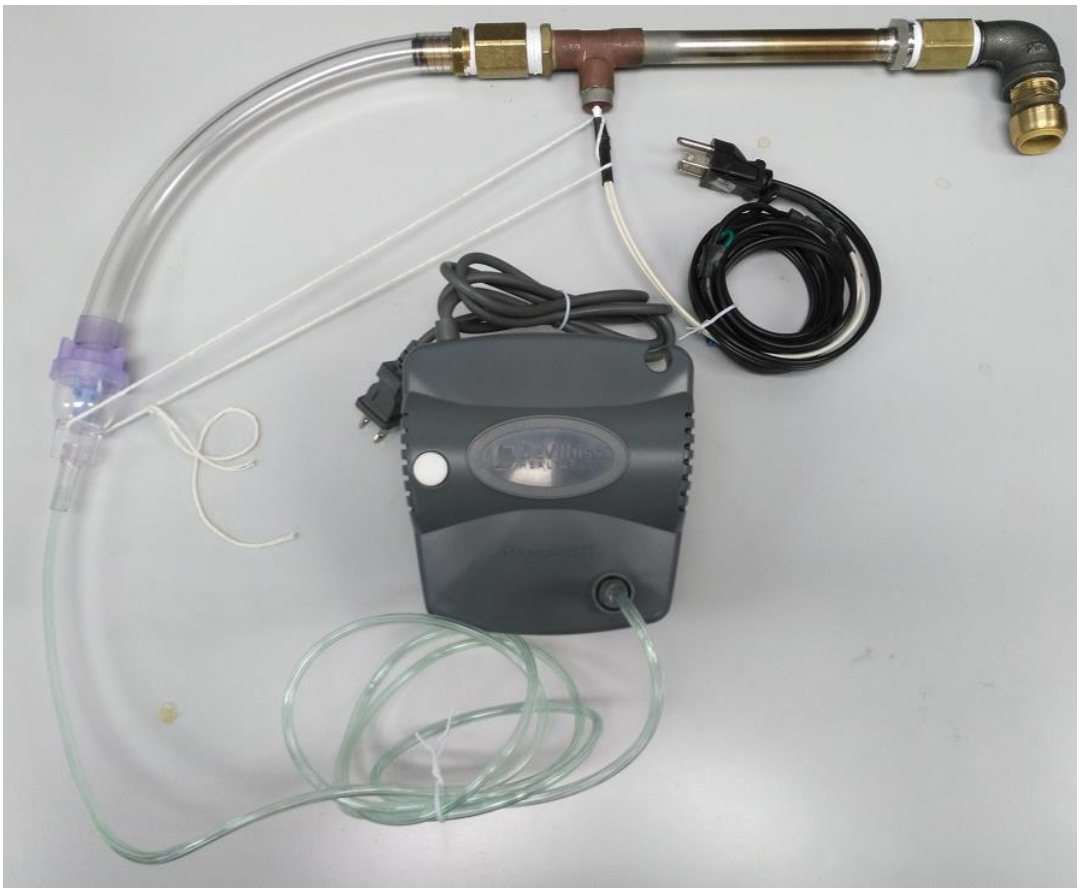

Figure 3-6. Nebulizer and heater.

noticeable water droplets could be seen and it was determined that this occurred at 25 Volts. At the heater exit, the temperature measured 150°C. At this temperature, all the water in the air has evaporated and became steam, which ensures that the particles are dry. The melting point of polystyrene is 230°C so the particles retained their solid form.

3.2.2 Humidity and Cooler

Humidity control is important in ensuring that only dry particles enter the chamber. In a previous experiment, Masati et al. presented results with large error bars[105]. It was determined that humidity was the cause of these errors. The water vapor entering the chamber from the nebulizer-heater system condensed into small droplets of unknown size, which interfered with measurements.

The laboratory, where the experiments were held, was kept at 70°F and 50% humidity. From Psychrometric charts, that amounts to about 8 grams of water per kilogram of air. The chamber is only 2 ft^3, which can only hold 1.1 grams of air. Only half a gram of water is necessary to reach 100% humidity.

To dehumidify the incoming air, a cooler was added to the setup. Figure 3-7 shows a 3D CAD representation of the nebulizer (a), heater (b), and cooler (c). The cooler was built with a copper pipe placed inside a bigger PVC pipe. The PVC

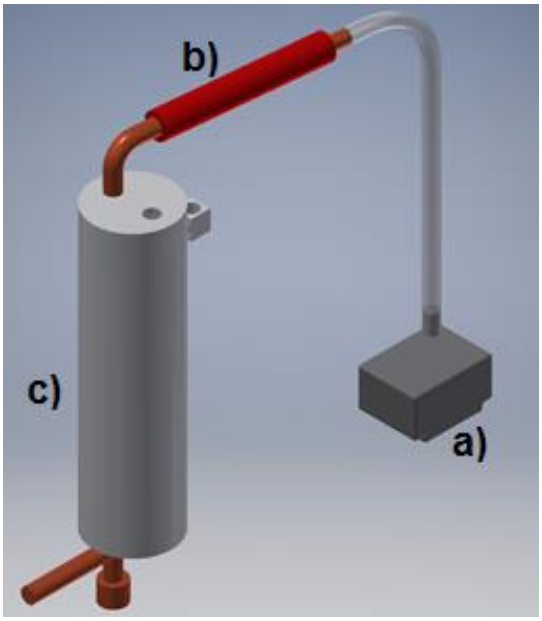

Figure 3-7. Seeding apparatus, a) nebulizer, b) heater, and c) cooler.

pipe was fed ice chilled water to cool the copper pipe. Approximately one foot of the copper pipe was in direct contact with ice water. A drain was added one foot above the bottom of the PVC container. The drain connected back to the ice water container with the water pump.

The cooler acts to condense the water droplets inside the copper pipe. A T-junction was placed at the bottom of the cooler to collect the condensed water but allow the dry polystyrene particles to continue to the chamber. The temperature at the end of the cooler, entering the chamber, was measured to be 18°C. At this temperature most of the water has condensed and the absolute humidity entering the chamber was less than that already in the chamber. Research by Benard et al.[30] shows that plasma actuator performance varies with relative humidity but that variance is smallest for the range between 40% and 55% relative humidity. Nagato et al. analyzed the mobility of ions in a negative corona operated in air[106]. They found that humidity plays an important role in ion formation. Water molecules increase the mass of the ion and alter mobility, an important factor in particle charging. However, such considerations are beyond the scope of this research.

Figure 3-8 shows the seeding apparatus attached to the chamber and the PIV setup. It was determined that one nebulizer-heater-cooler system did not properly seed the flow for PIV so a total of four systems were used in conjunction to increase seeding density. The figure only shows one seeding apparatus for clarity, but the system used four nebulizers, four heaters, and two PVC containers. The laser sheet was aligned with the center of the chamber so the seeding inlet holes were drilled away from the center. Polystyrene nanoparticles are safe to handle but are carcinogenic if inhaled. A 3 inch hole

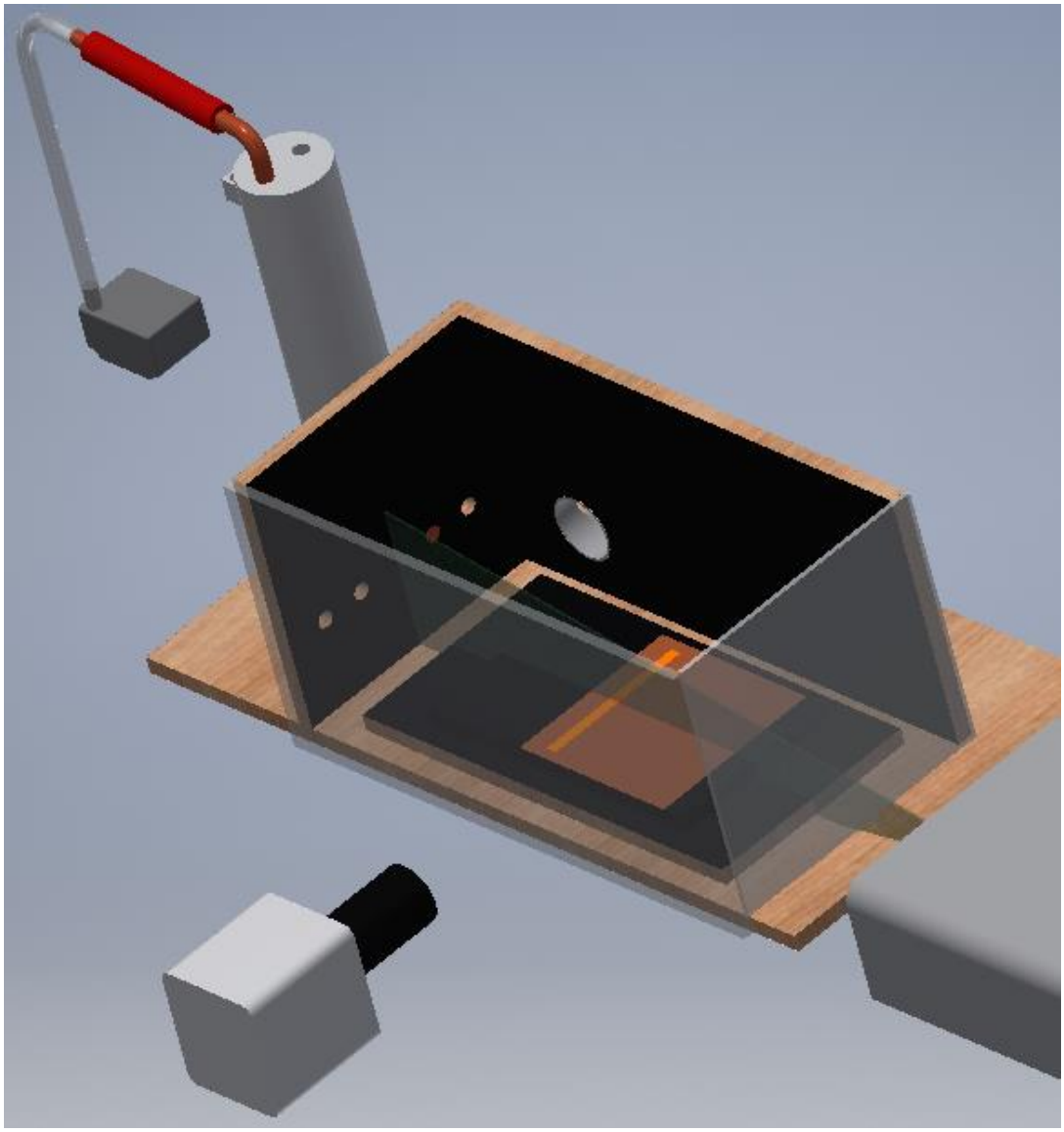

Figure 3-8. Chamber, PIV system, and one seeding apparatus.

was drilled on the far side panel and connected to a wet/dry vacuum with a HEPA filter capable of filtering 300 nm particles.

3.3 High Speed Data Acquisition

LaVision DaVis was the primary software used for image acquisition and analysis. Firmware update 2.0 for the high-speed controller and software update 8.2 allows LaVision DaVis to phase lock high-speed cameras usually meant for transient

flow. The update requires a steady input frequency that does not deviate by more than 1%. Instead of capturing each phase individually and saving after each capture, a circuit was designed to use the system speed to capture all images for all phases in one run. The total time remains the same but the data gathering portion only lasts a few seconds.

3.3.1 Circuit

The sinusoidal signal from the signal generator was connected to an inverting Schmitt trigger set to go high at 180 degrees and low at 250 degrees. The square wave was steady and connected to a phase-locked loop voltage controlled oscillator. A 25-bit ring counter acted as the frequency divider and shift register that separated the phases. The output signal from the voltage controlled oscillator had a ripple of 2.5 μs, which translates to an error of plus or minus 0.9 degrees for each phase. Each phase from the ring counter connected to a 32-bit multiplexer (mux) constructed using two 16-bit mux and a 2-bit mux. The output connected to the increment cable of the high-speed controller which acted as the camera trigger. A counter IC counted the number of image captures, which is an output of the camera. A second counter IC counted the number of times the first counter IC reached 256 images and signaled the multiplexer and the first counter IC to change to the next phase. This allowed the camera to continue capturing images for all the phases without stopping between them. Figure 3-9 shows the block diagram of the timing circuit. A GW Instek GDS 2204 oscilloscope was used to monitor the signal generator, the signal to the camera, the high voltage.

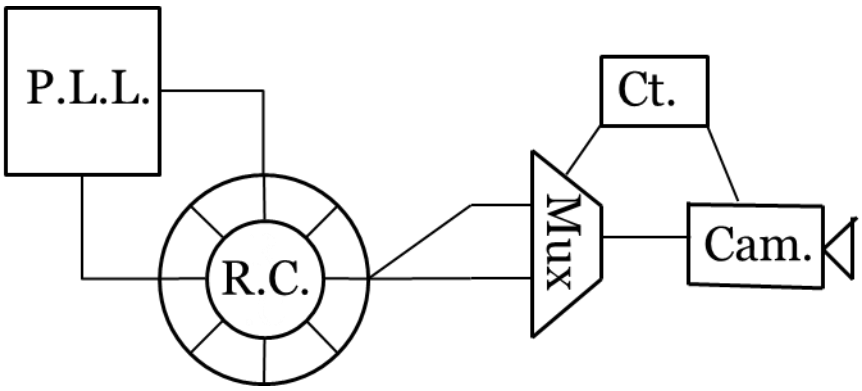

Figure 3-9. Timing circuit block diagram. P.L.L. is phase lock loop, R.C. is ring counter, Mux is the multiplexer, Cam., is camera and Ct., is the image counter.

3.3.2 Timing and Hardware

It should be noted that this method of image capture may damage certain lasers, especially older Nd:YLF lasers. The laser used for this experiment is capable of continuously varying its firing frequency; however, older laser systems could be damaged from continuously changing the frequency after several image captures. This change in frequency occurs during the change in phase when the laser needs to wait longer before it fires.

The camera also waited an extra 20 μs to capture the first image of a new phase. As such, that image is overexposed and not used in the analysis, but fortuitously, it simplifies the separation of images into phases by providing a distinct transition point. An artifact of the change in frequency appeared in the middle of the images. Two rows of pixels at the center of the camera had different exposures. This is due to the change in frequency during the transition from one phase to the next. The 20 μs time delay is 4% of the period and the camera is not calibrated for that frequency. Fortunately, the plasma actuator is located at the bottom of the image and the interesting flow region is far from the center of the camera. The center rows do not concern the flow interrogation.

In addition, the laser and camera capture a random number of blank images during warm up that are not saved in memory, but affect the counting for the timing circuit. The number of images to capture was buffered with extra images to account for the missing images. When all the necessary images were captured, the circuit was reset to finish capturing the extra images tacked on the end and save the entire set. The circuit should be augmented to change phases in a manner that does not cause artifacts before it is used with other systems.

3.4 Procedure

Before and after each experiment, the chamber, the plasma actuator, and the seeding apparatus were cleaned with acetone to avoid any mixing between particles. The proper amount of water and micro particles was placed into each container and thoroughly mixed. Seeding of the chamber began but to remove the initial water droplets that had not been evaporated, the wet-dry vacuum also started evacuating the chamber. After a couple of minutes, the heater reached a stable temperature and the vacuum was turned off. Seeding of the chamber continued until a proper seeding density was observed. Throughout all of this, the plasma actuator was operated to mix the air inside the chamber. The PIV experiment was conducted using the timing circuit to help with data acquisition. The plasma actuator and seeding apparatus were turned off. The chamber was evacuated with the vacuum and the assembly was cleaned with acetone to prepare for the next experiment. Distilled water was run through the seeding assembly to clean out any stray particles. Pipe cleaners and Kimwipes ® were used to clean the pipes in the cooler. The use of quick disconnect fittings simplified the process.

Chapter 4: Processing and Results

Cross-correlation is the mathematical basis of PIV. The discrete function is shown in Equation (4-1)

$$f(k) \otimes g(k) \equiv \sum_{l=-\infty}^{\infty} f^*(k)g(k+l) \tag{4-1}$$

Where $\otimes$ represents cross correlation, k is the function variable, and l is the dummy variable. The * modifying f inside the sum represents the complex conjugate operation. The continuous cross-correlation function replaces the sum with an integral. Simply stated, cross-correlation gives the similarity between two functions.

Pattern recognition relies on cross correlation, and a modern-day example would be facial recognition. Given a passport photo, cross-correlation can be used to find that person in another photo of themselves with a group of friends. In PIV, cross-correlation is used to find the displacement of a group of particles between two frames. Frames can be separated into windows to focus on groups of particles and calculate velocities in specific regions of the image. Window sizes can vary but in the present many studies attempt to get data using window sizes of 32 x 32 pixels or less to improve their vector resolution. As stated in the literature review, the usual rules for PIV cross-correlation are that there exists 10 particle pairs within one window, the particle displacement is around a quarter of the window size, and that loss of particles through uneven motions is small.

The plasma actuator in this experiment operated with a period of 500 μs. A 20 μs time difference between the images led to separating the cycle into 25 phases. The timing circuit was configured to capture 256 double images for each phase of each particle size.

The first 6 out of the 256 images for each phase were discarded because of light intensity issues from the change in the phase. The 20 μs Δt and image magnification lead to a maximum pixel displacement of 8 to 9 pixels for the fastest part of the flow, which would work well for an initial processing grid of 32 x 32 pixels; however, the seeding density was too low for such a small interrogation window.

4.1 Processing

The LaVision DaVis processing software was used to conduct the cross correlation analysis. An initial grid of 64 x 64 pixels with standard PIV techniques produced bad quality vectors. Even with four seeding apparatuses, the seeding density was not high enough for standard PIV techniques; grid sizes of 128 x 128 pixels would be needed to initiate processing at the expense of resolution. Sum-of-Correlation PIV was used to increase vector density and quality at the expense of automated error analysis and individual image pair data.

Sum-of-Correlation processing is used to find the average velocity field for flows with low seeding. For good PIV results, 10 particle pairs between frames is suggested. When looking at small regions of flow, seeding density decreases and individual cross-correlation results can be noisy and incorrect. Sum-of-Correlation relies on the flow being steady enough that the correlation peaks between accurate cross-correlation results are within each other's uncertainty. By summing all the correlation planes, the average particle displacement becomes more apparent.

Sum-of-Correlation processing was conducted for each phase and each particle. The initial window size was set to 64x64 with 50% overlap and then reduced to 32x32

with 50% overlap. Three passes were conducted for each window size to ensure convergence. Average intensity subtraction pre-processing was used to increase peak to noise ratio. Post processing consisted only of an allowable velocity vector range, which ranged from -2 m/s to 7 m/s for the x-direction and -2 m/s to 2 m/s for the y-direction (normal to the surface).

The laser sheet was aligned parallel to the plasma actuator's dielectric sheet; however, some light still reflected off the dielectric. More light was reflected from the electrode and the area near the electrode is brighter than other areas. Figure 4-1 shows the region of interest for interrogation, a rectangle that masks out some of the reflection from the dielectric. With the 32x32 window and a 50% overlap vector, the vector density exceeded 6 vectors per millimeter with 12 vertical vectors and 98 horizontal vectors in the region of interest.

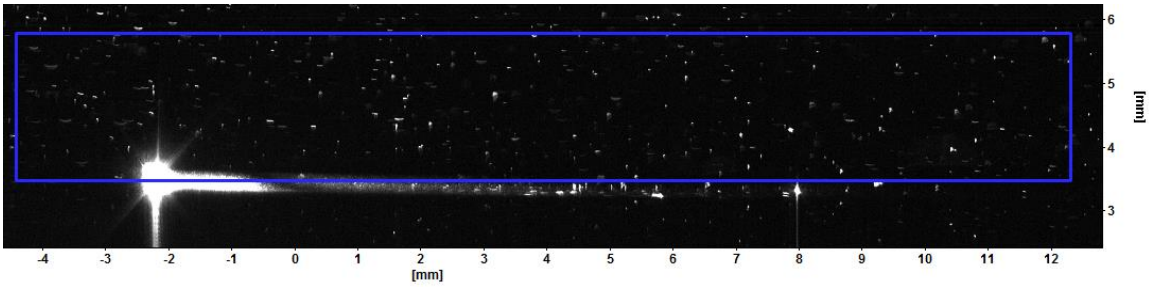

Figure 4-1. Camera image showing the region of interest, the geometric mask and the electrode reflection.

4.2 Vector Alignment

Velocity vectors need to be compared at the same location and same phase in order to glean accurate information. Cleaning the chamber and the seeding apparatus after every particle moved the plasma actuator. The camera pixels are only 10 μm and it was noticed that after cleaning, the plasma actuator had moved in the image plane by a

few pixels. The interrogation grid and the vector positions are always in the same location in the image plane.

To properly compare vectors, the center of the plasma actuator was set as the zero position for each phase. Since the plasma actuator moved after cleaning, a global zero position was needed to subtract out the translation of the actuator. The phase at 48^{o} in the 300 nm particle set was chosen as the global zero position.

Figure 4-2 shows the reflection from the copper electrode and the calculated centroid. The reflection image was converted to a binary image by setting all intensities values greater than 2000 to 1, and all lower values to 0. The binary image isolated the reflection of the electrode. The plasma actuator reflection from the copper electrode served as the zero point and the center was determined using a centroid finding algorithm. Cross correlation analysis of the plasma actuator reflection between each phase and each particle run was conducted to determine the displacement of the actuator. Within a particle set, the plasma actuator was found to translate within +/- 1 pixel. This is believed to be caused by heating effects from the plasma. The translation of the plasma actuator was found to be on the order of 10 pixels or about 0.1 mm between particle sets. This is not a large movement and within the alignment precision of the chamber. As such, re-alignment between the plasma actuator and the laser was not performed after cleaning.

Figure 4-2. Reflection from the top electrode and associated centroid location.

With the plasma actuator and vector locations properly zeroed, the next step was to create a global grid for vector comparisons. The grid points were chosen such that they

were within the data sets for each particle size. A bilinear interpolation was used to calculate vectors for each phase and particle set at the same physical location from the plasma actuator and allow for a proper comparison between them.

4.3 Velocity Measurements

Ensemble processing combined the 250 double images for each phase into one vector field producing 25 vector fields for 5 particle sets or a total of 125 velocity vector fields. Each vector field contains 10 vectors in the vertical direction and 96 vectors in the horizontal direction, parallel to the plasma actuator.

Figure 4-3 shows the velocity field for some of the phases and particles. Two phases, 62° and 235°, show that during the positive voltage cycle of the actuator the velocity profile is thinner and closer to the surface, while during the negative half cycle the velocity profile is thicker, in line with previous experimental results.

Also included in the figure are velocity profiles for the 300 nm and 1250 nm particles at 235° to show the qualitative similarity between the particles. The choice of particle size in this range does not alter the flow shape of the plasma actuator, which implies that the particles are not qualitatively affecting the plasma actuator operation. Differences between particle sizes can be seen in the color shading but for more quantitative analysis, a point comparison is best.

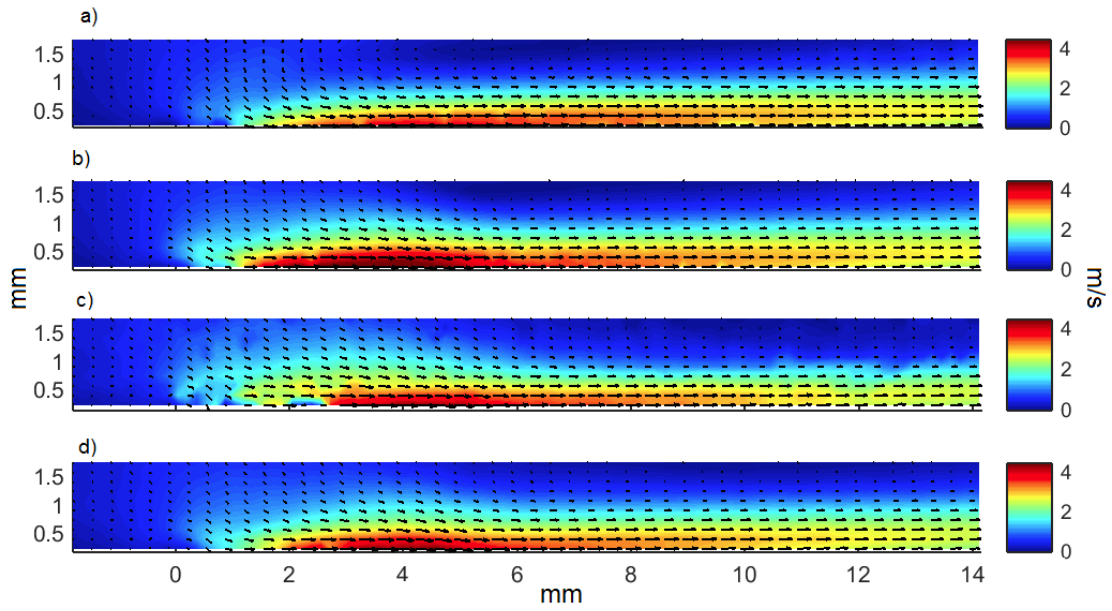

Figure 4-3. Velocity fields results from PIV analysis: a) 700 nm particles at 62° phase, b) 700 nm particles at 235° phase, c) 300 nm particles at 235° phase, d) 1250 nm particles at 235° phase.

The position 5.24 mm downstream of the top electrode and 0.42 mm above the dielectric was chosen to analyze the velocities of the particles. The point is at an interesting location where the flow velocity peaks and changes magnitude and direction throughout the cycle. The peak velocity changes location with phase and 5.24 mm is the average downstream distance for the peak velocity location.

Figure 4-4 shows the x-velocity component at that point for the 300, 700, and 1250 nm particles for all phases. The 500 and 900 nm particles were excluded for clarity. Smaller particles are faster than larger particles. This is more prevalent when the actuator is on the positive voltage half cycle between 0 and 180 degrees.

The velocity of each particle shows a large acceleration at about 180 degrees when the voltage becomes negative. A PUSH-push type of actuation is observed as the particles have 2 peaks in velocity. Velocities peak for particles at around 60° and again at

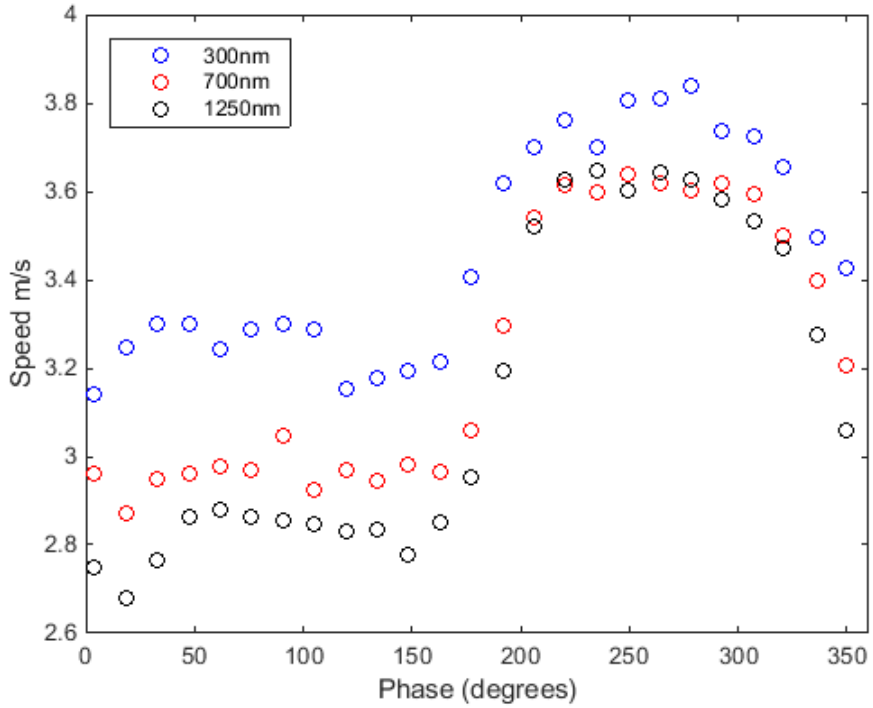

Figure 4-4. Particle velocity for all phases in the x direction at (5.24, 0.42) mm. The 300 nm particles in blue are the fastest, followed by the 700 nm particles in red, and the 1250 nm particles, in black, are the slowest.

around 250°, though the latter peak is larger. The 1250 nm particles are accelerated to 3.6 m/s at their major peak and less than 2.9 m/s at their minor peak.

Velocity varies more for smaller particles rather than larger particles. From 220° to 292° the velocities of the particles are mostly constant, but the 300 nm particles vary more with a 0.05 m/s standard deviation compared to the 0.02 m/s of the 1250 nm particles. A larger variance is present during the plateau between 50° and 148°. Smaller particles have faster velocities with larger variances.

Velocity differences between the 300 and 1250 nm particles are larger when the voltage is positive. During the later phases, velocity differences reduce and the 1250 nm particles travel faster than the 700 nm particles for a few phases. Focusing on the 62°

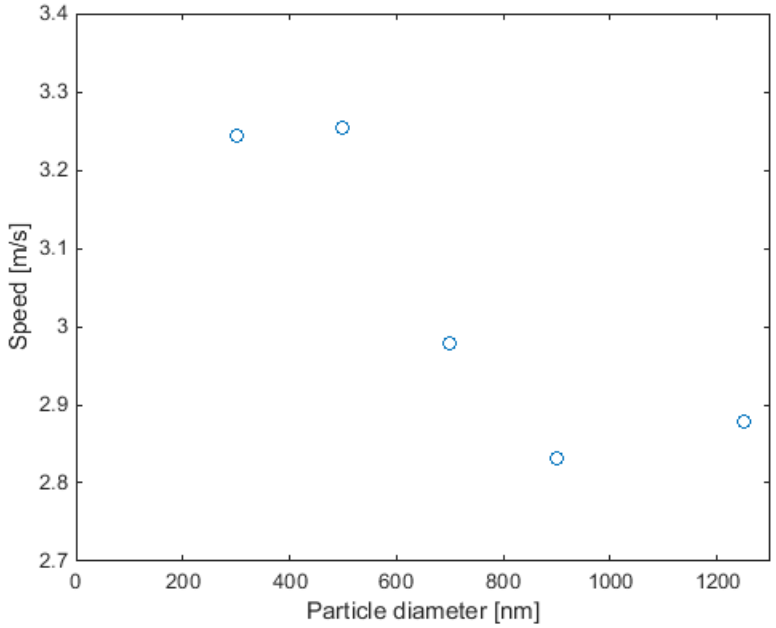

Figure 4-5. Particle velocity in the x-direction at (5.24, 0.42) mm and 62° phase.

phase, Figure 4-5 shows the x-velocity for all particles. The difference in speed between particles is more apparent in this figure.

The 300 nm and 500 nm particles are about 0.4 m/s faster than the 900 nm and 1250 nm particles. In this case, the 500 nm particles are faster than the 300 nm particles. Also, the 1250 nm particles are faster than the 900 nm particles with the 700 nm particles in the middle. Uncertainty analysis will be covered in the next chapter, which will explain the difference in velocity between neighboring particles.

For the y-component of the velocity, significant differences are difficult to discern. Figure 4-6 shows the y-component of the velocity for all phases. Particle velocities remain negative most of the time with a sharp rise near the transition from negative to positive voltages with a sawtooth structure as shown in the figure.

Unfortunately, the differences between particles are small and difficult to categorize. The 300 nm particles tend to have a more negative bias in the data and again are more sporadic than the larger particles. Velocity differences between the 300 nm and the 1250 nm particles are around 0.1 m/s and the 700 nm particle speeds are not always in the middle. Velocity components in the y-direction do not have a clear trend like the x-component velocities at this location.

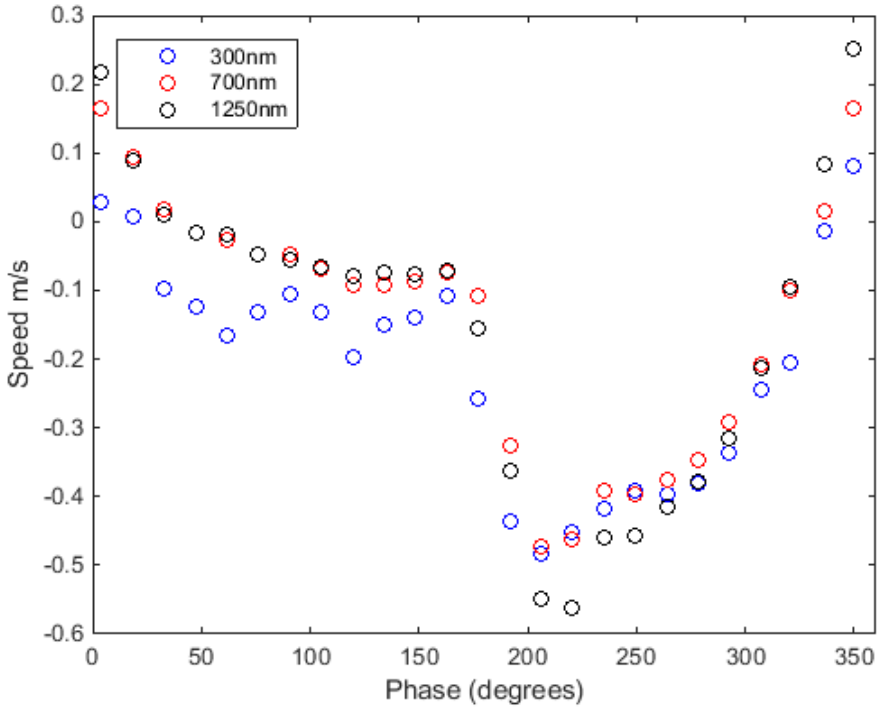

Figure 4-6. The y-direction velocity component for all phases at (5.24, 0.42) mm. A sawtooth structure exists for all particles but differences between particles are small.

4.4 Particle Acceleration

Particle acceleration provides important information for the dynamics of plasma actuators. Accelerations were calculated with time and convective derivatives of the velocity fields as shown in Equation (4-2)

$$a = \frac{dv}{dt} = \frac{\partial v}{\partial t} + (v \cdot \nabla)v \tag{4-2}$$

The time derivate of the velocity was calculated using a central differencing scheme for each phase. The convective derivate of the velocity was calculated also using a central differencing method, which reduced the number of data points by 2 in both the x and y-direction. Acceleration fields are made up of 10 vertical vectors and 96 horizontal vectors for a total of 960 vectors, which cover the rectangular region between the corner points (-1.63, 0.42) mm and (13.95, 1.59) mm.

Figure 4-7 shows the acceleration fields for four phases, 4°, 91°, 192°, and 278° from top to bottom for the 500 nm particles. Strong acceleration regions are present near the electrode and depending on the phase, the direction can be upstream or downstream. Stronger magnitudes are on the order of $1x10^4$ m/s^2 and present during the transition to negative voltages at 192°. Weaker acceleration magnitudes, on the order of $3x10^3$ m/s^2, are present for positive voltages, quantifying the PUSH-push actuation. Following the

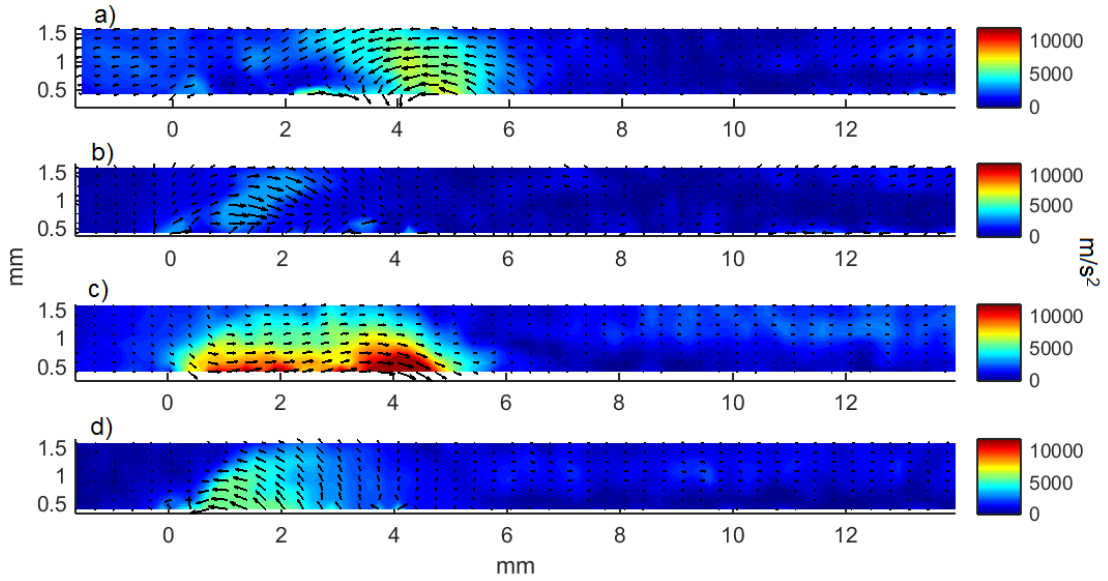

Figure 4-7. Acceleration field for 500 nm particles at a) 4°, b) 91°, c) 192°, and d) 278° phase.

strong acceleration at 192°, the flow begins to decelerate at 278° starting near the electrode and persisting through 4°. Flow acceleration begins again after that but as seen at 91°, the strength is much smaller in comparison to 192°.

In order to avoid a division by zero, the absolute value of the time and convective derivatives were summed to give the positive acceleration value, which was used as a normalizing variable for the time derivate. Equation (4-3) and (4-4) show the absolute value summed acceleration and the normalized ratio of the timed derivate. Where a_{abs} is the normalization variable and $a_{t/abs}$ is the acceleration ratio, which is plotted in Figure 4-8 for 4°, 91°, 192°, 278°. Stronger time derivative values are represented by lighter regions, while stronger convective derivative values are represented by darker regions.

$$a_{abs} = \left|\frac{\partial v}{\partial t}\right| + |(v \cdot \nabla)v| \tag{4-3}$$

$$a_{t/abs} = \frac{\frac{\partial v}{\partial t}}{a_{abs}} \tag{4-4}$$

Near the top electrode, the convective derivative has larger values at 4° and 91°. The time derivative is stronger for the later phases at 192° and 278°.

Focusing on the region between 0 and 6 mm, the time derivative has a larger effect overall as darker regions tend to be confined to smaller areas near the 2 mm mark. For the region downstream of 6 mm, the ratio values fluctuate with apparent randomness, which is the noise caused by taking a derivative of discrete data.

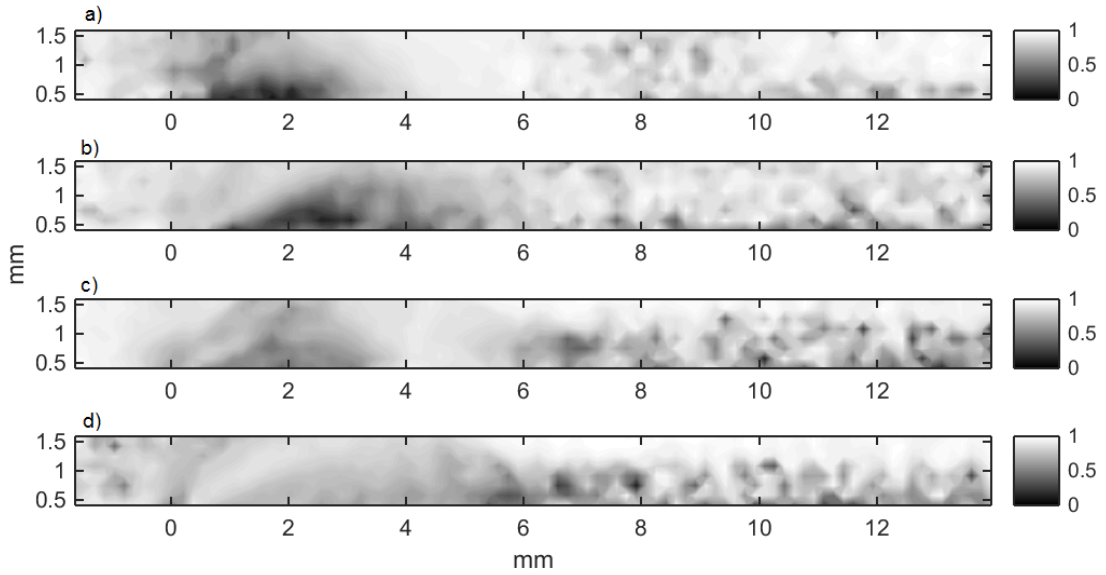

Figure 4-8. Acceleration ratio for the 700 nm particles at a) 4°, b) 91°, c) 192°, and d) 278° phase

Figure 4-9 shows the acceleration in the x-direction for time and convective derivatives and the total derivative for all phases for the 700 nm particles at (2.22, 0.42) mm (left) and (5.24, 0.42) mm (right). The acceleration at 2.22 mm peaks at 148° and 25,000 m/s^2. The acceleration at 5.24 mm peaks at 206° and 6,000 m/s^2. The PUSH notation refers to these large accelerations. A large pull can be seen for both points. At 307°, flow decelerates at with a negative value of 15,000 m/s^2 at 2.22 mm, and at 4° the deceleration at 5.24 mm reaches a negative value of 6,500 m/s^2. The time derivative fluctuation drives the change in acceleration, while the convective derivative remains mostly constant for both points. It is for this reason that better temporal resolution would serve plasma actuator analysis more than better spatial resolution.

A small push can be seen in the time derivative at 48° and 5.24 mm. For the 2.22 mm point, the small push is driven by the convective derivative instead. Both the large acceleration and the large deceleration start upstream at 2.2 mm and travel downstream. These accelerations are driven by the time component. The forces originate near the

electrode and travel downstream while dissipating. Each phase is 20 μs apart, so the propagation speed of these forces is approximately *3.02/(4*20) = 0.038* mm/μs or 38 m/s. The large acceleration dissipates faster than the deceleration. The positive

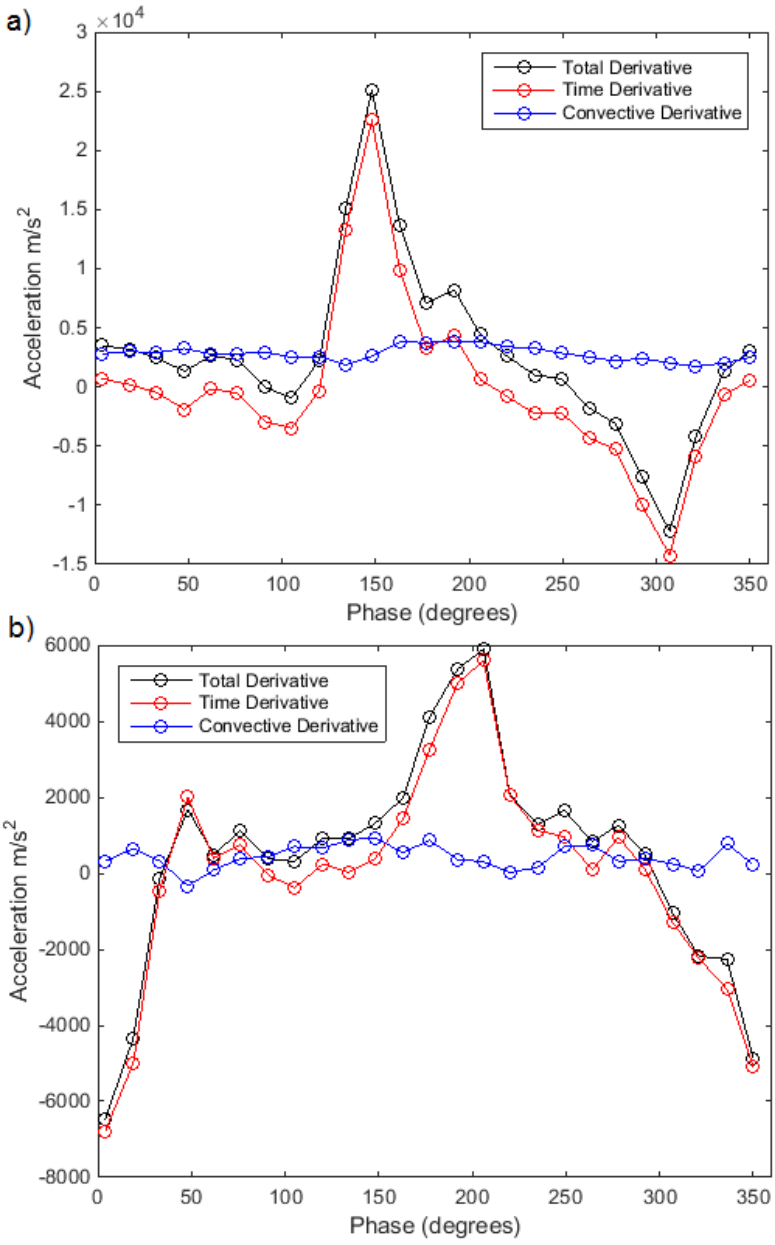

Figure 4-9. Acceleration components for the 700 nm particles for all phases and two locations: a) (2.22, 0.42) mm, b) (5.24, 0.42) mm.

acceleration has decreased to just 24% of its maximum magnitude at 5.24 mm, while the negative acceleration decreased to 45% of its maximum. By the time the forces have propagated to 5.24 mm, deceleration has overtaken acceleration in magnitude and only the small push starting at 48° raises the average acceleration to 430 m/s^2 compared to the average 2800 m/s^2 at 2.22 mm. As seen in Figure 4-7, plasma actuators accelerate the flow near the top electrode but the forces dissipate further downstream. The effective flow acceleration region has a downstream length of 6 mm, at most.

4.5 Comparison with literature

PIV has been used extensively to study plasma actuators and many of those studies were discussed in Chapter 2. Kotsonis and Ghaemi[26] produced PIV results with high spatial and temporal resolution for a plasma actuator operating at 625 Hz and 10 kV_{pp} and their work will be used for comparison. They produced both velocity and acceleration data for 48 phases, but were limited by the camera to a distance of less than 8 mm downstream of the top electrode. They seeded the flow with atomized olive oil, which has an average diameter of about 1 μm and enabled the use of standard PIV processing algorithms.

Results showed velocity fields with speeds approaching a maximum of 4 m/s and a PUSH-push type of actuation. In general, the velocity fields were similar in structure and behavior to the ones presented here. For the x-direction, two velocity peaks were present, but the velocity during the positive half cycle had a much smaller peak and flatter plateau than the data presented here. The difference is attributed to the operating frequency and voltage differences between the two experiments. For the y-direction, the velocity

remains mostly negative with a positive peak near 0° in a sawtooth shape, much like the data presented here.

There were similarities for the acceleration results as well. Their results showed a large push forward when the voltage became negative with a 12,000 m/s^2 maximum magnitude. There is agreement for the flow deceleration that occupies a large portion of the cycle and the small acceleration experienced after that, but their magnitude for the weak acceleration is on the order of 1000 m/s^2, while the results presented here are closer to 3000 m/s^2. Again, the factor of three difference is attributed to the different operating conditions of the plasma actuator, such as higher voltage and higher frequency.

Murphy et al. researched the scaling of velocity and force through an empirical fit based on PIV measurements[107]. They found similar trends to what was mentioned in Chapter 2 for scaling of speed and force. They conducted phase locked PIV experiments for 8 phases spaced 45° apart. The quiescent experiment chamber was seeded with DEHS particles and the plasma actuator operated at 4 kHz and two voltages, 7 kV_{pp} and 14 kV_{pp}. Results agreed with the findings of the community; airspeed is faster during negative voltages and velocity and forces increased with voltage. Interestingly, higher voltages also led to a stronger push during the positive half cycle, which explains the stronger acceleration in the present data when compared to Kotsonis and Ghaemi.

In conclusion, the results presented here agree with the community for both velocity and acceleration. This work provides values for multiple monodisperse particle experiments and has shown that there exists a difference between particle sizes. To properly compare particle velocities, the uncertainty of the measurements must be quantified.

Chapter 5: Uncertainty Analysis

In recent years, PIV uncertainty analysis has gained attention and brought about new methods of analysis, which are covered in Ref. 73-76. A test was conducted in Refs. 77 and 78 to measure the performance of the new methods. LaVision DaVis uses the method described in Ref. 76 to calculate the uncertainty given a set of PIV images.

Unfortunately, these methods cannot be used with Sum-of-Correlation techniques. A qualitative uncertainty determination method was proposed by Kähler and Scholz[71], who, using Gaussian approximation, took into account turbulence, noise, particle size, and velocity gradients. Scharnowski et al.[79] quantitatively determined the effect of particle size and velocity gradients on single pixel ensemble PIV uncertainty.

They argue that the Reynolds stresses – the fluctuation of the velocity – can be calculated if the probability density function (PDF) of the flow is known. They assumed that the correlation plane peak, *C,* can be approximated as the result of the cross correlation of image *A* and image *B*, which was convolved with the PDF as shown in Equation (5-1), where $\otimes$ represents the cross-correlation operator and $\circledast$ represents the convolution operator defined in Equation (5-2)

$$C \approx A \otimes (B \circledast PDF) \tag{5-1}$$

$$f(x) \circledast g(x) \equiv \int_{-\infty}^{\infty} f(s) g(x-s) ds \tag{5-2}$$

Convolution is simply the integral transformation of a function by another function. Essentially, a function, *f*, is weighted by another function, *g*, to give the result. For Equation (5-1), Scharnowski et al. assumed that the PDF acted only on the second image and that all effects, such as noise, turbulence, and velocity gradients were captured

by the PDF. By assuming that the PDF is Gaussian, they related the correlation peak with the PDF. At first, they considered only the particle image diameter and then added the effect of velocity gradients. Plasma actuators have weak velocity gradients for most of their velocity field. As such, only particle image diameter effects are taken into account.

The correlation peak was shown to be the convolution of the particle image diameter and the PDF. For perfect Gaussians, the relation for the standard deviation reduces to a geometric sum shown in Equation (5-3), where *D* is the particle image diameter and σ represents the standard deviation in either the x or y-direction

$$C_\sigma = \sqrt{PDF_\sigma^2 + 2D^2} \tag{5-3}$$

The standard deviation of the correlation peak can be calculated from experimental data. The particle image diameter is determined through autocorrelation. The standard deviation of the PDF can be calculated from the deconvolution of the image particle diameter from the correlation peak. In this work, instead of the simplified geometric difference, deconvolution between the correlation peak and the particle image diameter was used. The Gaussian assumption is great for theoretical works, but whenever possible the experimental data were used instead.

Reynolds stress is a measure of the flow fluctuation, or, in other words, the variance in the flow velocity. Scharnowski et al. then derive the Reynolds stress for the x-direction based on the PDF as shown in Equation (5-4)

$$\langle u'^2_x \rangle = 1/16(PDF^2_{\sigma x} cos^2\alpha + PDF^2_{\sigma y} sin^2\alpha) \tag{5-4}$$

Where, u'^2_x is the velocity fluctuation in the x-direction, α is the rotation angle of the PDF, and σx represents the standard deviation in the x-direction. The y-direction equation

has the sine and cosine terms switched. The rotation angle of the PDF, α, was discovered to be less than 4° so the relation was further simplified.

In summary, the correlation peak contains the sum of all effects of the particle flow. The uncertainty is calculated by deconvolving the particle image diameter from the correlation peak to determine the PDF. The velocity fluctuation is then computed from the standard deviation of the PDF. Effects such as noise and turbulence were not taken into account even though they contribute to the correlation peak width. Velocity gradient effects are small for plasma actuators and are ignored.

5.1 Particle Image Diameter Estimation

The correlation peaks given by the Sum-of-Correlation technique are the amalgamation of all the image pairs for that phase and image location. The amalgamation of the particle image diameters needs to be calculated first in order to deconvolve the particle image diameters. Autocorrelation was used on each window and image, along with a 3 point Gaussian fit, to calculate the particle image diameter. The average diameter was calculated for each window.

However, due to the low particle density, some windows did not contain any particles. These empty windows were, instead, a collection of noise. An empty window autocorrelates to the Dirac Delta function and significantly decreases the average particle diameter measurement, which artificially increases the uncertainty measurement. Figure 5-1 shows the autocorrelation for an empty window (top) and an adjacent populated window (bottom). Empty windows autocorrelate to single peaks, while particles have significantly larger diameters. Empty windows do not contribute to the cross-correlation

peak but they do artificially decrease the autocorrelation peak. The decrease in diameter for the autocorrelation leads to an artificial increase in uncertainty measurements. To combat the effect of empty windows, any particle image diameter found to have a standard deviation of less than half a pixel, or one pixel for two standard deviations, was excluded from the average diameter calculation.

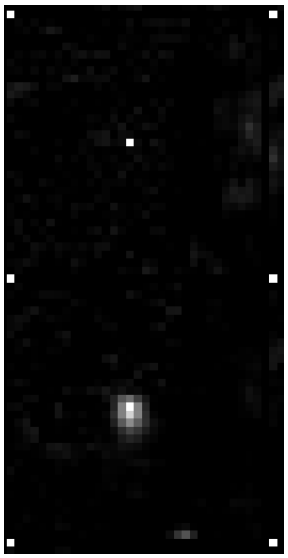

Figure 5-1. Autocorrelation of an empty window on top and an adjacent populated window on the bottom.

Figure 5-2 shows the calculated diameters from the 250 images for a window for the 500 nm set at a phase of 48°. The blue circles represent the diameter data. The red stars show the increase in the average image diameter after excluding the smaller diameter data. Diameters smaller than 1 pixel are grouped together and a clear division exists between the group and the larger diameter data. The figure also shows the average image diameter before and after excluding the empty windows as 2 red stars with a difference of about 0.4 pixels in both directions.

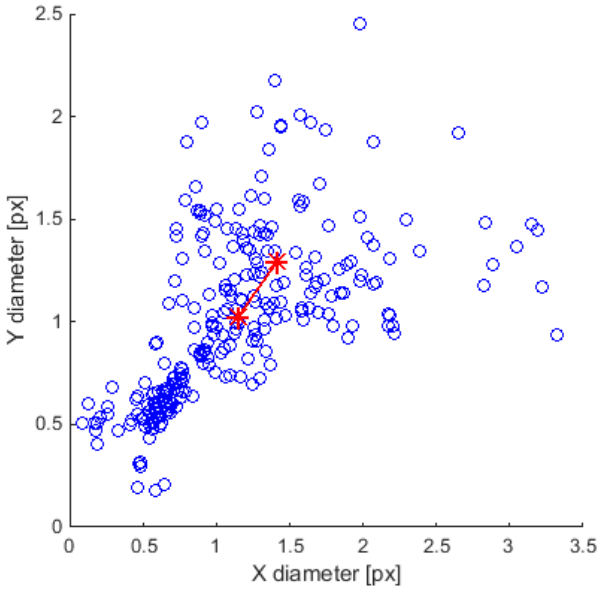

Figure 5-2. Particle image diameter for the 500 nm data of 250 windows.

5.2 Velocity Comparison with Uncertainty

The average image diameter was calculated from the addition of all populated autocorrelation windows. Deconvolution from the cross-correlation peaks, which were provided by the DaVis software, was conducted using the Weiner algorithm with zero noise level. After deconvolution, standard deviations in both x- and y-directions were calculated using a 3 point Gaussian fit for each window. The bilinear interpolation was conducted once again to calculate the uncertainties at the chosen vector locations. The results are shown in Figure 5-3 as error bars. For 95% bounds, the average uncertainty for all phases and particles was about 0.7 pixels, which corresponds to 0.4 m/s. The 300 nm particles lie outside of the 900 and 1250 nm error bars and have a difference of at least 0.4 m/s.

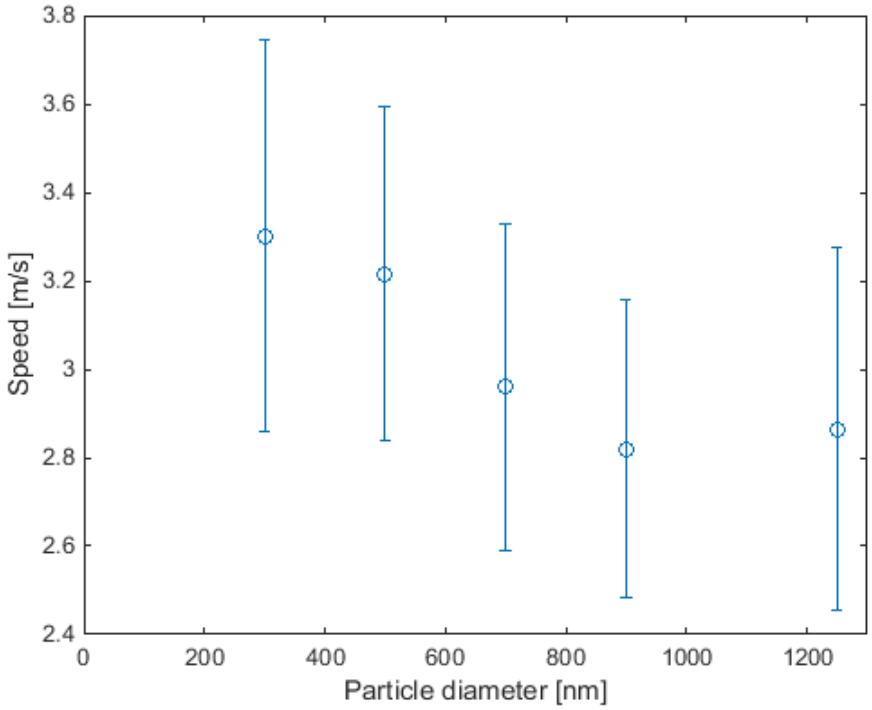

Figure 5-3. The speed of particles with error bars at 48° and point (5.24, 0.42) mm.

5.3 Multiple Particle Data Sets

It was desired to conduct the experiment multiple times for each particle; however, time limitations with the hardware allowed for gathering an extra dataset only for the 300 nm, 500 nm, and 700 nm, particles. Until now only the clean data has been presented, but Figure 5-4 presents the speed for both sets of particle data at point 5.24, 0.42 mm with corresponding uncertainty bounds. Differences within particle data sets can be large. Although the 500 nm particles don't show much of a difference at this location and phase, their differences are more severe in other points. Both 300 and 700 nm sets have an almost full error bar difference between their respective data sets.

Why such a large difference? Two conclusions can be reached. Either the plasma actuator behaves more erratically than can be measured by 250 images, or the particles are not the same size throughout the measurements. A statistical T-test can help resolve the question by answering whether or not the plasma actuator performance varies to the point where these data sets are dependent.

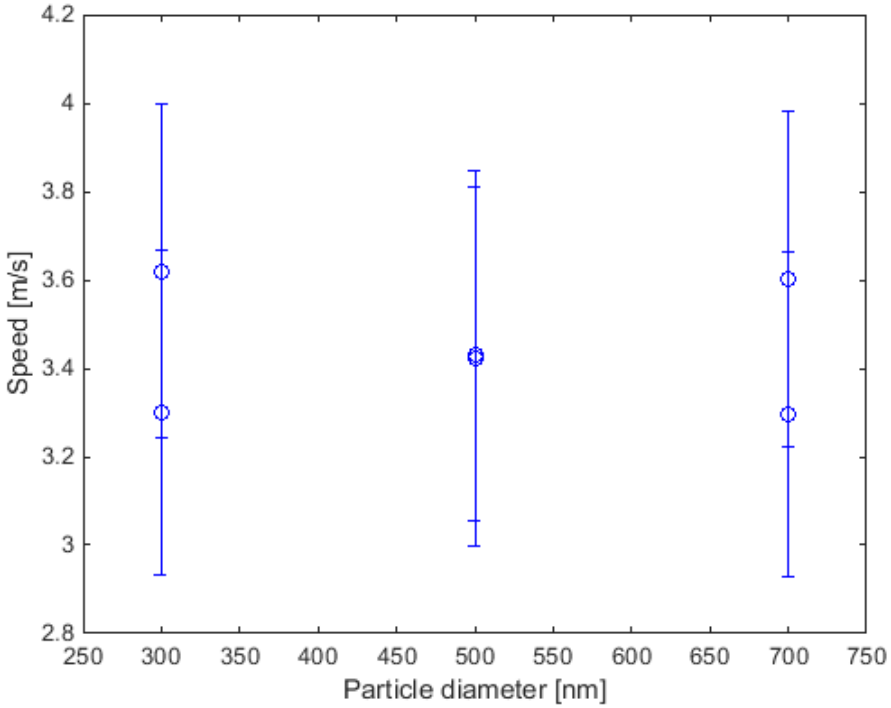

Figure 5-4. Intra-particle set velocity differences at (5.24, 0.42) mm.

5.3.1 Null Hypothesis

In testing differencing within particle data sets, the null hypothesis will first be considered. Are the different data results statistically independent? If so, the difference is not caused by limited sampling of the variability in plasma actuator performance but rather other factors, such as particles sticking together. The standard method for calculating independence is the T-test for two data sets. Three pieces of information are required for each data set, the mean, the standard deviation, and the number of samples. The mean and standard deviation have already been calculated as outlined above. The number of samples was calculated by summing the cross-correlation intensity values over 3 pixels in the x- and y-direction. The T-test was conducted in MatLab for the intra-particle-size data sets. Only the 5 phases with uncertainty data were included.

Figure 5-5 shows the result of the test for phase and particle size. The T-test results are shown on top and the velocity field on the bottom for the 700 nm 264° data set. White squares indicate statistically different speeds and pass the null hypothesis test. A significant portion of the velocity field was found to be different for the two data sets, which implies that there is a difference in the particle data not caused by the plasma actuator performance.

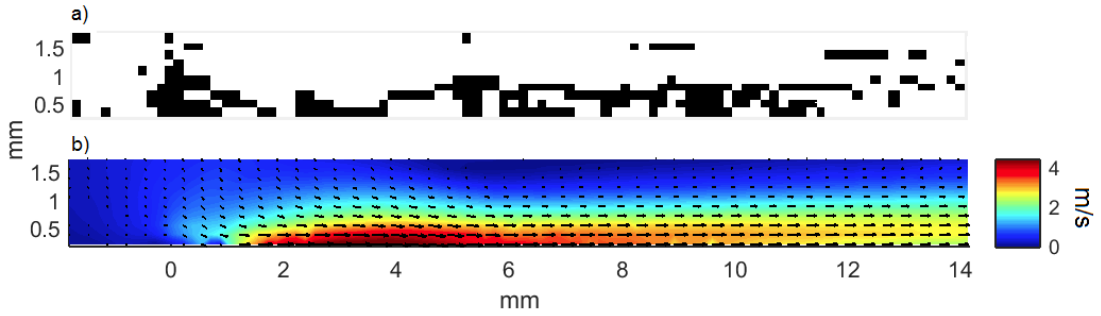

Figure 5-5. Null hypothesis test, a) T-test result, b) velocity field.

Plasma actuator variability is not the reason for the difference. Focusing on the particles, while they were diluted and mixed in a distilled water solution, there is no guarantee that any two particles didn't attach to one another forming a larger particle. Attached particles are larger but don't have a spherical shape. The differences in velocity would arise from a combination of electrostatic and aerodynamic forces. A larger surface area can hold more charge. At the same time, the Stokes drag force is larger but since the shape is not spherical, the value is not easily determined. The most accurate representation of the stated particle size, is the data set with the smallest particle diameter. The question becomes, "which data set best represents single spherical particles?"

5.3.2 Smallest Particle Diameter

Two particles adhered together have a larger scattering cross section than a single particle. While the light scattered off a particle will depend on the laser sheet and particle interaction, on average the data set with the smaller average particle image diameter contains fewer double particles and is more accurate. The calculations for the particle image diameter were already completed and outlined in the section above. Elliptical areas were calculated for each particle data set by multiplying the x- and y-direction standard deviations together. The comparison was conducted for the velocity field region between 2.2 mm and 8.1 mm in the x-direction and 0.42 mm and 0.93 mm in the y-direction. Comparing the entire velocity field showed little difference between particles because of boundary reflections and out of focus particles that linger in slow speed regions. As such, the comparison region was reduced to the fast speed portion of the flow field.

Results showed that the first data set for the 300 nm particles had a smaller area by 0.06 px^2. The second data sets for the 500 nm and 700 nm particles were found to have smaller areas by 0.12 px^2 and 0.05 px^2 respectively. The velocity fields with the smaller area particles, along with the 900 nm and 1250 nm velocity fields, comprise the data presented in this work.

5.4 Air Velocity field

Particle image velocimetry results show the velocity field of the particles, not necessarily the airflow. This work has demonstrated that particle size affects PIV results. Smaller particles are expected to trace the true airflow better because they charge less and are affected by the strong electric fields less than larger particles. In theory, a very small

particle would have little to no charge on it and perfectly follow the flow. In reality, PIV cannot image small particles, and diameters on the order of Angstroms are closer to molecules than tracer particles. Therefore, the actual velocity of a small particle is not the true air velocity. The true air velocity is given by the extrapolation of velocity data from larger particles.

5.4.1 Charged Particle Aerodynamics

This section investigates the dynamics of a charged dust particle in fluid flow. Equation (5-5) shows the sum of the forces in one dimension for a particle experiencing two forces: Stokes drag and electrostatic.

$$\Sigma F = \frac{\pi d^3 \rho_p \dot{v}}{6} = 3\pi\mu d(u - v) + qE \tag{5-5}$$

Mass has been written in terms of particle density and volume, and acceleration is best described as $\dot{v}$, the time derivative of velocity. The air velocity, u, charge, q, and electric field, E, are assumed constant for all time. The solution to the first order differential equation takes the form shown in Equation (5-6), where the time constant f_p represents the reaction frequency of the particle and is given in Equation (1-4), and C_1 and C_2 are constants that depend on boundary conditions. The initial particle velocity was assumed zero and the final particle velocity is given by the force balance between the electrostatic force and Stokes drag given in Equation (5-7). The solution for the particle velocity is given in Equation (5-8)

$$v = C_1 e^{-f_p t} + C_2 \tag{5-6}$$

$$v_f = u + \frac{qE}{3\pi\mu d} \tag{5-7}$$

$$v = u\left(1 - e^{-f_p t}\right) + \frac{qE}{3\pi\mu d}\left(1 - e^{-f_p t}\right) \tag{5-8}$$

The particle reaches its final velocity more quickly if f_p is large, but unlike standard PIV, the electrostatic force will change the final velocity depending on the charge and electric field signs and magnitudes.

Figure 5-6 plots the velocity of a 1250 nm particle with an f_p value of 200,000 kHz (5μs) as given in Table 3-1. The electric field is set to $1x10^6$ V/m, while the charge varies between 100, 0, and -100 elementary charges. If the particle isn't charged, it accelerates to the air speed as would be the case in flow that does not include plasma effects. When the particle charge is positive, the electric field helps the particle move faster than the air flow. When the charge is negative, the electric field reduces the particle's final speed. For the chosen parameters, the charged particles have a velocity difference of 0.073 m/s when compared to the uncharged particle.

Smaller particles have been found to have faster velocities than larger particles. A very small sized particle follows the flow better, but if the particle is charged, the extra forces will affect its speed. The final velocity of a particle is given in Equation (5-7). Taking the limit of velocity as the diameter approaches zero leads to the velocity of a zero nanometer diameter particle. Three possible scenarios exist at this limit.

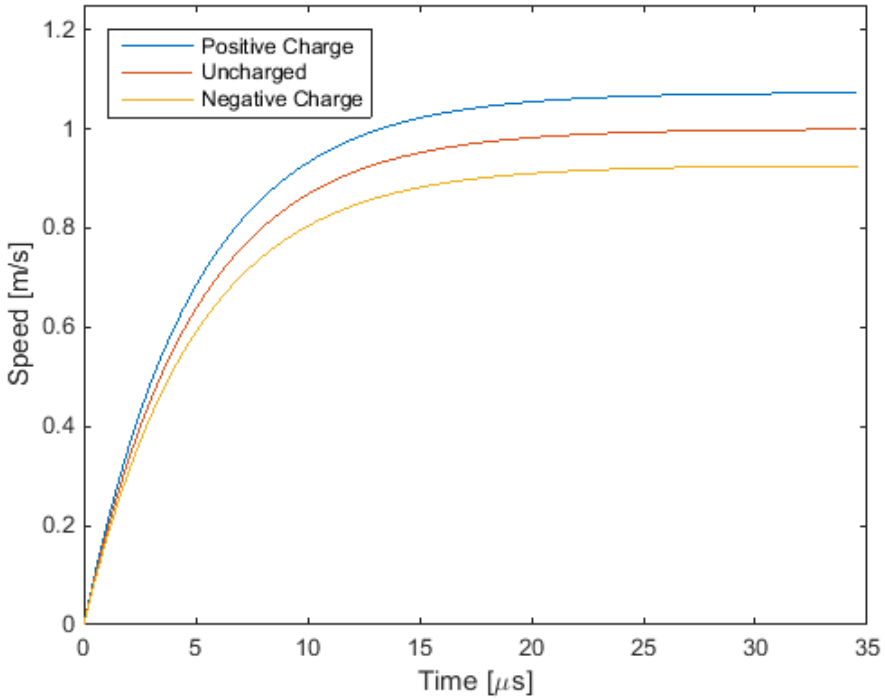

Figure 5-6. Step response of a 1250 nm particle that is charged positive (blue), charged negative (yellow), or uncharged (red).

First, the charge remains constant for all particle sizes. In this case, in the limit as the diameter decreases to zero, the ratio of *q/d* would increase and smaller particles would not closely follow the flow. Stokes drag acts weakly on smaller particles, so to compensate for the constant electrostatic force, the velocity difference would increase. This scenario can occur if the particle charge is quantized. A particle may have one or two electrons on it, but not a half or 1.86. As such, a large particle and a small particle could both be charged with one electron. This scenario does not apply to the data presented in this work. Chapter 6: focuses on forces acting on the particles and will show that particle charge is on the order of 100s of electrons. For the forces to match with a singular charge, the electric field magnitude would have to be on the order of $1x10^8$ V/m, which is too large for plasma actuators.

Second, the charge could decrease linearly with diameter. In this case, the final velocity of all particles, regardless of size, would be the same. If $q=s_q*d$, where s_q is the slope of the linear dependence, then the ratio of q/d would reduce to a constant for all particle sizes. Smaller particles would have the same speed as larger particles. This is not observed in the data. As such this scenario is not considered.

Third, the charge could decrease at a higher power law with respect to diameter. Assuming the charge has a square relation with diameter, $q \sim d^2$, then the ratio of q/d would lead to a linear relation between the final particle velocity and the particle diameter. In the limit as particle diameter approaches zero the final particle velocity would be the true air velocity. It is not important that the charge relation is quadratic, as assumed above, only that the power law relation is larger than linear.

5.4.2 Extrapolation

Because this is the first work to attempt an extrapolation to the 0 nm particle diameter, and because the uncertainty is large, a simple linear fit was used to extrapolate the true air velocity as opposed to assuming higher order fits. Figure 5-7 applies the linear fit and extrapolation to the data at (5.24, 0.42) mm and 192° phase. The error bar for the 0-nm velocity was calculated by extrapolating the error bars for the other particle sizes. The difference between the air velocity and the 300 nm particles is 0.05 m/s and increases to 0.25 m/s for the 500 nm particles. With a difference of 0.48 m/s, the 1250 nm particles have a 13% error in measuring the true airflow.

The true airflow was calculated for all vectors and phases. Figure 5-8 shows the velocity fields for the air flow, and the 500 nm and 1250 nm particles at 264° phase.

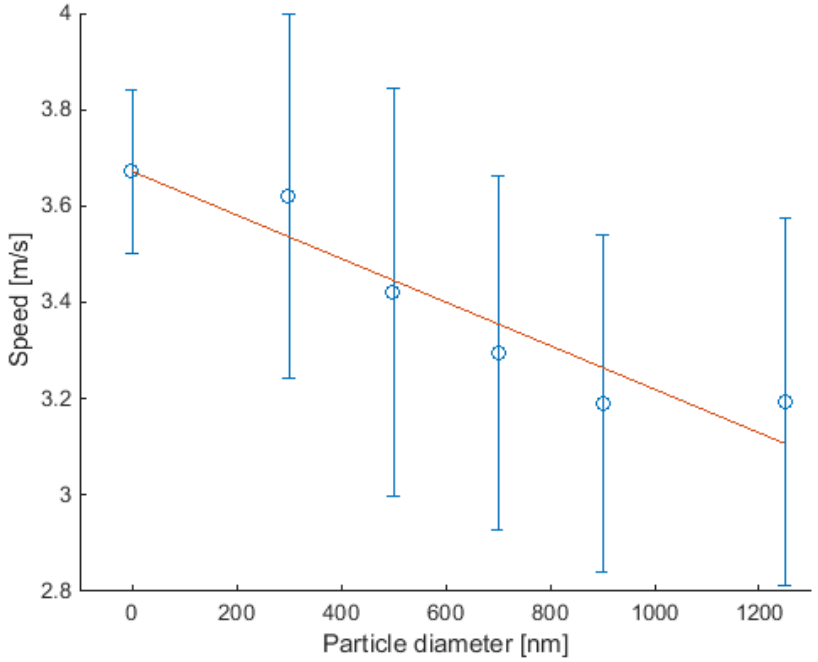

Figure 5-7. Linear fit extrapolation and error bars at (5.24, 0.42) mm and 192° phase.

Qualitatively, the particles' velocity fields match the shape of the air flow and properly present the basic dynamics.

Air is drawn into the actuator from above and accelerated forward. Farther downstream, a larger boundary layer develops and the jet expands. The 500 nm and air velocity field regions near the electrode are faster than the 1250 nm. The largest error for

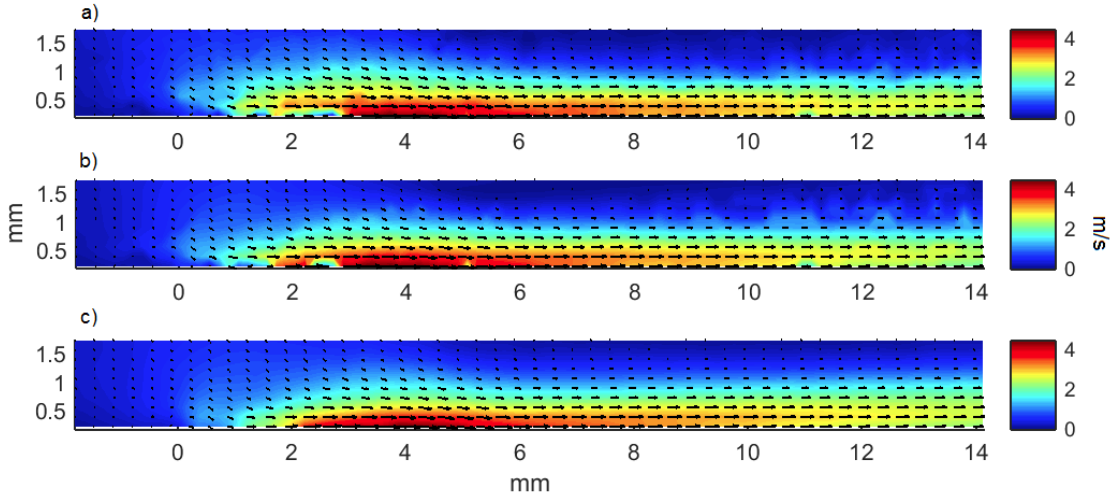

Figure 5-8. Velocity fields for the a) air, b) 500 nm, c) 1250 nm.

larger particles occurs near the plasma actuator top electrode, at the location of flow acceleration.

Figure 5-9 shows the difference in velocity between the air and the 1250 nm particles at 4° phase. Differences of 1 m/s are present near the electrodes and quickly diminish farther downstream. It is not surprising that the area most affected by the electric field is the area near the electrode. Larger particles struggle to closely match the airflow in high density plasma regions, where charging effects are strongest.

The preceding discussion has focused on the large differences between particles but it should be mentioned, and it can be seen, that larger particles accurately follow the flow in many regions of the plasma actuator flow field, such as farther downstream or upstream. Forcing effects from the electric field in these regions could be diminished from the lack of strong electric fields or the lack of particle charging due to low plasma density, or lack of strong differences in plasma species mobility and density.

As noted in the literature review section, many PIV studies use olive oil as a seeding medium. Olive oil droplets are, on average, about 900 nm in diameter. From this study, it is seen that 900 nm particles do not give accurate results for plasma actuator flow. DEHS is another popular oil used in PIV studies. On average, DEHS produces droplets with a diameter of about 300 nm, a smaller and better suited particle. Further studies should be conducted to determine the effect of plasma on oil droplets and poly-disperse particles for PIV measurements.

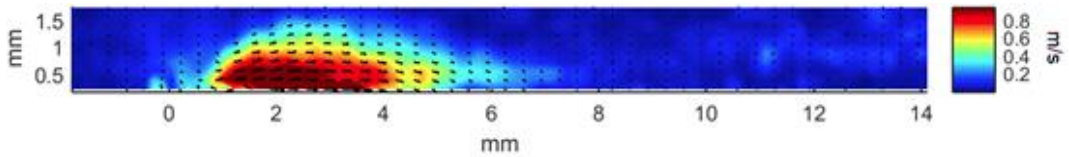

Figure 5-9. Velocity difference between the air and the 1250 nm particles at 4° phase.

5.4.3 Acceleration

The acceleration field for the air was calculated using the equations and analysis in section 4.4 for the particles. Figure 5-10 shows the acceleration field for the air at 4°, 91°, 192°, and 278° phase angles. The magnitude is still on the order of 10,000 m/s^2. The majority of the acceleration occurs between 91° and 192° phase with the majority of the deceleration occurring between 278° and 4° phase, much like the particle accelerations.

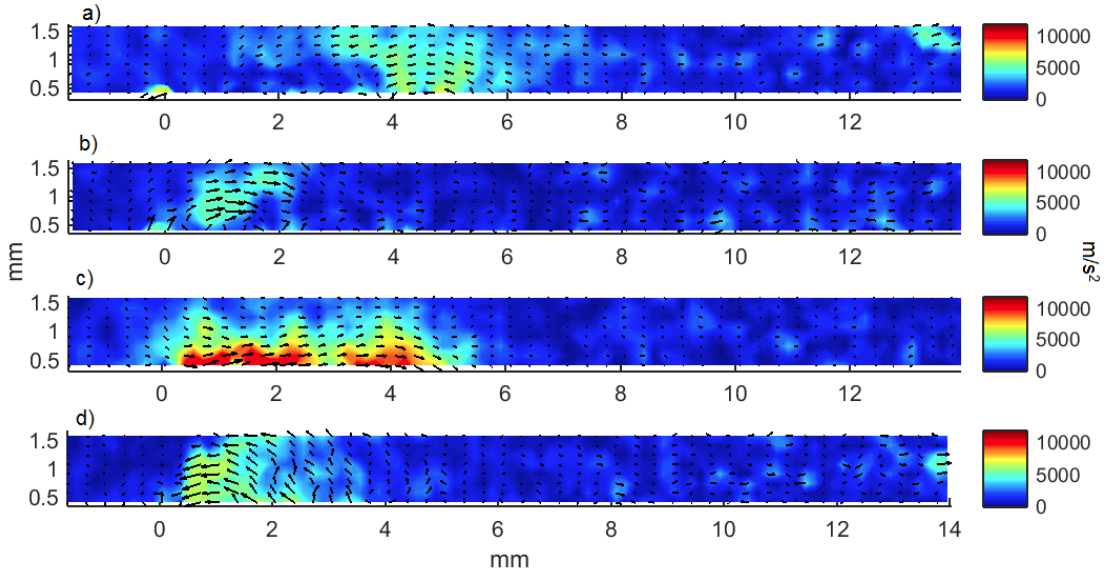

Figure 5-10. Acceleration field for air: a) 4°, b) 91°, c) 192°, and d) 278° phase.

Unsurprisingly, time and convective velocity derivatives also follow the trends of the particles. Figure 5-11 shows the ratio of the time derivative to the total derivative. Strong convective accelerations can be seen around 2 mm downstream and exist mostly between 4° and 91° phase. During other phases, the time derivative is more dominant throughout.

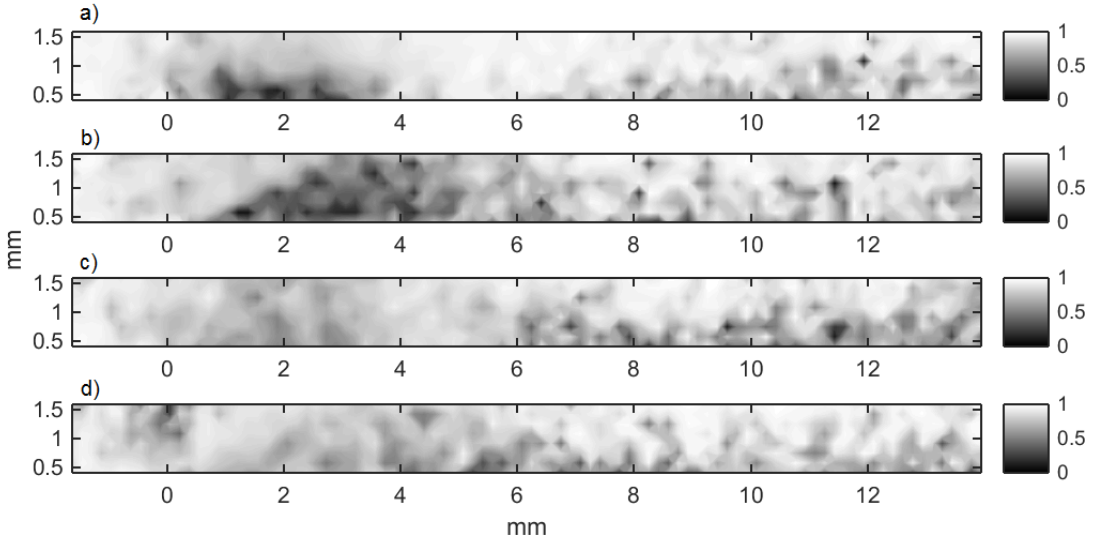

Figure 5-11. Ratio of time derivative to total derivative for air acceleration at a) 4°, b) 91°, c) 192°, d) 278° phase angle.

The previous plots provided a qualitative view of the air acceleration. Focusing specifically at (2.22, 0.42) mm and (5.24, 0.42) mm, Figure 5-12 plots the total, time, and convective derivatives for all phases and shows the quantitative differences between the comparatively smooth particle acceleration plots shown in Figure 4-9 and the derivative results of an extrapolated quantity.

Many flow characteristics observed with particle accelerations can be seen in the air acceleration results. The time derivative spikes up at 148° phase for the 2.22 mm location and at 48° and 206° phase for the 5.24 mm location, much like the accelerations of the particles. Decelerations at 292° and 350° phase at 2.22 mm and 5.24 mm respectively match the decelerations of the particles.

The air acceleration is not as smooth as the particle acceleration. Kinks and turns can be seen throughout most of the cycle and even the convective derivative, which stays mostly constant for particles, has a larger variability. The large variability of the air acceleration is due to the noise inherent in taking the derivative of a quantity.

Furthermore, the quantity being differentiated, the velocity of the air, is extrapolated from data with moderate uncertainty. Both the uncertainty and the derivative operation increase the level of noise for the result. Extrapolation can provide a good estimate of the air velocity but only a noise estimate of the air acceleration.

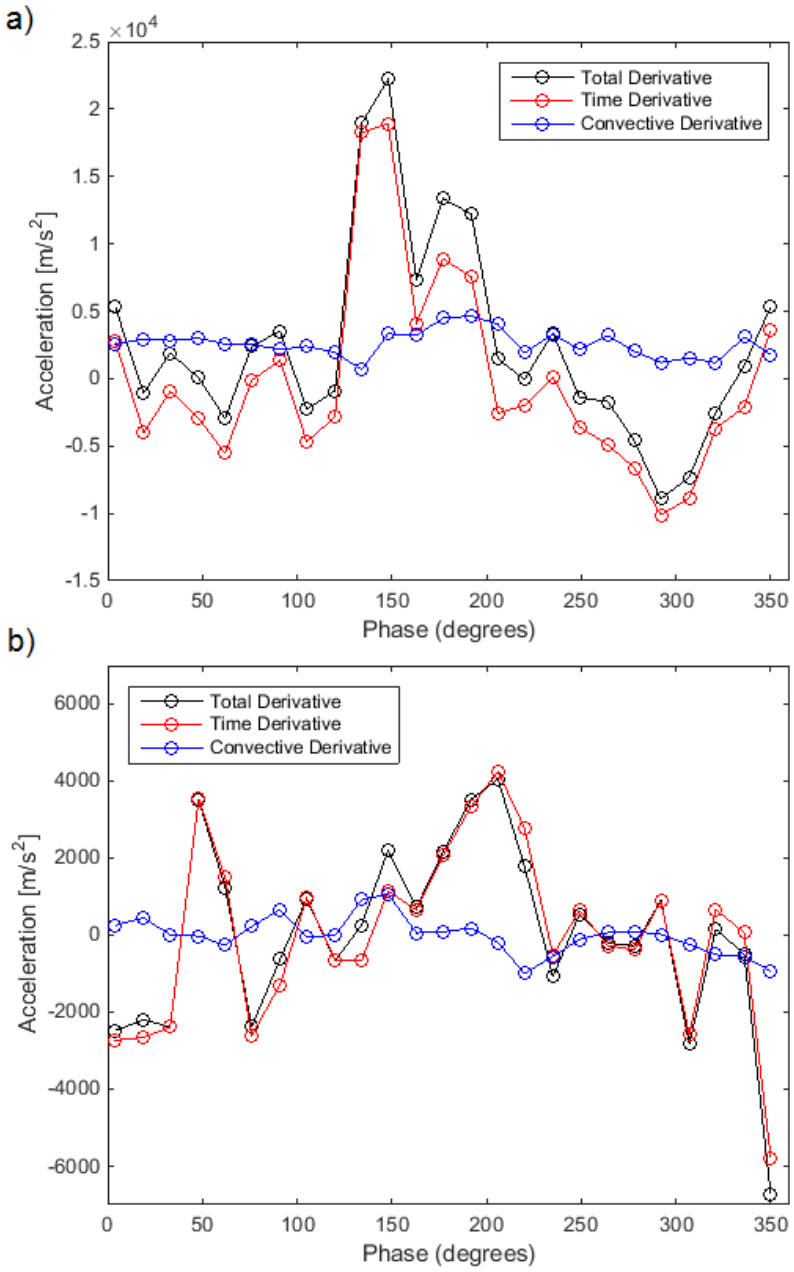

Figure 5-12. Derivatives of air velocities at a) (2.22, 0.42) mm and b) (5.24, 0.42) mm. The total derivative is shown in black, the time derivative is shown in red, and the convective derivative is shown in blue.

Chapter 6: Forces

Significant differences were discovered between particle velocities and the causes for these differences are investigated in this chapter. PIV particles experience many forces within fluid flow with Stokes drag being the predominant force. Secondary forces, such as gravity and buoyancy, were investigated and shown to have a minimal effect on the velocity, leaving only the electrostatic force as the reason for the velocity differences.

6.1 PIV Aerodynamic Forces

Stokes drag is the prevalent force acting on PIV particles, while secondary effects include those from gravity, buoyancy, Reynolds number corrections, etc. Equation (6-1) shows the Stokes drag force and combination of gravity and buoyancy acting on a PIV particle where ρ_f is the density of the fluid and φ serves as a correction for finite Reynolds numbers

$$\Sigma\vec{F} = 3\pi\mu d(\vec{u} - \vec{v})\varphi + \frac{\pi d^3}{6}\left(\rho_p - \rho_f\right)\vec{g} + \mathcal{O} \tag{6-1}$$

Higher order forces are represented by $\mathcal{O}$. Gravity and buoyancy depend on known material constants, for which ρ_f is taken to be 1.225 kg/m^3. Calculating Stokes drag requires the air velocity field, which has been extrapolated and can be used to calculate the force on each particle. The particle Reynolds number is given in Equation (6-2)

$$Re_p = \frac{\rho_f d|\vec{u} - \vec{v}|}{\mu} \tag{6-2}$$

A large velocity difference for the 300 nm particle is 0.2 m/s, and 1.0 m/s the 1250 nm particle, which leads to a particle Reynolds number of 0.04 and 0.08 respectively. The

Reynolds number correction factor, φ, is calculated using the particle Reynolds number. For the range of $0.01 \leq Re_p \geq 20$, φ is calculated using Equation (6-3)[64]

$$\varphi = 1 + 0.131 * (Re_p)\text{^}\left(0.82 - 0.05log_{10}(Re_p)\right) \tag{6-3}$$

Correcting Stokes drag for finite Reynolds numbers over the particle doesn't account for the large difference in velocity compared to air. For that range of Reynolds number, the correction factor increases the Stokes drag force by 0.7% and 1.4% for the 300 and 1250 nm particles respectively. One percent is too small of a value when compared to the uncertainty in the measurements and the difference in velocity between particles. As such, Stokes drag is calculated without the correction factor.

Figure 6-1 shows the calculated Stokes drag force for the linearized 700 nm particles. It was assumed that the viscosity remains constant inside a weakly ionized environment. Hogg studied the viscosity of air and found no discernable differences for weakly ionized air[108]. Murphy examined transport coefficients of air plasma from 300 K to 30,000 K and found that differences became significant only for temperatures greater than 1,000 K[109]. Strong forces with magnitudes on the order of tens of picoNewtons exist near the electrode that extend vertically to the top of the field of view and 6 mm downstream. Other particles experience similar force fields but with different magnitudes; larger particles experience magnitudes on the order of hundreds of picoNewtons. Farther downstream, the force weakens, but in general, remains on the order of 1 picoNewton, which is the value used for comparing other forces.

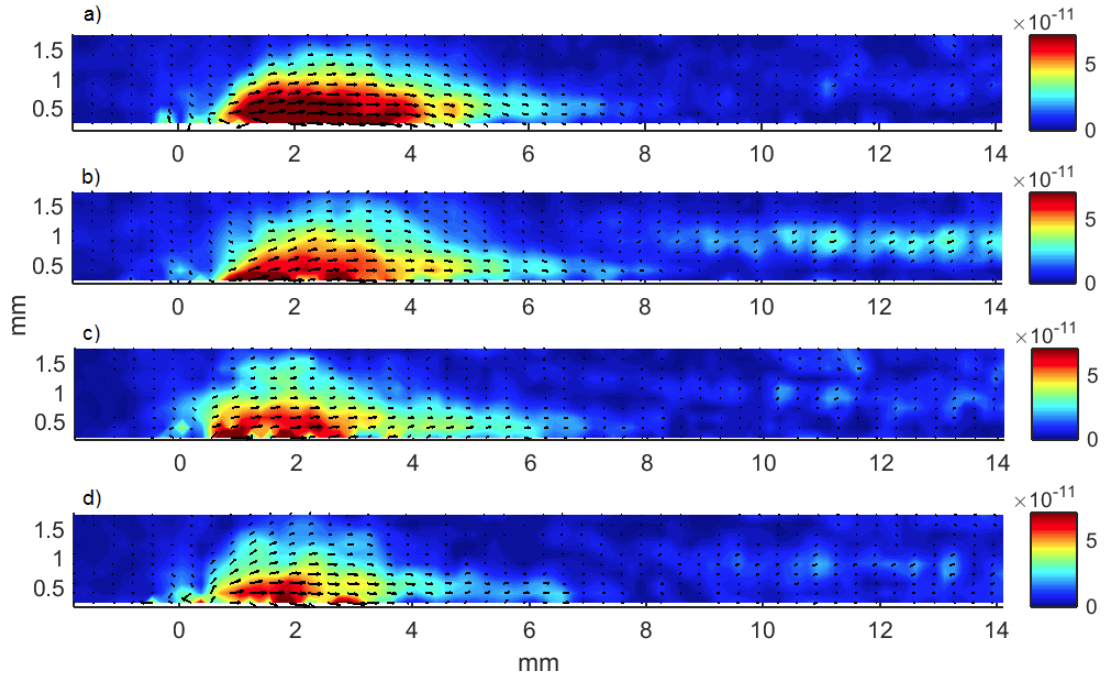

Figure 6-1. Stokes drag force field in Newtons for the 700 nm particles at a) 4°, b) 91°, c) 192°, and d) 278° phase angles.

Contributions from secondary forces, like buoyancy, are too small to be considered. The combination of gravity and buoyancy impart only 0.14 femtoNewtons to the 300 nm particles, while the 1250 nm particles feel a 0.01 picoNewton force acting on them. Therefore, gravity and buoyancy are also not taken into account.

Other secondary forces include the history force, the added mass force, and the fluid stress force[64]. All of these forces depend on the acceleration of the fluid and the particle. Large acceleration magnitudes are on the order of 10,000 m/s^2. The 700 nm particles have a mass of $1.8*10^{-16}$ kg, which, under observed accelerations, corresponds to an inertial force of 1.8 pN. As seen in Figure 6-1, the regions with the largest acceleration experience forces on the order of 50 pN or more. The effects from secondary forces and corrections are not considered in this work. Uncertainty measurements are too large to be caused by secondary effects; and the secondary forces are too weak and incapable of affecting the particles to the extent seen in the experiments. Standard PIV

effects for the velocity difference of the particles have been quantitatively excluded. A different force must be acting on the particles.

6.2 Electrostatic Forces

Plasma actuators need to reach electric field strengths that surpass the breakdown field of air, 3 MV/m. The strong electric fields present in the actuator impart kinetic energy to the ions, which induce airflow. These fields also act on the charged PIV tracer particles. Assuming an electric field strength of ~1 MV/m and a charge of 100 elementary charges on a tracer particle, the electrostatic force on that particle would be 16 pN, the same order of magnitude as the Stokes drag force acting on said particle.

6.2.1 Particle Charging, A Closer Look

A review of particle charging was given in chapter 2. This section examines, in more detail, the theoretical works for high pressure charging. Based on the work by Khrapak et al.,[89] and following the details in the works by Chang and Laframboise[81] and Kennedy and Allen[87], two theories formulate the basis for particle charging in atmospheric plasma – partially collisional and fully collisional. For the former theory, electrons are assumed non-collisional and follow OML theory dynamics while ions are assumed collisional. Khrapak et al. used the name, partially collisional, to describe this theory. The second theory, described as fully collisional, assumes that both the ions and electrons are collisional. Chang and Laframboise[87] derive expressions for collisional current toward a dust particle that depend on a collisional parameter *k*. This work simplifies the definition of *k* to a ratio of mean free path to particle radius. Equations

(6-4) and (6-5) equate the positive and negative currents to the particle for the partially collisional and fully collisional case respectively.

$$\frac{4\pi r q n_+ D_+ {}^{\varphi}/_{\varepsilon}}{1-\exp({}^{-\varphi}/_{\varepsilon})} = \sqrt{8\pi} q r^2 n_e v_{te} \exp(\varphi) \tag{6-4}$$

$$\frac{4\pi r q n_+ D_+ {}^{\varphi}/_{\varepsilon} \exp({}^{-\varphi}/_{\varepsilon})}{1-\exp({}^{-\varphi}/_{\varepsilon}) + k_+ {}^{\varphi}/_{\varepsilon}} = \frac{4\pi r q n_e D_e \varphi \exp(\varphi)}{\exp(\varphi) - 1 + k_e \varphi} + \frac{4\pi r q n_- D_- {}^{\varphi}/_{\varepsilon} \exp({}^{\varphi}/_{\varepsilon})}{\exp({}^{\varphi}/_{\varepsilon}) - 1 + k_- {}^{\varphi}/_{\varepsilon}} \tag{6-5}$$

In the equations, r is radius, n is density, D is the diffusion coefficient, φ is the normalized particle potential, and ε is the ratio of ion to electron temperatures. The subscript symbols, +, -, and e, correspond to positive ions, negative ions, and electrons. The contribution from positive ions is placed on the left side and equated to the contributions from electrons and negative ions. Negative ions are only considered in the fully collisional case.

The partially collisional equation easily reduces to a linear dependence for the radius. While at first glance it appears as if there will be no radius dependence for the fully collisional case, k is the ratio of mean free path to radius, so both cases depend on the particle size.

Khrapak's analysis was followed for the partially collisional theory with the diffusion coefficient, approximated as the product of mean free path and thermal velocity. Einstein's relation, $D=\mu_q K_b T$, where μ_q is the charged particle mobility and K_b is the Boltzmann constant, was used to relate diffusion to mobility and temperature for each species in the fully collisional theory. Both sets of ions were assumed to have a temperature of 400 K, while electrons were assumed to have a temperature of 11600 K. The assumed 1 MV/m electric field and 2.5E25 m^{-3} air density equate to 40 Townsend

(Td). Interpolating data from Nielsen and Bradbury[110] and from Frommhold[111] from the LXCat database[112], electron mobility was approximated as 0.064 m^2/V-s. Ion mobility in air is still a topic of research with a plethora of species and results[113-115]. Positive and negative ion mobility were approximated as $2.5x10^{-4}$ and $2.0x10^{-4}$ m^2/V-s respectively. For such a high-pressure plasma, voltage was related to charge through the vacuum capacitance of a charged sphere.

Figure 6-2 shows the charge in units of electrons present on a particle for a given diameter for both partially collisional (PC) and fully collisional (FC) formulations. The plasma is always assumed perfectly neutral such that $n_+=n_-+n_e$. The different lines represent the ratio of electrons to positive ions with the remaining negative charges as negative ions. For a ratio of zero, an ion-ion plasma exists, while for 100% the plasma is composed of electrons and positive ions only.

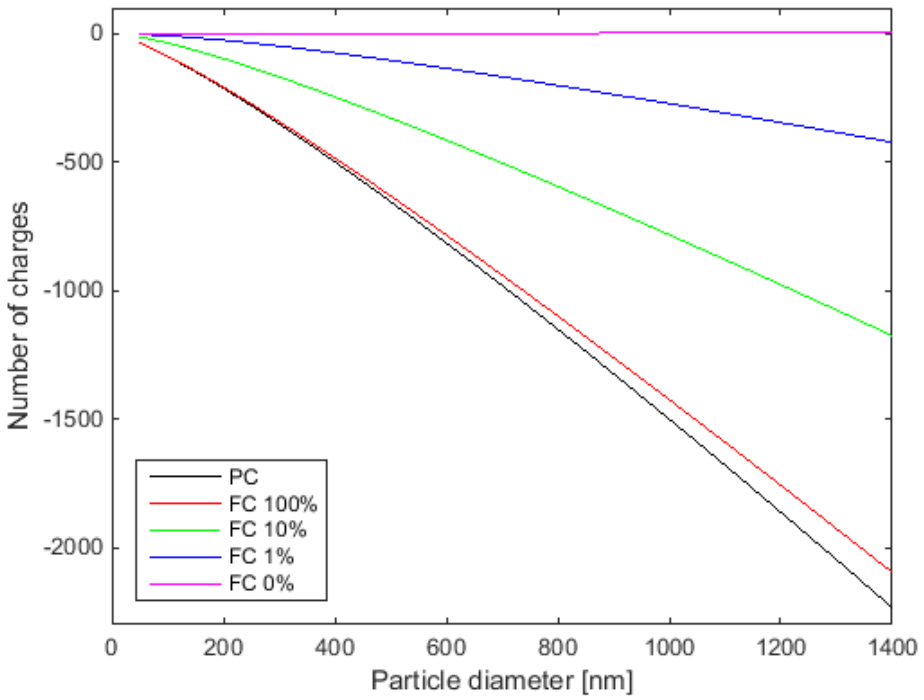

Figure 6-2. Elementary charges on a particle of a given diameter for partially collisional plasma and fully collisional plasma with electron to positive ion percentage.

For the given parameters, a particle with a 300 nm diameter charges to about 300 electrons in a partially collisional plasma, while a 1250 nm diameter particle charges to about 2000 electrons. An electric field on the order of 1 MV/m would impart a 160 pN force on a particle with 1000 charges on it. The magnitude of the electrostatic force can approach and surpass that of the Stokes drag force and significantly affect the tracing ability of a particle.

It is interesting to note the similarity between the partially and fully collisional theory results. At one atmosphere and for the chosen values, electrons are not significantly limited in their mobility as seen by the small difference between the fully collisional and partially collisional results. For a 1250 nm particle, the difference in charge between the partially collisional charge and the fully collisional charge is 108 electrons, or, less than 6%. For an ion-ion plasma, the values are positive because the chosen mobility of positive ions is larger than that of negative ions. It has been shown that particle can gain a positive charge if the negative ions have reduced mobilities compared to the positive ions[102, 103].

In section 5.4.1, it was determined that in order for the extrapolation to 0 nm to lead to the true air velocity, the charge must vary more than linearly with particle size. From Figure 6-2, it can be seen that the charge is not a linear function of size. Still, Figure 6-3 plots a linear fit and a quadratic fit for the partially collisional data. Both fits have a zero intercept. A quadratic dependence fits the data more accurately than a linear fit. A higher order polynomial can be used to improve the fit, but the importance of the fit is the power being greater than linear.

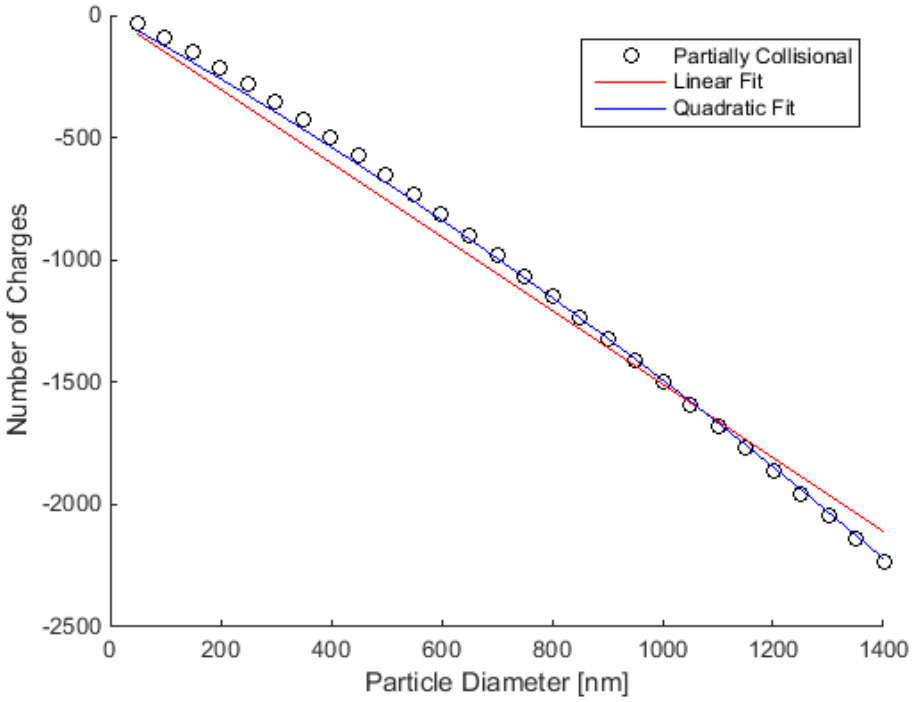

Figure 6-3. Linear fit (red) and quadratic fit (blue) for partially collisional particle charge.

6.2.2 Calculating the Electrostatic Force

Newton's second law applied to the particles has been reduced to the sum of two forces, Stokes drag and the electrostatic force. The particle acceleration term was calculated in Chapter 4. Stokes drag was calculated in the preceding section. Secondary PIV forces were ignored due to their weak effects. The electrostatic force is the only other force acting on the particles. Equations (6-6) and (6-7) show the sum of the forces for the particles in the x and y-directions.

$$\Sigma\overrightarrow{F_x} = m\vec{a}_x = \vec{F}_{SDx} + \vec{F}_{Ex} = 3\pi\mu d(u_x - v_x) + q_p E_x \tag{6-6}$$

$$\Sigma\overrightarrow{F_y} = m\vec{a}_y = \vec{F}_{SDy} + \vec{F}_{Ey} = 3\pi\mu d\left(u_y - v_y\right) + q_p E_y \tag{6-7}$$

Figure 6-4 shows the electrostatic force for the 700 nm particles. Strong forces exist near the top electrode and persist downstream. Larger particles, which have a higher charge, experience stronger forces. Near the electrode, 300 nm particles experience forces on the order of 10 pN, while 1250 nm particles experience forces on the order of 200 pN.

As for the dependence on phase, electrostatic forces are strongest when the voltage changes from negative to positive values from 321° to 4° phase. Particles experience larger forces during the positive voltage part of the cycle. The force near the electrodes always points upstream for every phase. The electric field pulls the particles back and reduces their speed and ability to match the airflow, as was seen through velocity comparison. Always pointing upstream implies that the particles charge negatively when the electrode voltage is positive and charge positively when the electrode voltage is negative. However, the force during the negative voltage half cycle has a lower magnitude when compared to the positive voltage half cycle. Either the charge or the electric field, or both, have a lower magnitude.

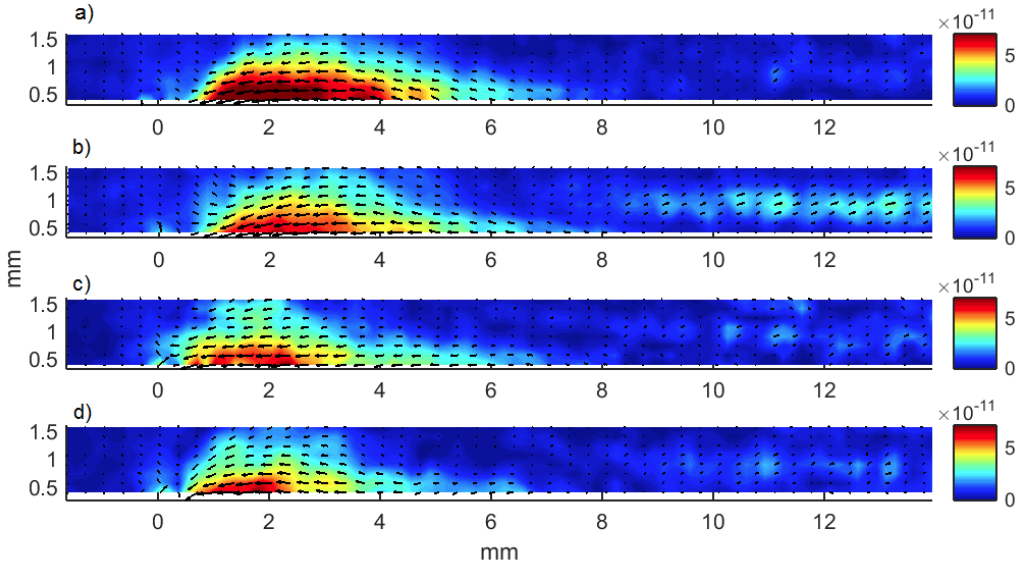

Figure 6-4. Electrostatic force in Newtons acting on the 700 nm particles at a) 4°, b) 91°, c) 192°, and d) 278° phase angle.

The electrostatic force looks to be equal and opposite the Stokes drag force. The difference between the two is the inertial force of the particle, mass times acceleration. Acceleration magnitudes for the largest, 1250 nm, particle are on the order of 12,000 m/s^2. The mass of one 1250 nm particle is 1e-15 kg with an inertial force of 12 pN, hardly enough to compare with the 150 pN forces. Therefore, to within 8 percent, Stokes drag and the electrostatic force are equal and opposite.

6.2.3 Comparison of Linear and Average Data Points

For the aforementioned results, the linear fit points were used to illustrate the Stokes drag and electrostatic forces as opposed to the average data points from the PIV results. Due to the large uncertainty of the data, the linearized points were favored for presentation. Differences between the two sets are discussed here.

Smaller particles have larger percentage differences between the sets. The 300 nm particles do not share many characteristics between them as shown in Figure 6-6. Due to the large percentage difference between small numbers, force measurements for smaller particles seem to contradict each other. Stokes drag depends on the difference between the extrapolated air velocity and the particle data. Figure 5-7 shows the less than 0.1 m/s difference between the linear fit point and the average data point. The difference in magnitude between the linearized force field and the average data force field is only 1 or 2 pN. However, the percent difference between the air velocity is large, which significantly affects Stokes drag. Larger particles don't suffer from the same problem.

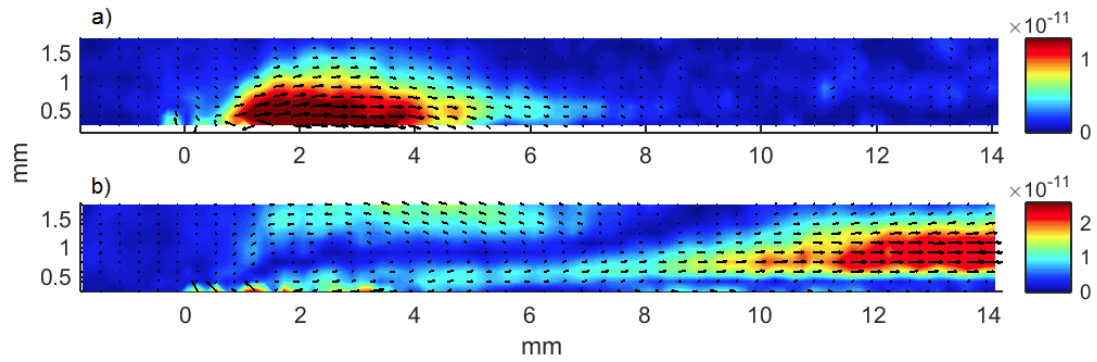

Figure 6-6. Stokes drag acting on the 300 nm particles, a) linearized, b) average data.

Figure 5-7 shows a similar difference between the linear and average data point for the 1250 nm particle but the percent difference is much smaller. Figure 6-5 shows just how similar the calculated forces can be. It is for this reason that linear fits are used for presenting force data as opposed to the average data point from the PIV results.

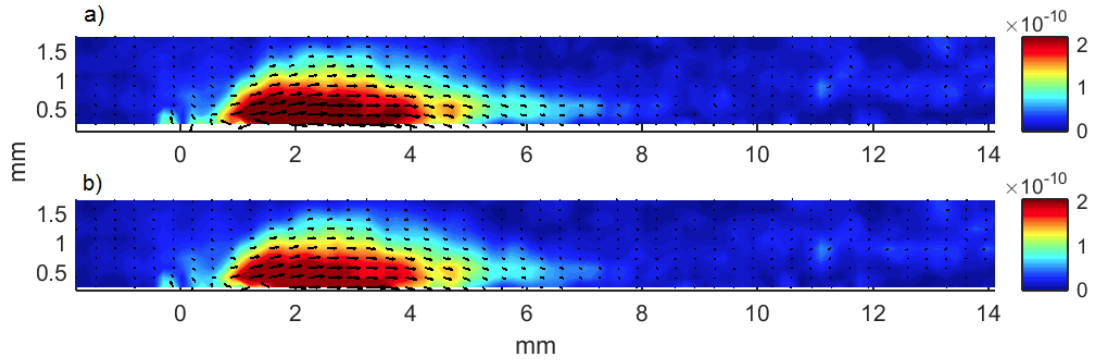

Figure 6-5. Stokes drag acting on the 1250 nm particles, a) linearized, b) average data.

6.3 Charge and Electric Field

The electrostatic force acting on the particles is an important discovery for the analysis of plasma actuators. The electric field and charge are even better. Unfortunately, separating the charge and the electric field from the force is not possible with the current set of equations. There are three unknowns: the charge of the particle, the electric field in the x-direction, and the electric field in the y-direction. One particle set provides two

equations, sum of the forces in the x and y. This is not enough to solve the system of equations, but, using two particle sets, the number of equations increases to 4, two for each particle, and the number of unknowns increases to 4. Therefore, the system can, in principle, be solved. However, the last equation can be derived from the previous 3 and is therefore dependent.

The ratio of the x- and y-direction forces acting on a particle is calculated by taking Equation (6-6) and dividing it by Equation (6-7), which is shown in Equation (6-8). This relation holds true for all particles because of the equivalent electric field assumption between particle pairs. Therefore, the ratio of Stokes drag for one particle can be equated to another particle as shown in Equation (6-9). This means that given two particle sets, only three equations are independent since the fourth velocity can be derived from the other three using Equation (6-9)

$$\frac{F_{SDx}}{F_{SDy}} = \frac{F_{Ex}}{F_{Ey}} = \frac{E_x}{E_y} = \frac{u_x - v_x}{u_x - v_y} \tag{6-8}$$

$$\frac{u_x - v_{1x}}{u_x - v_{1y}} = \frac{u_x - v_{2x}}{u_x - v_{2y}} \tag{6-9}$$

Although not immediately obvious, the assumption that the electric field stays the same for each particle allows for the derivation of the fourth equation from the other three. Including another particle increases both the number of equations and unknowns. An equation outside of the force balance is needed to solve the system. Maxwell's equations immediately come to mind for the electric field. Gauss's law requires information about charge density, which is not available. No magnetic field was applied so it holds true that $\nabla \times \vec{E} = 0$. The downside of the curl of E is that it's a differential equation and requires boundary conditions.

To the author's knowledge, the only boundary conditions obtained for plasma actuator electric fields were from works using V-dot probe experiment like the work of Enloe et al[31]. However, the data pertains to only one side and at least one more is needed to solve for the field. A zero electric potential boundary condition was applied to the top and upstream boundaries to attempt a solution, but the results were infeasible with electric field strengths ranging from $1x10^3$ V/m to well over $1x10^7$ V/m for the adjacent vector. It has also been shown that the charge on a particle is independent on the electric field unless that electric field is strong enough to accelerate the ions to hypersonic speeds[91]. The electrostatic force is the product of two independent variables. Separating the charge and electric field from the force data remains a hurdle for the future. Information can still be gleaned through force data. Direction information about the electric field can be inferred from the force. The electric field direction is either in line with or opposite to that of the force depending on the particle charge. Near the electrode, the force always acts upstream. When the electrode voltage is at a positive or negative maximum, the electric field should point either downstream or upstream. Yet the force always acts upstream. The particles charge negatively when the voltage is positive and positively when the voltage is negative.

Figure 6-7 shows the direction of the normalized force vectors for the region near the electrode superimposed on the force magnitude at 91° phase, during maximum positive voltage. The vectors are normalized and reversed to point in the correct direction and give a better visual of the electric field. The electric field expands upward and outward from the top electrode and remains parallel to the plasma actuator for 3 mm before converging toward the dielectric. There is a gap between the tip of the electrode

and when the force and electric field increases. The gap is probably due to the top electrode reflecting so much that the particles around it become hard to discern. The data around the top electrode is not trustworthy because of that reflection.

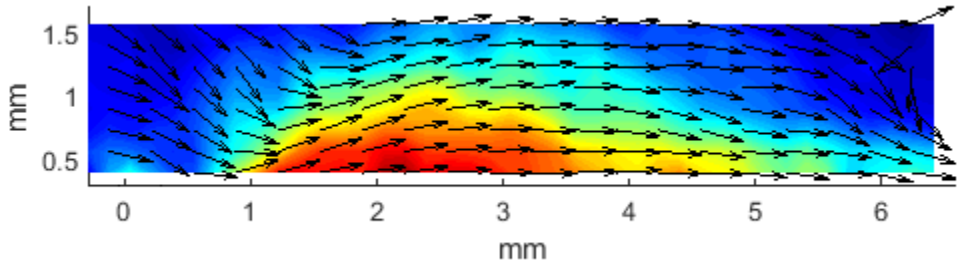

Figure 6-7. Normalized and reversed electrostatic force vectors overlaid on the force magnitude at 91° phase.

6.4 Comparison with Literature

Enloe et al.[31] and Nichols and Rovey[32] conducted V-dot probe experiments that measured the longitudinal electric field along the dielectric. Their results showed that the voltage near the top electrode followed the applied electrode voltage, but farther downstream the voltage was always positive and the electric field pointed downstream. The electrostatic force presented here could not be separated into charge and electric field; none-the-less, a comparison can be made to the boundary electric field values.

Figure 6-8 plots the linearized electrostatic force experienced by the 1250 nm particles from the top electrode downstream till the end of the interrogation area at 0.42 mm above the dielectric. Only half the phases are shown as to not cloud the plots. Large negative forces exist near the electrode and, during some phases, a small force surfaces downstream starting at around 8 mm. The negative forces near the electrode vary in magnitude between 150 pN and 300 pN. The largest forces appear between 307° and 4° phase.

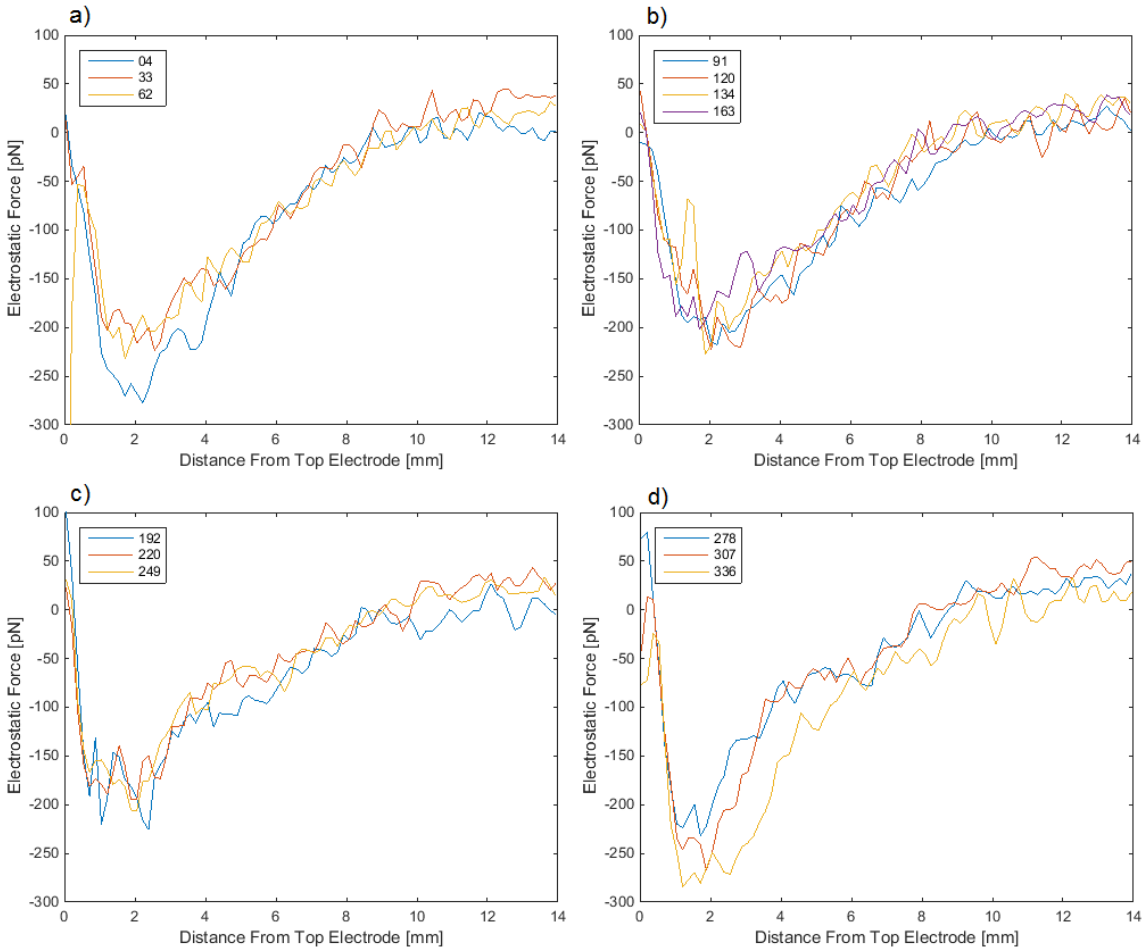

Figure 6-8. Electrostatic force in picoNewtons from the top electrode to the end of the interrogation window at 0.42 mm above the dielectric at phases a) 4°, 33°, 62°, b) 91°, 120°, 134°, 163°, c) 192°, 220°, 249°, d) 278°, 307°, 336° phase angles.

Unlike the results from the V-dot probe experiments, which showed a maximum electric field at the top electrode, the force calculated in the current experiments diminishes next to the electrode. A couple of reasons could lead to this difference. First and foremost, the reflection from the electrode obscures the particles near that region and reduces the accuracy of PIV. Secondly, the force is the product of charge and electric field, which are independent quantities. It is possible that the particles don't gain a large charge near the electrode, reducing the experienced force.

What remains true is that the force is negative and that the particles charge both negatively and positively. Farther downstream, the small force is sometimes positive with

magnitudes around 50 pN. It is known that the electric field is always positive after 8 mm, which implies that the particles charge positively after they pass the 8mm mark. However, the large uncertainty in velocity measurements diminish the reliability of these measurements, and the small but existent downstream force is difficult to compare with results from experiments in the literature. A boundary layer-like phenomenon can be seen in Figure 6-4 for the electrostatic force at 91° phase angle. It is highly unlikely that the electric field or the charge increased significantly from the dielectric boundary. Rather, the observed force boundary layer is a remnant of the air boundary layer and the inability of the simple force model to account for complex flows.

Chapter 7: Conclusions

Particle image velocimetry is a powerful tool for characterizing plasma actuator induced flow. However, dusty plasma physics has been absent from major PIV studies. The work presented here examined particle charging effects on PIV measurements. Experiments were conducted using monodisperse polystyrene nanoparticles of different sizes. Uncertainty quantification was conducted simply by deconvolving the particle size from the correlation peak. Stokes drag and the electrostatic force were shown to be the dominant forces. Secondary aerodynamic forces were calculated to be too small in comparison. Comparing with charging theories, particles charge to the same order of magnitude when considering electric field strengths of 1 MV/m.

7.1 Summary of Work

High speed PIV measurements were conducted on a plasma actuator operating with a sinusoidal voltage at 4.5 kV_{rms} and 2 kHz. The laser pulse time difference was set to 20 μs, which separated the cycle into 25 phases. Polystyrene nanoparticles were chosen as flow tracers because they can be manufactured to a precise size. The data set was composed of 5 particle sizes, 300 nm, 500 nm, 700 nm, 900 nm, and 1250 nm. A nebulizer, and a heater and cooler apparatus were used to seed the enclosure housing the plasma actuator. Two hundred fifty-six double images were taken for each phase and particle. The first six double images were discarded due to intensity.

Seeding density was low, and standard PIV processing would give a low vector density, so ensemble average processing was used to increase the vector density. An

initial window size of 64 x 64 was reduced to 32 x 32 with a 50% overlap to provide a vector every 0.16 mm. The interrogation region was composed of 12 vectors vertically and 98 vectors horizontally. Velocity uncertainty was quantified using the standard deviation of the correlation peak, which was approximated as a Gaussian peak. The correlation peak is the amalgamation of every effect in the calculation including particle displacement, particle image diameter, sensor noise, turbulence, and others. Only the particle image diameter, which was calculated through autocorrelation, was subtracted from the peak. The average velocity uncertainty measured 0.4 m/s at a 95% confidence value.

Velocity fields for each particle qualitatively matched each other and those in the literature for similar plasma actuator geometries. Velocities were larger during the negative voltage phases and the actuator showed a PUSH-push type of actuation. Peak accelerations were calculated to be on the order of 10,000 m/s^2. Smaller particles traced the airflow better than larger particles, especially near the electrode where the plasma and electric field are strongest. Differences between the 300 nm and 1250 nm particles can reach 0.7 m/s. A weighted linear fit was applied to each vector position and extrapolated to 0 nm size, which was taken as the true air speed. In certain areas and phases, the 1250 nm particles are slower than the air speed by 50%.

Stokes drag was calculated using the extrapolated air speed and the linearized velocity values for each particle. Secondary PIV forces, such as buoyancy, gravity, and Reynolds number were too small to be considered. The only remaining explanation for the variation of velocity relative to the flow field was the effect of particle charging and the electrostatic force from the strong electric fields. The electrostatic force was

calculated by subtracting out the effect of stokes drag. Because the particle mass and the acceleration were small, Stokes drag and the electrostatic force appear to be equal and opposite of each other.

The electrostatic force on the tracer particles near the plasma actuator appears to always act upstream; however, electric fields change direction for positive and negative voltages. This implies that the particles charge negatively when the electric field points downstream and the particles charge positively when the electric field points upstream. Results shown in this work corroborate simulations and experiments arguing that negative ions are very important in plasma actuator operation.

Unfortunately, with the current information, it was not possible to separate the electrostatic force into particle charge and electric field. Combining the force information for multiple particles always leads to one more unknown than the number of available equations. The curl of the electric field can, in theory, be used as a closing equation; however, boundary conditions are required to solve the system. The separation of charge and electric field remains a future work.

This work describes a method for correcting PIV results of plasma induced airflow. The method is not limited to plasma actuators and can be used for any flow that includes in it an ionized region. Stokes drag and electrostatic forces acting on a particle can be calculated using the methodology outlined above, which can provide information about the electric field and charge on the particles. This work has also shown theoretical charging models are within a factor of two in predicted the charge on a tracer particle in a high pressure plasma flow. This information can be used to compare and validate simulation results that specifically solve for the electric field, the plasma density, and the

temperature. Using the information available from a simulation, the theoretical particle charge can be calculated and compared to experiments. Lastly, this work raises awareness in the plasma actuator community about the errors present in PIV results.

Should someone wish to condct further research into this topic

7.2 Future Work

First and foremost, separating out the particle charge and electric field would be an important future accomplishment. Doing this will provide significant progress in plasma actuator characterization and testing of dusty plasma charging theories. A combination of Maxwell's equations might be used to close the equations, but they require knowledge of charge density within the plasma and boundary conditions. V-dot probe measurements work very well and it's easy to imagine a wall of electrodes surrounding the plasma actuator to measure the voltage and attain boundary conditions. A closer look at all the pertaining equations may lead to a method of determining the charge and electric field.

Accounting for particle charging effects leads to the extrapolation of the true air velocity and the calculation of the electrostatic force and the Stokes drag force acting on the particles. Improvements to the PIV measurements can lead to even better mapping of these quantities. Measurement error can be reduced by seeding the chamber using a method that better keeps the particles separate. Accounting for more PIV error sources could reduce the uncertainty and lead to a better understanding of the flow characteristics and the dependence on particle size. In this work a linear fit was considered because the velocity uncertainty was too large to assume a higher order relation.

Measurements near the electrode region were obstructed due to the laser reflection. This problem plagues all PIV studies. A less reflective, possibly black, electrode material could be used to get more accurate measurements in this important region. Further reduction of the uncertainty can be accomplished by investigating some of the present assumptions. It was assumed that the electric field and plasma actuator performance are the same from one cycle to the next. This assumption can be tested by running multiple experiments with the same particle. If the seeding method is improved, the only differences between runs will be caused by the plasma actuator variance.

If uncertainty can be reduced enough, and linear fits are found to be accurate enough, only two particle sets would be needed to calculate the true air velocity. The smaller particle size can be determined by the intensity of light reflected to the camera, and the larger particle can be as large as the Stokes number allows for proper tracing of the given flow. Low seeding densities are recommended to minimize the effect on the flow. This study showed that, qualitatively, the flow kept its structure, but seeding density effects were not considered. Using ensemble averaging, at least 50 double images were needed for convergence in this study; therefore, at least 100 image pairs are recommended. More image pairs will allow for smaller interrogation windows and better vector resolution, but the camera memory is the limiting factor. With the air velocity available, new analyses can be conducted looking into the Navier-Stokes equations for plasma actuator flow, accounting for pressure gradients and electrostatic forces.

References

[1] Khrapak, S., and Morfill, G., "Basic processes in complex (dusty) plasmas: charging, interactions, and ion drag force," *Contributions to Plasma Physics*, Vol. 49, No. 3, 2009, pp 148-168

[2] Roth, J. R., Sherma, D. M., Wilkinson, S. P., "Boundary layer flow control with a one atmosphere uniform glow discharge surface plasma," *36th AIAA Aerospace Sciences Meeting and Exhibit*, AIAA, Washington DC, 1998

[3] Roth, J. R., "Aerodynamic flow acceleration using paraelectric and peristaltic electrohydrodynamic effects of a One Atmosphere Uniform Glow Discharge Plasma," *Physics of Plasmas*, Vol. 10, No. 5, May 2003

[4] He, C., Corke, T. C., Patel, M. P., "Plasma Flaps and Slat: An Application of Weakly Ionized Plasma Actuators," *Journal of Aircraft*, Vol. 46, No. 3, May-June 2009

[5] Greenblatt, D., Ben-Harav, A., Schulman, M., "Dynamic Stall Control on a Vertical Axis Wind Turbine Using Plasma Actuators,"*50th AIAA Aerospace Sciences Meeting including the New Horizons Forum and Aerospace Exposition*, AIAA, Washington DC, 2012

[6] Nishihara, M., Takashima, K., Rich, J. W., Adamovich, I. V., "Mach 5 Bow shock Control by a Nanosecond Pulse Surface DBD," *49th AIAA Aerospace Sciences Meeting including the New Horizons Forum and Aerospace Exposition*, AIAA, Washington DC, 2011

[7] Gnemmi, P., Rey, C., "Plasma Actuation for the Control of a Supersonic Projectile," *Journal of Spacecraft and Rocket*, Vol. 46, No. 5, Sep.-Oct. 2009

[8] Kriegseis, J., Schröter, D., Barckmann, K., Duchmann, A., Tropea C., Grundmann, S., "Closed-Loop Performance Control of Dielectric-Barrier-Discharge Plasma Actuators," *AIAA Journal*, Vol. 51, No. 4, April 2013

[9] Kogelschatz, U., "Dielectric-barrier discharges: Their history, discharge physics, and industrial applications," *Plasma Chemistry and Plasma Processing*, Vol. 23, No. 1, March 2003

[10] Moreau, E., "Airflow control by non-thermal plasma actuators," *Journal of Physics D: Applied Physics*, Vol. 40, No. 3, 2007, pp 605-633

[11] Corke, T. C., Enloe, C. L., Wilkinson, S. P., "Dielectric Barrier Discharge Plasma Actuators for Flow Control," *Annual Review of Fluid Mechanics*, Vol. 42, 2010, pp 505-529

[12] Corke, T. C., Post, M. L., Orlov, D. M., "SDBD plasma enhanced aerodynamics: concepts, optimization and applications," *Progress in Aerospace Sciences*, Vol. 43, No, 7-8, 2007, pp 193-217

[13] Corke, T. C., Post, M. L., Orlov, D. M., "Single dielectric barrier discharge plasma enhanced aerodynamics physics, modeling and applications," *Experiments in Fluids*, Vol, 46, No. 1, Jan. 2009, pp 1-26

[14] Enloe, C. L., McLaughlin, T. E., VanDyken, R. D., Kachner, K. D., Jumper, E. J., Corke, T. C., Post, M., Haddad, O., "Mechanisms and Responses of a Dielectric Barrier Plasma Actuator: Geometric Effects," *AIAA Journal*, Vol. 42, No. 3, March 2004

[15] Hoskinson, A. R., Hershkowitz, N., Ashpis, D. E., "Force measurements of single and double barrier DBD plasma actuators in quiescent air," *Journal of Physics D: Applied Physics*, Vol. 41, No. 24, 2008

[16] Forte, M., Jolibois, J., Pons, J., Moreau, E., Touchard, G., Cazalens, M., "Optimization of a dielectric barrier discharge actuator by stationary and non-stationary measurements of the induced flow velocity: application to airflow control," *Experiments in Fluids*, Vol. 43, No. 6, Dec. 2007, pp 917-928.

[17] Kriegseis, J., Dehles, T., Pawlik, M., Tropea, C., "Pattern-Identification Study of the Flow in Proximity of a Plasma Actuator," *47th AIAA Aerospace Sciences Meeting Including The New Horizons Forum and Aerospace Exposition*, AIAA, Washington DC, 2009

[18] Thomas, F. O., Corke, T. C., Iqbal, M., Kozlov, A., Schatzman, D., "Optimization of dielectric barrier discharge plasma actuators for active aerodynamic flow control," *AIAA Journal*, Vol. 47, No. 9, Sept. 2009

[19] Pons, J., Moreau, E., Touchard, G., "Asymmetric surface dielectric barrier discharge in air at atmospheric pressure: electrical properties and induced airflow characteristics," *Journal of Physics D: Applied Physics*, Vol. 38, No. 19, 2005

[20] Durscher, R., Roy, S., "On Multi-Barrier Plasma Actuators," *49th AIAA Aerospace Sciences Meeting including the New Horizons Forum and Aerospace Exposition*, AIAA, Washington DC, Jan. 2011

[21]Erfani, R., Hale, C., Kontis, K., "The Influence of Electrode Configuration and Dielectric Temperature on Plasma Actuator Performance," *49th AIAA Aerospace Sciences Meeting including the New Horizons Forum and Aerospace Exposition*, AIAA, Washington DC, Jan. 2011
[22] Orlov, D. M., Apker, T., He, C., Othman, H., Corke, T. C., "Modeling and Experiment of Leading Edge Separation Control Using SDBD Plasma Actuators," *45th AIAA Aerospace Sciences Meeting and Exhibit*, AIAA, Washington DC, 2007
[23]Enloe, C. L., McLaughlin, T. E., VanDyken, R. D., Kachner, K. D., Jumper, E. J., Corke, T. C., "Mechanisms and Responses of a Dielectric Barrier Plasma Actuator: Plasma Morphology," *AIAA Journal*, Vol. 42, No. 3, March 2004
[24]Benard, N., Jolibois, J., Moreau, E., "Lift and drag performances of an axisymmetric airfoil controlled by plasma actuator," *Journal of Electrostatics*, Vol. 67, No. 2-3, 2009, pp 133-139
[25]Balcon, N., Benard, N., Lagmich, Y., Boeuf, J.-P., Touchard, G., Moreau, E., "Positive and negative sawtooth signals applied to a DBD plasma actuator - influence on the electric wind," *Journal of Electrostatics*, Vol. 67, No. 2-3, 2009, pp 140-145
[26] Kotsonis, M., Ghaemi, S., "Forcing mechanisms of dielectric barrier discharge plasma actuators at carrier frequency of 625 Hz," *Journal of Applied Physics*, Vol. 10, No. 11, 2011
[27]Font, G. I., Enloe, C. L., Newcomb, J. Y., Teague, A. L., Vasso, A. R., McLaughlin, T. E., "Effects of Oxygen Content on Dielectric Behavior Barrier Discharge Plasma Actuator Behavior," *AIAA Journal*, Vol. 49, No. 7, July 2011
[28] Leonov, S. B., Opaits, D., Miles, R., Soloview, V., "Time-Resolved Measurements on Plasma-Induced Momentum in Air and N2 under DBD Actuation," *49th AIAA Aerospace Sciences Meeting including the New Horizons Forum and Aerospace Exposition*, AIAA, Washington DC, 2011
[29]Benard, N., Balcon, N., Moreau, E., "Electric wind produced by a surface dielectric barrier discharge operating in air at different pressures: aeronautical control insights," *Journal of Physics D: Applied Physics*, Vol. 41, No. 4, 2008
[30]Benard, N., Balcon, N., Moreau, E., "Electric Wind Produced by a Surface Dielectric Barrier Discharge Operating Over a Wide Range of Relative Humidity," *47th AIAA Aerospace Sciences Meeting Including The New Horizons Forum and Aerospace Exposition*, AIAA, Washington DC, 2009
[31]Enloe, C. L., Font, G. I., McLaughlin, T. E., Orlov, D. M., "Surface Potential and Longitudinal Electric Field Measurements in the Aerodynamic Plasma Actuator," *AIAA Journal*, Vol. 46, No. 11, Nov. 2008
[32]Nichols, T. G., Rovey, J., L., "Fundamental Processes of DBD Plasma Actuators Operating at High Altitude," *50th AIAA Aerospace Sciences Meeting including the New Horizons Forum and Aerospace Exposition*, AIAA, Washington DC, 2012
[33]Kozlov, K. V., Wagner, H-E., Brandenburg, R., Michel, P., "Spatio-temporally resolved spectroscopic diagnostics of the barrier discharge in air at atmospheric pressure," *Journal of Physics D: Applied Physics*, Vol. 34, No. 21, 2001
[34]Starikovskaia, S. M., Allegraud, K., Guaitella, O., Rousseau, A., "On electric field measurements in surface dielectric barrier discharge," *Journal of Physics D: Applied Physics*, Vol. 43, No. 12, 2010
[35]Stanfield, S. A., Menart, J., DeJoseph, C., Jr., Sands. B., "Spectroscopic Investigation of An Asymmetric Surface Dielectric Barrier Discharge," *39th Plasmadynamics and Lasers Conference*, AIAA, Washington DC. 2008
[36]Stanfield, S. A., Menart, J., DeJoseph, C., Jr., Kimmel, L., Hayes, J. R., "Rotational and Vibrational Temperature Distributions for a Dielectric Barrier Discharge in Air," *AIAA Journal*, Vol. 47, No. 5, May 2009
[37] Stanfield, S. A., Menart, J., "Optical emission spectroscopy measurements within a single microdischarge of a dielectric barrier discharge actuator," *Applied Physics Letters*, Vol. 103, No. 5, 2013
[38] Wu, Y., Li, Y., Jia, M., Song, H., Guo, Z., Zhu, X., Pu, Y., "Influence of operating pressure on surface dielectric barrier discharge plasma aerodynamic actuation characteristics," *Applied Physics Letters*, Vol. 93, No. 3, 2008
[39] Li., Y-H., Wu, Y., Jia, M., Zhou, Z.-W., Guo, Z.-G., Pu, Y.-K., "Optical Emission Spectroscopy Investigation of a Surface Dielectric Barrier Discharge Plasma Aerodynamic Actuator," *Chinese Physics Letters*, Vol. 25, No. 11, 2008

[40]Suzen, Y. B., Huang, P. G., Jacob, J. D., Ashpis, D. E., "Numerical Simulations of Plasma Based Flow Control Applications," *35th Fluid Dynamics Conference and Exhibit*, AIAA, Washington DC, 2005
[41]Suzen, Y. B., Huang, P. G., Ashpis, D. E., "Numerical Simulations of Flow Separation Control in Low-Pressure Turbines using Plasma Actuators," *45th AIAA Aerospace Sciences Meeting and Exhibit*, AIAA, Washington, 2007
[42]Meijerink, J. A. W., Hoeijmakers, H. W. M., "Plasma Actuators for Active Flow Control on Wind Turbine Blades," *29th AIAA Applied Aerodynamics Conference*, AIAA, Washington DC, 2011
[43]Maden I., Maduta, R., Kriegseis, J., Jakirlić, S., Schwarz, C., Grundmann, S., Tropea, C., "Experimental and computational study of the flow induced by a plasma actuator," *International Journal of Heat and Fluid Flow*, Vol. 41, June 2013, pp 80-89
[44] Braun, D., Küchler, U., Pietsch, G., "Microdischarges in air-fed ozonizers," *Journal of Physics D: Applied Physics*, Vol. 24, 1991, 564-572.
[45]Braun, D., Gibalov, V., Pietsch, G., "Two-dimensional modelling of the dielectric barrier discharge in air," *Plasma Sources Science and Technology*, Vol. 1, No. 3, 1992, pp 166-174
[46]Jayaraman, B., Shyy, W., "Modeling of dielectric barrier discharge-induced fluid dynamics and heat transfer," *Progress in Aerospace Sciences*, Vol. 44, 2008, pp 139-191
[47] Font, G. I., "Boundary Layer Control with Atmospheric Plasma Discharges," *40th AIAA/ASME/SAE/ASEE Joint Propulsion Conference and Exhibit*, AIAA, Washington DC, 2004
[48]Orlov, D. M., Font, G. I., Edelstein, D., "Characterization of Discharge Modes of Plasma Actuators," *AIAA Journal*, Vol. 46, No. 12, December 2008
[49]Boeuf, J. P., Lagmich, Y., Unfer, Th., Callegari, Th., Pitchford, L. C., "Electrohydrodynamic force in dielectric barrier discharge plasma actuators," *Journal of Physics D: Applied Physics*, Vol. 40, No. 3, 2007
[50] Likhanskii, A. V., Shneider, M. N., Macheret, S. O., Miles, R. B., "Modeling of dielectric barrier discharge plasma actuator in air," *Journal of Applied Physics*, Vol. 103, No. 5, 2008
[51] Boeuf, J. P., Lagmich, Y., Pitchford, L. C., "Contribution of positive and negative ions to the electrohydrodynamic force in a dielectric barrier discharge plasma actuator operating in air," *Journal of Applied Physics*, Vol. 106, No. 2, 2009
[52] Adrian, R. J., "Twenty years of particle image velocimetry," *Experiments in Fluids*, Vol. 39, No. 2, 2005
[53] Willert, C. E., Gharib, M., "Digital particle image velocimetry," *Experiments in Fluids*, Vol. 10, No. 4, 1991, pp 181-193
[54] Lourenco, L. M., Gogineni, S. P., LaSalle, R. T., "On-line particle-image velocimeter: an integrated approach," *Applied optics*, Vol. 33, No. 13, 1994
[55] Keane, R. D., Adrian, R. J., "Theory of cross-correlation analysis of PIV images," *Applied Scientific Research* Vol. 49, No. 3, 1992, pp 191-215
[56] Westerweel, J., "Efficient detection of spurious vectors in particle image velocimetry data," *Experiments in Fluids*, Vol. 16, No. 3, 1994
[57] Westerweel, J., "Theoretical analysis of the measurements precision in particle image velocimetry," *Experiments in Fluids*, Vol. 29, 2000
[58] Willert, C., "The fully digital evaluation of photographic PIV recordings," *Applied Scientific Research*, Vol. 56, No. 2, 1996, pp 79-102
[59] Scarano, F., "Iterative image deformation methods in PIV," *Measurements Science and Technology*, Vol. 13, No. 1, 2001
[60] Scarano, F., Riethmuller, M. L., "Advances in iterative multigrid PIV image processing," *Experiments in Fluids*, Vol. 29, 2000
[61] Scarano, F., Riethmuller, M. L., "Iterative multigrid approach in PIV image processing with discrete image window offset," *Experiments in Fluids*, Vol. 26, No. 6, 1999, pp 513-523
[62] Westerweel, J., "Fundamentals of digital particle image velocimetry," *Measurements Science and Technology*, Vol. 8, No. 12, 1997
[63] Raffel, M., Willert, C. E., Kompenhans, J., *Particle Image Velocimetry: A Practical Guide*, Springer Science & Business Media, Berlin, Germany, 2007
[64] Adrian, R. J., Westerweel, J., *Particle Image Velocimetry*, Cambridge University Press, New York, USA, 2011

[65] Melling, A., "Tracer particles and seeding for particle image velocimetry," *Measurements Science and Technology*, Vol. 8, No. 12, 1997
[66] Adrian, R. J., Yao, C. S., "Pulsed laser technique application to liquid and gaseous flows and the scattering power of seed material," *Applied Optics*, Vol. 24, No. 1, 1985, pp 44-52
[67] Lindken, R., Rossi, M., Grosse, S., Westerweel, J., "Micro-particle image velocimetry (microPIV): recent developments, applications, and guidelines," *Lab on a chip*, Vol. 9, No. 17, 2009, pp 2551-2567
[68] Santiago, J. G., Wereley S. T., Meinhart, C. D., Beebe, D. J., "A particle image velocimetry system for microfluidics," *Experiments in Fluids*, Vol. 25, No. 4, 1998
[69] Meinhart, C. D., Wereley, S. T., Santiago, J. G., "A PIV algorithm for estimating time-averaged velocity fields," *Journal of Fluids Engineering*, Vol. 122, No. 2, 2000, pp 285-289
[70] Westerweel, J., Geelhoed, P. F., Lindken, R., "Single-pixel resolution ensemble correlation for micro-PIV applications," *Experiments in Fluids*, Vol. 37, No. 3, 2004, pp 375-384
[71] Kähler, C. J., Scholz, U., "Transonic jet analysis using long-distance micro PIV," *12th International Symposium on Flow Visualization*, 2006
[72] Willert, C., "Adaptive PIV processing based on ensemble correlation," *14th International Symposium on Applications of Laser Techniques to Fluid Mechanics*, Lisbon Portugal, 2008
[73] Timmins, B. H., Wilson, B. W., Smith, B. L., Vlachos, P. P., "A method for automatic estimation of instantaneous local uncertainty in particle image velocimetry," *Experiments in Fluids*, Vol. 53, No. 4, 2012
[74] Sciacchitano, A., Wieneke, B., Scarano, F., "PIV uncertainty quantification by image matching," *Measurements Science and Technology*, Vol. 24, No. 4, 2013
[75] Charonko, J. J., Vlachos, P. P., "Estimation of uncertainty bounds for individual particle image velocimetry measurements from cross-correlation peak ratio," *Measurement Science and Technology*, Vol. 24, No. 6, 2013
[76] Wieneke, B., "Generic a-posteriori uncertainty quantification for PIV vector fields by correlation statistics," *17th international symposium on applications of laser techniques to fluid mechanics*, Lisbon, Portugal, 2014
[77] Neal, D. R., Sciacchitano, A., Smith, B. L., Scarano, F., "Collaborative framework for PIV uncertainty quantification: the experimental database," *Measurements Science and Technology*, Vol. 26, No. 7, 2015
[78] Sciacchitano, A., Neal, D. R., Smith, B. L., Warner, S. O., Vlachos, P. P., Wieneke, B., Scarano, F., "Collaborative framework for PIV uncertainty quantification: comparative assessment of methods," *Measurements Science and Technology*, Vol. 26, No. 7, 2015
[79] Scharnowski, S., Hain, R., Kähler, C. J., "Reynolds stress estimation up to single-pixel resolution using PIV-measurements," *Experiments in Fluids*, Vol. 52, No. 4, 2012
[80] Allen, J. E., "Probe theory- the orbital motion approach," *Physica Scripta*, Vol. 45, No. 5, 1992
[81] Kennedy, R. V., Allen, J. E., "The floating potential of spherical probes and dust grains. II: orbital motion theory," *Journal of Plasma Physics*, Vol. 69, No. 6, 2003, pp 485-506
[82] Allen, J. E., Boyd, R. L. F., Reynolds, P., "The collection of positive ions by a probe immersed in a plasma," *Proceedings of the Physical Society. Section B*, Vol. 70, No. 3, 1957
[83] Ratynskaia, S., Khrapak, S., Zobnin, A., Thoma, M.H., Kretschmer, M., Usachev, A., Yaroshenko, V., Quinn, R.A., Morfill, G.E., Petrov, O., Fortov, V., "Experimental determination of dust particle charge," *Physics Review Letters*, Vol. 93, No. 8, 2004
[84] Khrapak, S.A., Ratynskaia, S.V., Zobnin, A.V., Usachev, A.D., Yaroshenko, V.V., Thoma, M.H., Kretschmer, M., Höfner, H., Morfill, G.E., Petrov, O.F., Fortov, V.E., "Particle charge in the bulk of gas discharge," *Physical Review E*, Vol. 72, No. 1, 2005
[85] Lampe, M., Goswami, R., Sternovsky, Z., Robertson, S., Gavrishchaka, V., Ganguli, G., Joyce, G., "Trapped ion effect on shielding, current flow, and charging of a small object in a plasma," *Physics of Plasmas*, Vol. 10, No. 5, 2003, pp 1500-1513
[86] Khrapak, S.A., Tolias, P., Ratynskaia, S., Chaudhuri, M., Zobnin, A., Usachev, A., Rau, C., Thoma, M.H., Petrov, O.F., Fortov, V.E., Morfill, G.E., "Grain charging in an intermediately collisional plasma," *EPL (Europhysics Letters)*, Vol. 97, No. 3, 2012
[87] Chang, J. S., Laframboise, J. G., "Probe theory for arbitrary shape in a large Debye length, stationary plasma," *The Physics of Fluids*, Vol. 19, No. 1, 1976, pp 25-31

[88] Gatti, M., Kortshagen, U., "Analytical model of particle charging in plasmas over a wide range of collisionality," *Physics Review E*, Vol. 78, No. 4, 2008
[89] Khrapak, S.A., Morfill, G.E., Khrapak, A.G., D'yachkov, L.G., "Charging properties of a dust grain in collisional plasmas," *Physics of Plasmas*, Vol. 13, No. 5, 2006
[90] Khrapak, S. A., Klumov, B. A., Morfill, G. E., "Electric potential around an absorbing body in plasmas: Effect of ion-neutral collisions," *Physical Review Letters*, Vol. 100, No. 22, 2008
[91] Khrapak, S. A., Klumov, B. A., Morfill, G. E., "Ion collection by a sphere in a flowing highly collisional plasma," *Physics of Plasmas*, Vol. 14, No. 3, 2007
[92] Ivlev, A.V., Zhdanov, S.K., Khrapak, S.A., Morfill, G.E., "Ion drag force in dusty plasmas," *Plasma Physics and Controlled Fusion*, Vol. 46, No. 12B, 2004
[93] Khrapak, S. A., Zhdanov, S. K., Ivlev, A. V., Morfill, G. E., "Drag force on an absorbing body in highly collisional plasmas," *Journal of Applied Physics*, Vol. 101, No. 3, 2007
[94] Schweigert, I.V., Alexandrov, A.L., Peeters, F.M., "Negative ion drag force in a plasma of gas discharge," *IEEE Transactions on Plasma Science*, Vol. 32, No. 2, 2004, pp 623-626
[95] Chaudhuri, M., Khrapak, S.A., Morfill, G.E., "Effective charge of a small absorbing body in highly collisional plasma subject to an external electric field," *Physics of Plasmas*, Vol. 14, No. 5, 2007
[96] Chaudhuri, M., Khrapak, S.A., Morfill, G.E., "Electrostatic potential behind a macroparticle in a drifting collisional plasma: Effect of plasma absorption," *Physics of Plasmas*, Vol. 14, No. 2, 2007
[97] Chaudhuri, M., Khrapak, S.A., Morfill, G.E., "Ion drag force on a small grain in highly collisional weakly anisotropic plasma: Effect of plasma production and loss mechanism," *Physics of Plasmas*, Vol. 15, No. 5, 2008
[98] Khrapak, S.A., Chaudhuri, M., Morfill, G.E., "Ion drag force in collisional plasmas," *IEEE Transactions on Plasma Science*, Vol. 37, No. 4, 2009
[99] Franklin, R. N., "Electronegative plasmas-why are they so different?," *Plasma Sources Science and Technology*, Vol. 11, No. 3A, 2002
[100] Klumov, B.A., Ivlev, A. V., Morfill, G., "The role of negative ions in experiments with complex plasma," *Journal of Experimental and Theoretical Physics Letters*, Vol. 78, No. 5, 2003, pp 300-304
[101] Mamun, A.A., Shukla, P.K., "Charging of dust grains in a plasma with negative ions," *Physics of Plasmas*, Vol. 10, No. 5, 2003, pp 1518-1520
[102] Rapp, M., Hedin, J., Strelnikova, I., Friedrich, M., Gumbel, J., Lübken, F.J., "Observations of positively charged nanoparticles in the nighttime polar mesosphere," *Geophysical Research Letters*, Vol. 32, No. 23, 2005
[103] Kim, S.H., Merlino, R.L. "Charging of dust grains in a plasma with negative ions," *Physics of Plasmas*, Vol. 13, No. 5, 2006
[104] Durscher, R., Roy, S., "Induced flow from serpentine plasma actuators acting in quiescent air," *49th AIAA Aerospace Sciences Meeting including the New Horizons Forum and Aerospace Exposition*, AIAA, Orlando, Florida, 2011
[105] Masati, A., Sydney, A. J., Sedwick, R. J., "Parametric study of particle size for plasma actuator PIV measurements," *52nd Aerospace Sciences Meeting*, AIAA, Washington DC, 2014
[106] Nagato, k., Matsui, Y., Miyata, T., Yamauchi, T., "An analysis of the evolution of negative ions produced by a corona ionizer in air," *International Journal of Mass Spectroscopy*, Vol. 248, No. 3, 2006, pp 142-147
[107] Murphy, J.P., Kriegseis, J., Lavoie, P., "Scaling of maximum velocity, body force, and power consumption of dielectric barrier discharge plasma actuators via particle image velocimetry," *Journal of Applied Physics*, Vol. 113, No. 24, 2013
[108] Hogg, J. L., "Viscosity of air," *Proceedings of the American Academy of Arts and Sciences*, Vol. 40, No. 18, 1905
[109] Murphy, A. B., "Transport coefficients of air, argon-air, nitrogen-air, and oxygen-air plasmas," *Plasma Chemistry and Plasma Processing*, Vol. 15, No. 2, 1995
[110] Nielsen, R. A., Bradbury, N. E., "Electron and negative ion mobilities in oxygen, air, nitrous oxide and ammonia ," *Physical Review*, Vol. 51, No. 2, 1937
[111] Frommhold, L., "Über verzögerte elektronen in elektronenlawinen, insbesondere in sauerstoff und luft, durch bildung und zerfall negativer ionen (O-)," *Fortschritte der Physik*, Vol. 12, No. 11, 1964

[112] Dutton Database, www.lxcat.net, retrieved on January 16, 2017

[113] Stano, M., Safonov, E., Kučera, M., Matejčik, Š., "Ion mobility spectrometry study of negative corona discharge in oxygen/nitrogen mixtures," *Chemické listy*, Vol. 102, 2008

[114] Sabo, M., Páleník, J., Kučera, M., Han, H., Wang, H., Chu, Y., Matejčík, Š., "Atmospheric pressure corona discharge ionisation and ion mobility spectrometry/mass spectrometry study of the negative corona discharge in high purity oxygen and oxygen/nitrogen mixtures," *International Journal of Mass Spectroscopy*, Vol. 293, No. 1, 2010

[115] Böhringer, H., Fahey, D.W., Lindinger, W., Howorka, F., Fehsenfeld, F.C., Albritton, D.L., "Mobilities of several mass-identified positive and negative ions in air," *International journal of mass spectrometry and ion processes*, Vol. 81, 1987